UNIVERSITÀ DEGLI STUDI DI PADOVA

DIPARTIMENTO DI SCIENZE CHIMICHE

CORSO DI LAUREA MAGISTRALE IN

SCIENZA DEI MATERIALI

TESI DI LAUREA MAGISTRALE

Nickel-based catalysts for the Ammonia Oxidation Reaction

RELATORE: PROF. ELENA PASTOR TEJERA,

PROF. LAURA CALVILLO LAMANA

CONTRORELATORE: PROF. CHRISTIAN DURANTE

LAUREANDO: MATTEO TREVISAN

Anno Accademico: 2023/2024

INDEX

Abstract

The severity of the current climate crisis is unprecedented, and the transition toward renewable energy must accelerate its course to mitigate the consequences of overpopulation and rising temperatures. Scientists believe H_2 can play a lead role in the transition to renewable energies, as it is considered one of the best energy carriers thanks to its high gravimetric energy density. However, several technological downsides regarding its safe storage, handling, and transportation, hinder its feasibility as a fossil fuel alternative. For these reasons, many scientific endeavors are focused on the research of new energy carriers outperforming or at least facilitating hydrogen accessibility. Ammonia stands out as a carbon-free compound containing 17.7 wt % of H_2, requiring only up to 8 bars at room temperature to store, potentially allowing for safer hydrogen production at the point of usage. Moreover, a large and mature infrastructure network for the storage and transportation of this chemical has been developed and optimized throughout many decades, making ammonia a great alternative energy source carrier, bypassing critical technological and logistics limitations faced by hydrogen technology accessible up to date.

Materials science plays a critical role in developing high performance and cost effective electrocatalyst to facilitate the exploitation of this energy vector. Nickel-based materials have proven to be active toward the electrochemical Ammonia Oxidation Reaction (eAOR), displaying promising results as a cheaper and easier to access electrocatalysts when compared to other precious metals such as Pt, Ir, Rh, often subjects of geopolitical disputes. During this 6 months Research Internship at the University of La Laguna, several Ni-based materials with different morphologies were synthesized to study their electrocatalytic activity toward ammonia oxidation with conventional and operando electrochemical techniques such as Cyclic Voltammetry (CV), Linear Sweep Voltammetry (LSV) and Differential Electrochemical Mass Spectroscopy (DEMS). In addition to that, several physicochemical characterization techniques such as Scanning Electron Microscopy (SEM) and Energy Dispersive X-ray Analysis (EDX), Transmission Electron Microscopy (TEM), Inductively Coupled Plasma Mass Spectroscopy (ICP-MS), X-ray Diffraction (XRD), and X-ray Photoelectron Spectroscopy (XPS) were employed to understand the structural and electronic properties of the samples to allow for the correlation between their fundamental properties and their electrochemical response.

Five different morphologies were synthesized, but the catalytic activity of the samples was confirmed mainly for two samples that proved to be the most promising due to the synergic effect of Ni and Cu atoms left from the precursors. The most active sample was studied with DEMS. With this technique

DEMS it was possible to accurately determine electrochemical parameters such as eAOR onset potential, Oxygen Evolution Reaction (OER) onset potential, and outstandingly, it allowed the precise detection of gaseous products of the reaction such as N_2, O_2, and other toxic and undesired byproducts such as N_2O, and NO species, responsible for selectivity limitations and ultimately high overpotentials. Thanks to DEMS analysis, the role of the presence of O_2 in the reaction was studied further, revealing the influence on the eAOR onset potential and inhibition of OER. Also, new insights on the role of Cu were found through in-situ electrochemistry, as NO production seemed related to this element.

CHAPTER 1

1.1 Climate Change & Energy Demand

Globalization has been shaping our world and providing a quality of life like no human beings had ever seen before. Progress and technology are the engines that propel society forward and are partly responsible for the exponential growth of economies worldwide. All the major revolutions and scientific breakthroughs, from the Industrial Revolution back in the 18th century, to the more recent semiconductor-driven one, changed the way people used to live, arguably for the better. However, scientists worldwide agree and have shown how this increased human activity is also responsible for the major current climate crisis and how this is reshaping the world.

In particular, the increasing emission and the higher concentration of CO_2 (and other greenhouse gasses for that matter) in the atmosphere, due to human-related activity is currently responsible for the constant increase in the average temperature worldwide and the devastating consequences deriving from that, such as more frequent extreme events like flooding, wildfires and droughts[1,2]. In 1988 the World Meteorological Organization and the United Nations Environment Program established the Intergovernmental Panel on Climate Change (IPCC), whose main task is to assess the science related to climate change and help and assist governments in the development of climate-related policies. Since then, this panel publishes the Annual Assessment Reports about the state of scientific, technical and socio-economic knowledge on climate change, its impacts and future risks, and options for reducing the rate at which climate change is taking place. According to these reports, which are widely accepted in the scientific community, a global average temperature increase of 2°C will have catastrophic consequences on the environment. For that, a transition toward a green, more environmentally friendly economy, not solely reliant on petroleum, which promotes the reduction of CO_2 emissions is vital, and the intergovernmental cooperation is crucial to sustaining such technological endeavors as well as socio-economic challenges. Governments have settled for the Paris Agreement signed in 2015, a legally binding international treaty on climate change. It was adopted by 196 Parties at the UN Climate Change Conference (COP21) in Paris, France, on 12 December 2015. It entered into force on 4 November 2016 and its goal is to retain the increase in the global average temperature to well below 2 °C above pre-industrial levels and focus all endeavors to limit the increase to 1.5°C above pre-industrial levels(3). With this understanding of the facts, it is important to ensure that the energy demand growth predicted for 2050 will be aligned with the founding principle of this treaty.

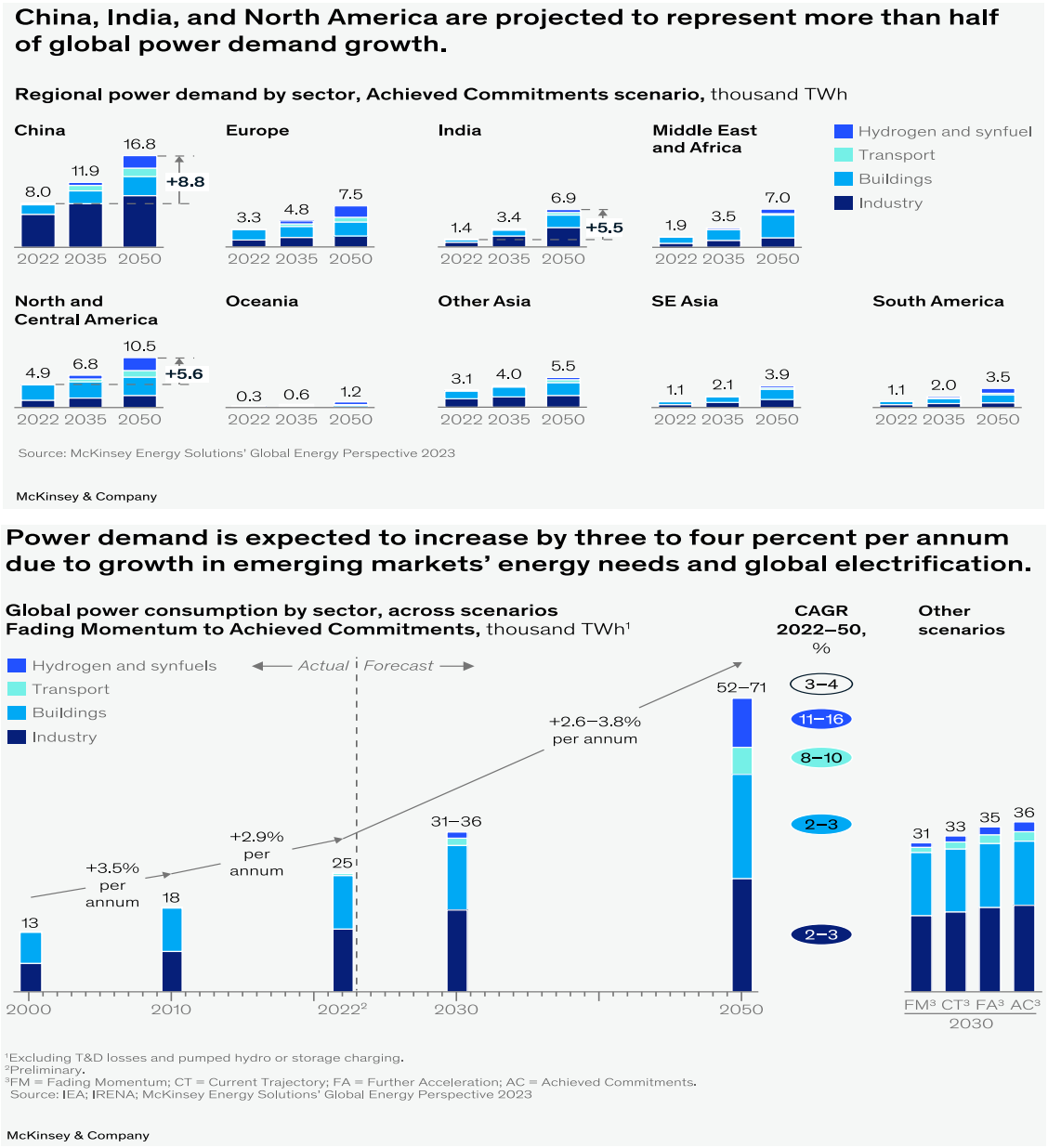

***Figure 1.1**: Global power demand prospect for the year 2000-2050 (top). Regional power demand prospect by sector (bottom). Reprinted from (3).*

Global electricity demand is expected to reach almost three times today's value due to the growth of emerging markets' needs. As Figure 1 shows, today's request of 25,000 TWh will reach nearly 72,000 TWh, and countries like China, India, and North America are expected to be the countries with the highest needs. However, from the same graph, one can see how, although currently limited, hydrogen and synfuel trade will rise as chemical industries and especially road transport will raise demand for clean hydrogen[(4)]. As the global energy consumption request increase, fossil fuel sources rapidly diminish, and scientists debate over the current and future availability of crude oil, therefore, the search for a new, greener energy vector, that is readily accessible, and as performant as petroleum-based fuels is of paramount importance.

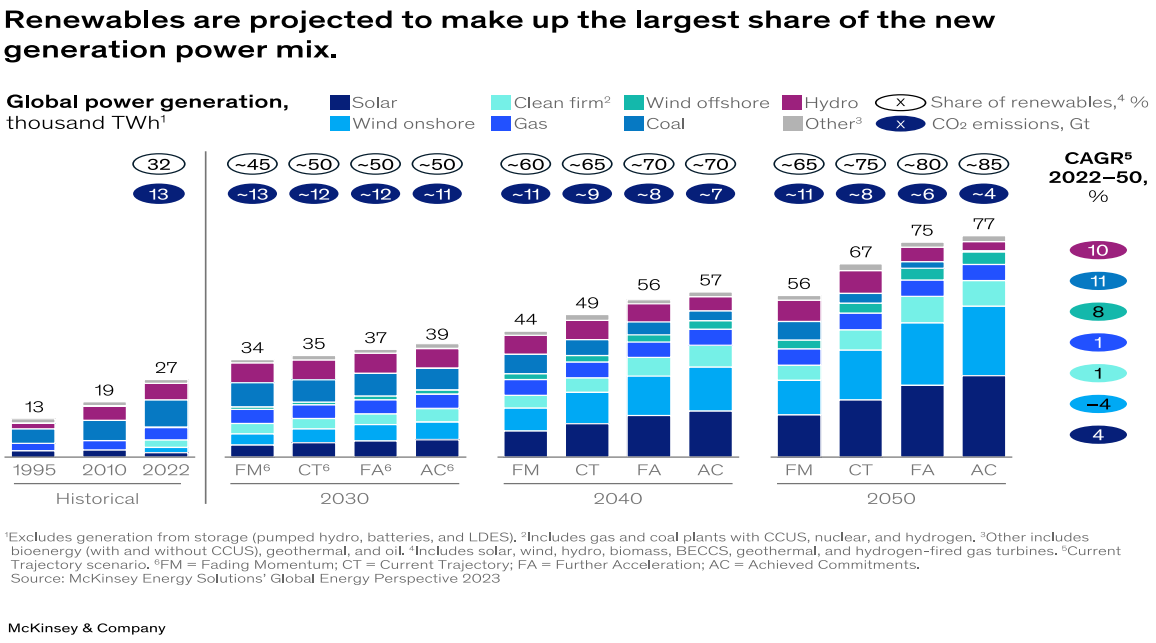

***Figure 1.2**: Renewable energy sources are expected to play a significant role in the transition toward net-zero emission. Solar and wind energy demand is forecasted to grow significantly in the next decades. Reprinted from (3).*

As reported by McKinsey & Company, renewables are expected to be the building block of the future energy supply chain. Among these, hydrogen technologies are expected to play a big role in the net zero transition.

1.2 Hydrogen Economy

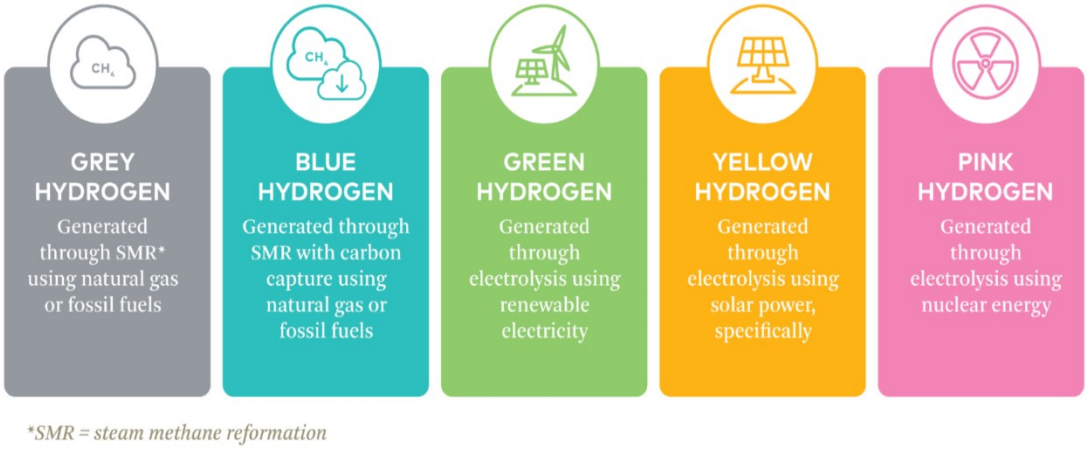

***Figure 1.3**: Schematic illustration of the different colors of Hydrogen Production. Reprinted from (8).*

Scientists regard H_2, the most abundant gas in the universe, as a promising energy vector that could help the transition toward the net-zero emission goal set for 2050. This is because this molecule can be obtained from renewable energy sources and is a carbon-free energy vector, with higher

gravimetric energy density than fossil fuels, making it an exceptional candidate to substitute petroleum.

To this day, hydrogen production can be achieved through different pathways leading scientists to categorize hydrogen production processes with colors; the most common of which is known as 'Grey Hydrogen', namely hydrogen obtained via steam reforming processes of fossil fuels, a process accompanied by large amounts of CO_2 emissions. This accounts for approximately 90 million tons per annum, however, as the rise in the demand for clean hydrogen is awaited, this estimate is expected to dramatically reduce. Among the many colors of hydrogen, 'Green Hydrogen' is the term used for that generated via electrolysis fueled by renewable energies as a source of electricity; this is currently the most interesting for the net-zero goals. Water electrolysis is the chemical process through which a water molecule is parted into its original components, namely hydrogen, and oxygen, when an electrical potential (theoretical $E^0 = 1.23$ V) is applied. However, the theoretical potential required for this reaction to occur is profoundly different from the real-world scenario, where due to many experimental variables large overpotentials are present and the practical electrochemical applied voltage required is 1.6-1.8 V.

By 2050, green hydrogen is expected to dominate the global supply mix, with a share of between 50 and 65 percent across scenarios, as cost reductions in renewables and electrolyzers make this production route more cost-competitive [3,4,5]. To make hydrogen economically appealing as an energy source, great technological endeavors are needed. That is owed to the fact that hydrogen has the highest energy per mass of any fuel; however, its volumetric energy density at room temperature density is low, requiring the development of advanced storage methods that allow a higher energy density.

Currently, storage technologies mainly rely on physical storage methods such as compression and liquefaction of this fuel, with major risk concerns coming along with them. Many downsides are found in the limited storage capacity and heat and energy losses when compressing or releasing on site of operation, thus limiting the overall efficiency of compressed hydrogen in the range of 70% to 90%[6]. When liquified, at a cryogenic temperature usually around -253 °C, boil-off during storage and safety are the most concerning aspects. New storage technologies mainly based on the physical adsorption of gaseous molecules on particular materials are currently under investigation; some examples are metal hydrates capable of storing hydrogen molecules thanks to favorable stoichiometric properties of the metal or materials with high surface area capable of physically absorbing gaseous molecules in their porous structure called Metal-Organic Frameworks (MOFs).

1.3 Ammonia Economy

Ammonia (NH_3) is one of the world's most important and largely produced chemicals. Unfortunately, mass utilization of nitrogen-based fertilizer can come with downsides, in fact, NH_3 emissions negatively affect the environment, as this is a toxic compound that can play a big role in exacerbating the climate change crisis; in fact, it is responsible for water, soil and air pollution, as ammonia can react with other pollutants present in the atmosphere such as sulfur or nitrogen as well, creating small particles leading up to smog formation and consequent respiratory problems; also, studies found that it is directly responsible for harming plants[7].

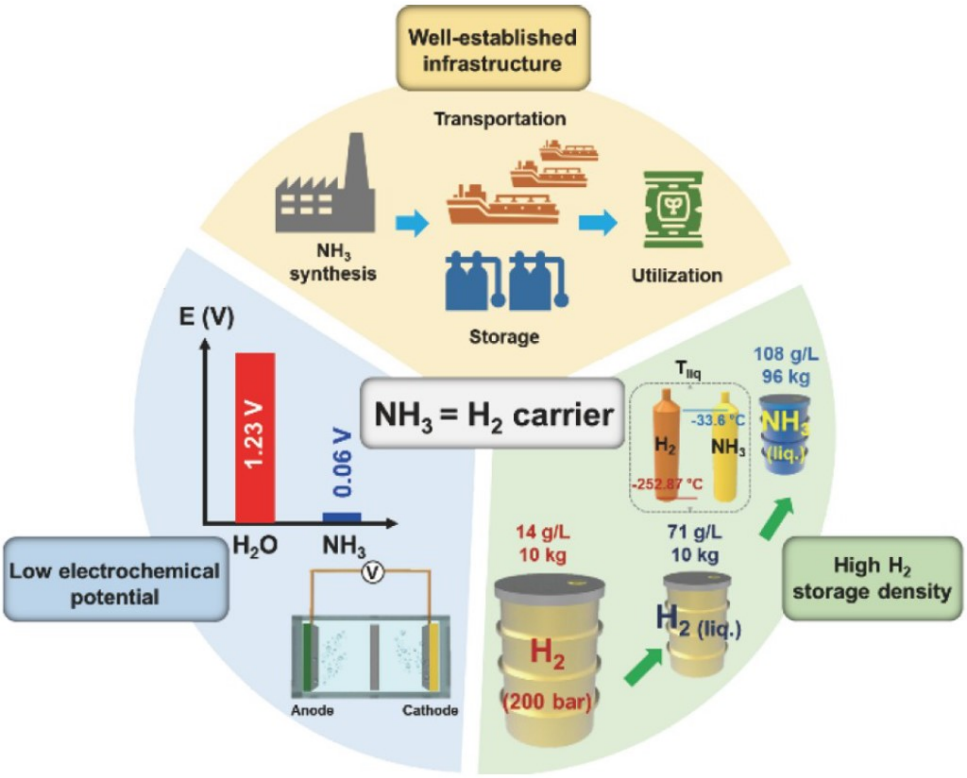

***Figure 1.4**: The ammonia economy diagram showing the potentiality of ammonia as a hydrogen carrier or as a green fuel potentially able to replace hydrogen. The strength points of ammonia are depicted and compared to the hydrogen economy as a reference. Reprinted from (8).*

Nevertheless, from the chemical point of view, ammonia is a carbon-free compound that contains 17.7 wt% of H_2, and it is fairly easy to store at room temperature as it only requires up to 8 bars of pressure to liquefy; also, a large and mature infrastructure network for the storage and transportation of this chemical has been developed and optimized throughout many decades. For these reasons, ammonia possesses great potential as an alternative energy source carrier, bypassing the critical

storage and transportation limitations, and making hydrogen production at the point of usage more accessible and safer[8,9,10].

Ammonia could be used as an alternative to methanol or hydrogen as fuel in fuel cells or to produce hydrogen in electrolytic cells. The mature transportation infrastructure developed throughout many years is a great asset to the ammonia economy. In particular, ammonia could be stored and transported in a liquid or solid form, under atmospheric conditions, or pressurized. A few aspects regarding the storage and transportation of this compound will be described below.

1.4 Ammonia Storage Systems

A brief description of the ammonia storage systems will be discussed analyzing the pros and cons of these technologies, and the readiness to the market[9]:

- Pressured ammonia is stored at ambient temperature in pressure vessels with capacities as large as 1,500 tons; this system is best suited for mobile applications such as storing small quantities as an intermediate storage site or for mobile applications involving loading and unloading of heavy-duty vehicles, maritime transportation.
- Semi-refrigerated Storage: this system allows the storage of the compound at low pressures (around 3-4 bars of pressure) and fairly low temperatures (around 0°C); ammonia vapors from the container are compressed in a single-stage compressor and liquefied by water cooling, and then returned to the tank as liquid. One of the main advantages of this system is the possibility of using lighter steel vessels than if the temperature was not controlled.
- Liquid ammonia, especially in large quantities, is stored in fully refrigerated single-wall or double-wall tanks depending on the application; this system is best suited for handling larger volumes of up to 50,000 tons. When stored in such a manner, the operation temperature is set at -33°C with pressures slightly above atmospheric pressure, again proving the advantages with respect to hydrogen storage.
- Solid-state storage is becoming an interesting perspective in storage technologies as it would limit end-consumer safety-related issues and would provide a space-optimizing yet with high gravimetric ammonia availability. Particular materials with specific properties like metal halides ($MX_m + nNH_3 \rightleftharpoons M(NH_3)_nX_m$ are the best candidates to store this compound, as they are capable of adsorbing ammonia at room temperature forming solid salts known as metal ammines, one of the most known example being $Mg(NH_3)_6Cl_2$. The adsorption and desorption are reversible processes that lower ammonia volatility limiting ammonia losses. It is important to specify that although this would represent fascinating and promising storage technology, it is fairly new and

with a low level of readiness concerning the well-established storage and transportation technologies already mentioned.

Eventually, the decision of the most suited storage technology is made on the base of the application and the storage capacity needed for the application, as well as on the base of economic advantages. Pressurization presents considerably higher costs than atmospheric pressure, however, the bigger capacity of the pressurized systems represents a strong point for this technology. Materials-based solid-state technology is considerably dearer than the already discussed alternatives[9].

***Table 1.1**: Summary table showing the working parameters of the ammonia storage technologies available up to date. The abbreviation (TRL) stands for Technology Readiness Levels and represents the accessibility of these technologies to the current market on a 1-10 scale. The higher scores obtained by the well-established storage technologies highlight the mature position and prestige of the ammonia economy in today's market[9,10].*

Type	TRL	Typical pressure, bar	Design temperature, °C	t ammonia per t steel	Capacity, t ammonia	Refrigeration compressor
Pressure storage	9	16-18	20-25	2.8-6.5	< 270 or < 1,500	None
Semi-refrigerated storage	9	3-5	Ca.0	10	450-2,700	Single stage
Low-temperature storage	9	1.1-1.2	-33	41-45	4,500-45,000 (< 50,000)	Two-stage
Solid-state storage	3-4	1-30	20-250	-	-	None

1.5 Ammonia Transportation

The mature transportation infrastructure developed throughout many decades is responsible for the annual transit of 25 to 30 million tons of ammonia worldwide[9]. Typical transportation ranges from a local distribution network mainly realized with the help of railways, heavy-duty vehicles, and pipelines, to an international network supported by maritime shipping and a long system of pipelines. Again, the final decision regarding the most suitable transportation system relies upon the application of interest and cost-related issues; also, the greenhouse gas emissions associated with transport may play an important factor in future policy making, leaning toward new eco-friendly possibilities and a more sustainable future for this sector.

1.6 Fuel Cells: Operating Principles, Components and Characterization

An overview of the storage and transportation possibilities has been discussed; however, another important topic must be addressed. To better understand the role of ammonia as a hydrogen carrier and possible alternative to crude oils-based fuels, a brief description of the basic operating principle of a fuel cell is given.

A fuel cell is an electrochemical device that harnesses the chemical energy of a fuel and transforms it into electrical energy. Many types of fuel cell technologies have been developed throughout the years, and some of the most widespread are Proton Exchange Membrane Fuel Cells (PEMFs), Solid Oxide Fuel Cells (SOFCs) or Direct Alcohols Fuel Cells (DAFCs). Fuel cell technologies are a promising resource in clean energy production, as most of the chemical fuels exploited by these technologies are environmentally friendly compounds like hydrogen or oxygen, producing water as the only byproduct. In the case of ammonia, Direct Ammonia Fuel Cells (DAFCs) are beginning to attract particular interest in the scientific community for their practical advantages over conventional hydrogen fuel, characterized by storage and transportation-related issues of the fuel. Fuel Cells are composed of several layers of different materials, and the heart of this technology is found in the Membrane Assembly Electrode, or MEA, which includes the membrane, the catalyst layer, and the gas diffusion layers (GDLs). Multiple other hardware is employed to incorporate the MEA, such as the gasket, which provides a seal for the MEA to prevent leakages, the bipolar plate, which is used as a cooling device, to provide channels for the gaseous fuel to flow, and provide mechanical stability[10,11].

As shown in the above picture, many are the components of a typical fuel cell. Starting from the outermost layer one can find two gas inlets, a current collector, and a graphite plate responsible respectively for providing the gas supply, realizing the electrical connections, and providing both mechanical stability and a cooling device to avoid overheating of the innermost layer of the cell. The Membrane Electrode Assembly (MEA) is the core of the device, and it is composed of the Polymeric Electrolyte Membrane (PEM), (for other types of cells this may vary or not be present at all), two catalyst layers, and two gas diffusion layers. The Gas Diffusion Layer (GDL) is often a layer of carbon-based fiber materials typically 100-300 μm thick, which is responsible for the diffusion of the gas phase to the catalyst, the prevention of the formation of hotspots, while also acting as a coolant. It possesses good electrical conductivity and is hydrophobic to prevent the accumulation of water on the cathode. The membrane, often composed of Nafion, is placed to separate the reactants, to prevent crossover, and to act as a proton conductor and OH^- ions conductor. This often represents a weak link

of these technologies as the Nafion membrane is typically hydrated so the working temperature is limited to around 100°C. Homogeneous thickness and good mechanical resistance are also a prerequisite of a good membrane.

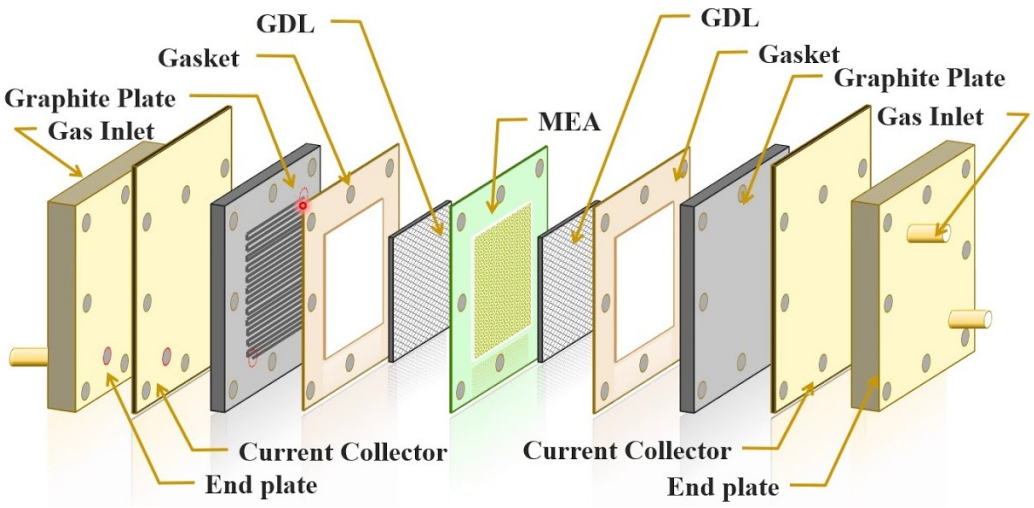

***Figure 1.5**: Schematic representation of the different components of a fuel cell device. From the outermost layer to the innermost one all the components are listed. The Membrane Electrode Assembly MEA located in the middle represents the core of this technology. Reprinted from (10).*

The catalyst layer is usually made up of a high surface area support, a carbon-based material, on top of which the electroactive material, i.e. the catalyst is supported; an ionomer, which is a species of the same nature as the electrolyte that increases the ionic conductivity to the catalyst layer, and a binder that usually is made up of a polymer (PTFE) and has the role binding all the parts together, providing extra mechanical stability to the system. It is also hydrophobic to prevent the flooding of the catalytic layer. Lastly, the Triple Phase Boundary (TPB) is the triple interface between the catalyst, the reactants, and the electrolyte; only at the TBP, the redox reaction can take place. The composition, size, morphology, stability, duration, poisoning resistance, dispersion, and degradation of the catalyst and the support are critical factors that come into play when developing a good MEA, therefore the choice of the right materials and the best support is of great importance[10].

Once the cell is assembled and ready to be tested, polarization curves are registered to characterize these devices. This is the most common characterization technique, and it implies connecting the fuel cell or the stack (a series of individual fuel cells connected in a sequence to increase the total power output) to a variable electrical load which can determine the potential output as a function of the applied electrical loading; the results are displayed in a chart reporting the potential as a function of the current density. However, the theoretical fuel cell voltage is never achieved under real operation

conditions. The cell potential departs from its maximum thermodynamic value due to multiple irreversible losses, from which the performance of the cell depends. Therefore, characterization is of fundamental importance in assessing the quality of fuel cell devices. A typical polarization curve is reported below. Three main regions can be identified and are called:

- *Activation Region*, dominant at low current densities, where typical losses are due to the activation energy barrier; electrode composition, the interaction between the electrode and the reactants, and the temperature, the concentration, and the pressure of the reactants are important parameters.
- *Ohmic region*, the region where ionic conductivity through the membrane, electron transfer resistance through the electrodes and current collectors, and losses due to electrical contacts are responsible for the overvoltage.
- *Mass Transport region*, where overvoltage is due to the concentration gradient of reactants as the electrochemical reaction proceeds, and where aspects such as slow diffusion of the fuel through the electrode's pores, and the diffusion or stagnation of products in the MEA can influence the correct behavior of the cell leading to lower performance.

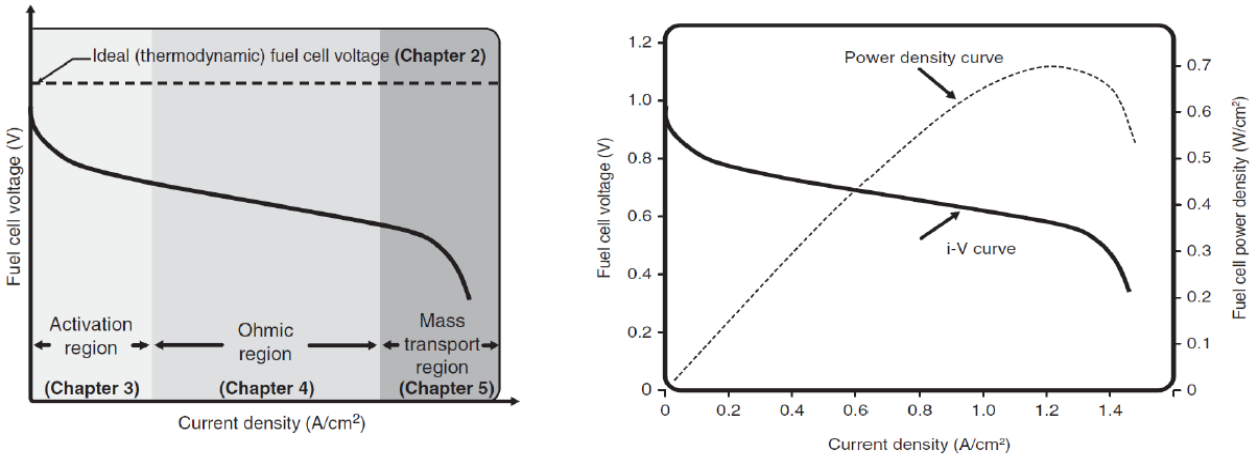

***Figure 1.6**: Example of Polarization Curves for a conventional fuel cell. As described above, the theoretical voltage is never reached; the three main regions are highlighted on the left-side graph, whereas the right-side graph shows the power density curve which is the trend of the Power (V*I) reported as a function of the current density, and it is another common representation of this characterization technique. Reprinted from (10).*

The standard reduction potential for ammonia oxidation and reaction is lower than the one of hydrogen (-0.77 V vs Standard Hydrogen Electrode (SHE) and 0.00 vs SHE), and again, a significant thermodynamic advantage can be seen when compared to water electrolysis (0.06 V, and 1.23 V)[10,11].

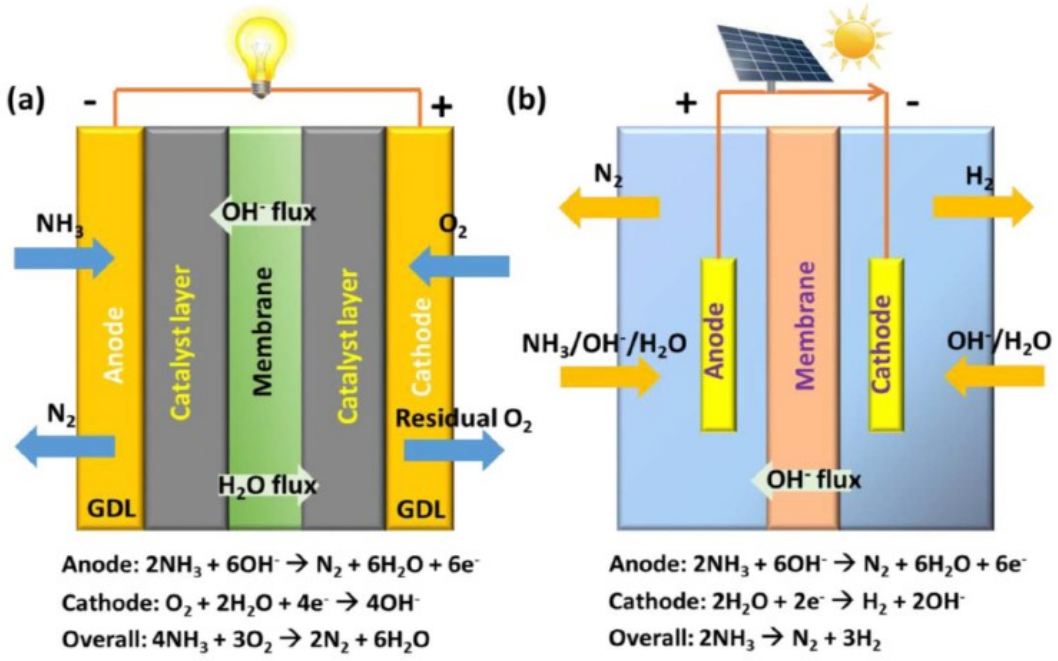

***Figure 1.7**: Schematic representation of technologies based on the eAOR. A DAFC represented on the left would use ammonia as direct fuel to produce electricity producing nitrogen as the major product. On the right, an ammonia electrolyzer used to produce clean hydrogen and nitrogen. Reprinted from (10).*

As mentioned above, the thermodynamic advantages of replacing hydrogen with ammonia are clear and it would benefit the introduction of these technologies in everyday life. As the reactions above show, in a so-called Direct Ammonia Fuel Cell (DAFC) the chemical energy of the ammonia fuel would be transformed to generate clean electricity, with the only by-products being molecular nitrogen (N_2) and water (H_2O), two non-toxic environmentally friendly compounds, and the electrooxidation of this compound requires less energy than water electrolysis. These devices are currently being studied and implemented to power heavy-duty vehicles, in maritime transportation, and agricultural vehicles as an alternative to fuels like gasoline or diesel, as it is a greener, eco-friendly, and promising movable power supply. As a matter of fact, either by using ammonia as a direct fuel or by oxidizing this compound to produce green hydrogen at the sight of operation, the prototypes and first widescale application of these devices has been observed, that will help the transition toward a green energy-based transportation system, a field that is accounted for approximately 16 percent of global greenhouse gasses (GHG) emissions, putting it on the second place as the largest source of emission worldwide[12].

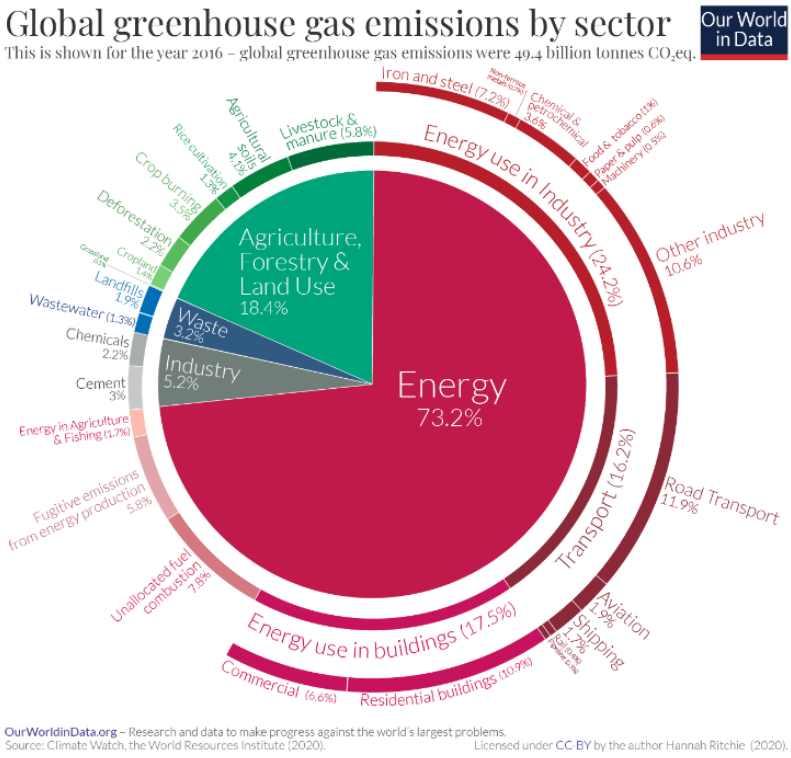

Figure 1.8*: A pie chart summarizing and highlighting the global greenhouse gas emissions (GHG) by sector for the year 2016. The total amount of GHG emissions that year was 49.4 billion tons with the energy and food and agriculture sector leading the way. Reprinted from (12).*

With this understanding of fuel cell technologies, their operating principles, and their potential application and benefits, it is now possible to describe the theoretical principle behind the reaction studied during this internship.

1.7 Electrochemical Ammonia Oxidation Reaction (eAOR)

The electrochemical oxidation of ammonia (eAOR) can take place in both basic and acidic media. In the latter case, the ammonium ion (NH_4^+) is the more stable species, however, sluggish kinetics and poor efficiency are reported when working in such conditions[8].On the other hand, it is accepted that OH^- groups are linked to the oxidation of ammonia. Studies also suggest the use of non-aqueous electrolytes to limit the formation of NO_x species[8].

Two main mechanisms were proposed and are currently largely accepted by the scientific community, i.e. via the Oswin-Salomon and the Gerischer-Mauerer mechanism. The first was developed by two scientists in 1963, who proposed the adsorption of ammonia molecules NH_{3ads} on the electrode's surface as a first step, to then be continuously dehydrogenated to form N_{ads} species while releasing electrons, eventually going for the recombination of two N_{ads} species to form the N_2 molecule. The

final step is the desorption of molecular nitrogen from the surface of the catalyst. This reaction pathway, however, presents itself with two major issues as it is accompanied by multiples rate-determining steps found at lower current densities, as the dehydrogenation from NH_{2ads} to NH_{ads} acts as the kinetics limitation, and at higher current densities where the recombination of the two N_{ads} species becomes the rate-determining step. Also, the adsorption and desorption energies of N_{ads} species must be taken into consideration as this species can cause catalyst poisoning[8,13].

The latter mechanism, described by Gerischer and Mauerer in 1970, proposes the dehydrogenation of NH_{2ads} species to form NH_{xads} (x = 1, 2) due to the presence of OH^- molecules while releasing electron, with a major difference found in the dimerization of NH_{xads} and NH_{yads} species to yield N_{2ads}, eventually forming N_2 molecules. Again, N_{ads} species are considered as possible catalyst-poisoning species[13]. This reaction is characterized by slow kinetics as it requires up to six electrons for its completion, also, the presence of multiple rate-determining steps leads to high overpotentials, and the difficulty in the selectivity leads to side reaction that could yield NOx or other toxic by-products, making this a very delicate yet very interesting reaction to be treated[8-13].

The reaction scheme of the whole mechanism as proposed is reported below:

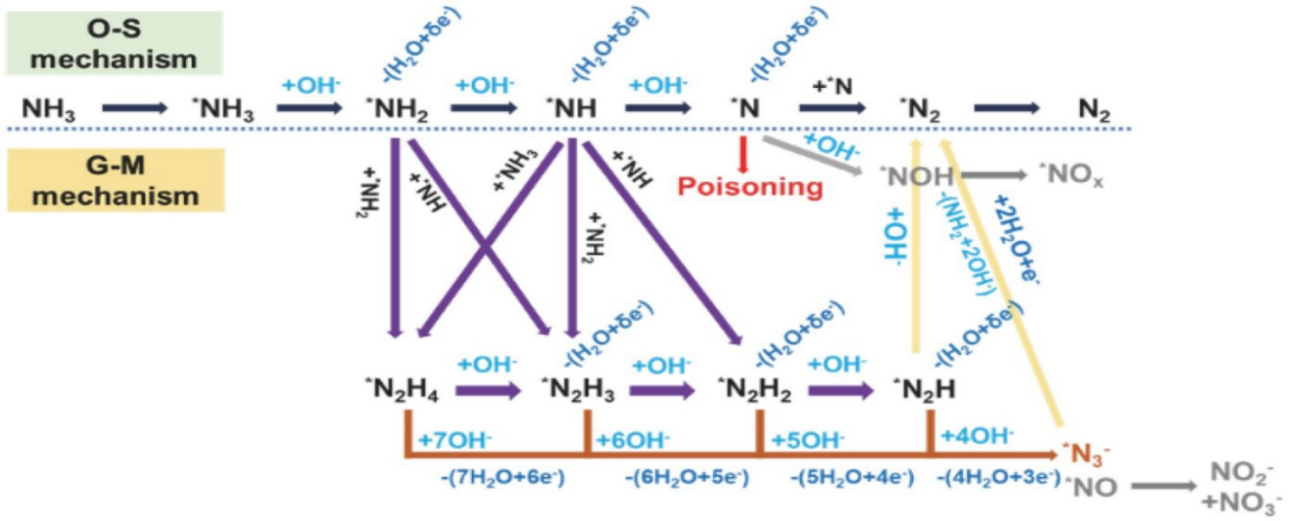

Figure 1.9: *Reaction scheme of the eAOR. In particular, both the O-S and the G-M mechanisms are represented. The sluggish kinetics and difficulty in the selectivity, as well as the catalyst poisoning, are much more understandable when looking at the complex reaction pathway proposed for this reaction. Reprinted from (8).*

From the reaction scheme it is possible to notice how the O-S mechanism could be very straightforward and efficient; however, the critical presence of adsorbed N* species could lead to

catalyst poisoning heavily influencing the whole reaction and the selectivity and formation of molecular nitrogen. The G-M mechanism, on the other hand, looks very complex, and the presence of several N_2H_x species and the many exchanged electrons required for this reaction pathway are clear indicators of the kinetic and selectivity limitation this reaction faces. As mentioned above, the yield of toxic products limits the potential of this reaction. For sure, a better understanding of the mechanism could help in the selectivity of the products but also of the intermediate species, helping in the improvement of a technological device based on this reaction[8].

Materials science plays a huge role in developing these processes, especially for discovering and implementing new catalysts, i.e., materials that can accelerate the kinetics of a specific reaction making it more accessible for technological purposes. Platinum is considered the best catalyst known not only for hydrogen production but also for the Ammonia Oxidation Reaction, as shown in the one-dimensional Sabatier Plot/Volcano Plot, where N_{ads} adsorption energy is used as a descriptor for both O-S (N+N) and G-M mechanism[8].

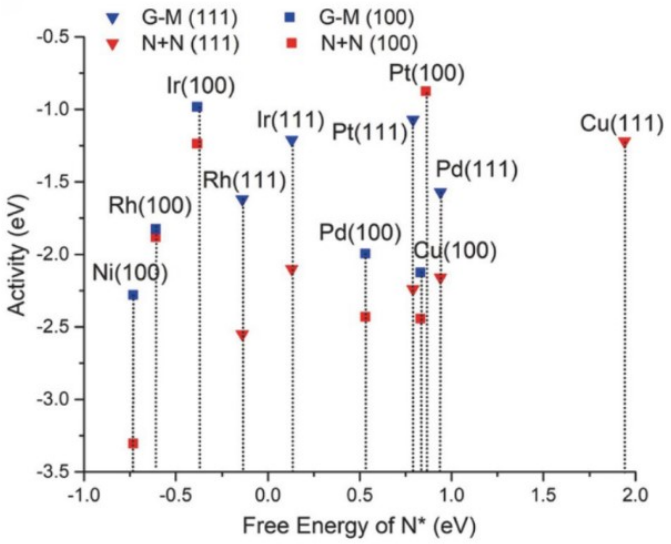

***Figure 1.10**: Volcano Plot for the possible catalysts for the eAOR. The Volcano plot was realized by taking the adsorption energies of N_{ads} species for both the O-S and G-M mechanisms for different materials and their different crystal facets. Reprinted from (8).*

Sabatier's principle states that the best catalyst is one that shows neither too strong nor too weak binding energy between the catalyst and the reactant; this is because when adsorption is too strong, degradation and poisoning of the catalyst can hinder the material's response toward the reaction of interest, while on the other hand, when adsorption is too weak, it prevents the formation of intermediates species, again leading to minor catalytic activity in the end. Such plots are useful tools

to identify the best catalyst considering the different crystal facets and their surface energy. As seen above Pt, Ir, and Rh are considered the optimal catalysts. However, the availability of these high-priced metals often clashes with geopolitical issues, making them a precious resource. Additionally, they are very sensitive to poisoning, reducing dramatically their electrocatalytic activity, therefore, great scientific endeavors are focused on replacing them with more easily accessible and less expensive materials.

Among these metals, Ni has proven itself to be the best candidate for the AOR, as its reactivity toward this reaction is supported by many scientific reviews, and its availability and costs are greatly appealing when compared to other metals. As mentioned above, both for the (O-S) and (G-M) eAOR mechanisms, adsorbed nitrogen N_{ads} is regarded as the potential catalyst poisoning species, therefore, binding energy for this species on nickel-based material must be evaluated. Nonetheless, many scientific works reported and agreed on the fact that the activity of Ni toward eAOR is due to the presence of $Ni(OH)_2$ and in particular NiOOH, which is regarded as the protagonist in the oxidation of ammonia[14].

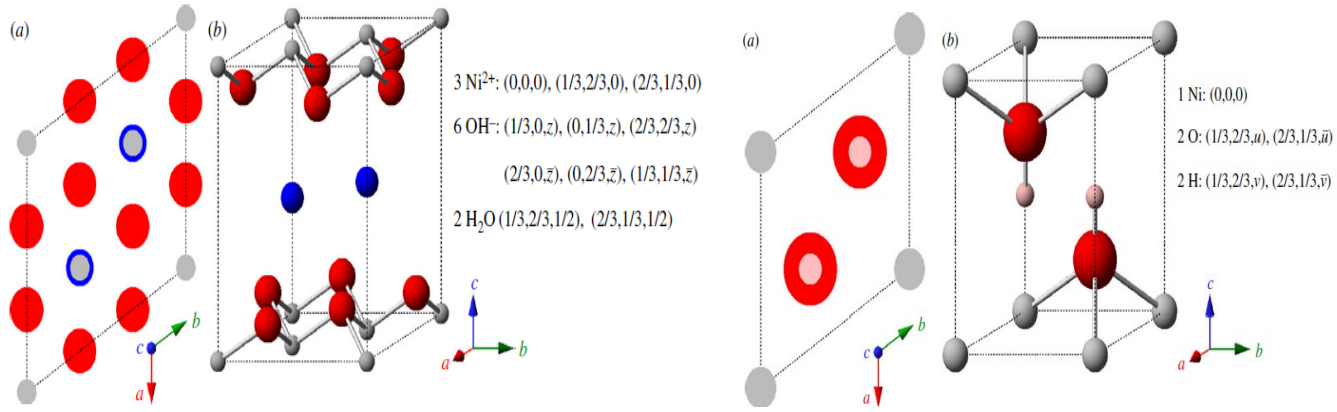

***Figure 1.11**: The crystallographic unit cell structure of α-Ni(OH)$_2$ with the coordinates of the respective atoms (Left). The crystallographic unit cell structure of β-Ni(OH)$_2$ with the coordinates of the respective atoms (Right). Reprinted from (15).*

Nickel-based materials, and especially hydroxides have been extensively studied to be implemented in battery technology and in electrochemistry in general, thus, the fundamental structure of these materials has been known for a long time and the identification of two main structures is widely accepted; in particular β-$Ni(OH)_2$, and α-$Ni(OH)_2$, are the two main crystalline structures. The first structure is the most common crystalline structure, belonging to the trigonal crystalline structure,

while the latter is formed by stacking different β-$Ni(OH)_2$ layers as depicted in Figure 1.11. It is possible to see that the α-$Ni(OH)_2$ structure allows water intercalation.

Regarding the electrochemical behavior of $Ni(OH)_2$ electrode and its reactivity toward AOR, one can obtain precious information by looking at electrochemical measurements such as Cyclic Voltammetry (CV) and Linear Sweep Voltammetry (LSV)[16]. However, the evaluation of the present phase is difficult due to the many different stable oxidation numbers that Ni and its compound possess. A Pourbaix diagram is an essential tool to evaluate the stability of a species to which an electrical potential is applied as a function of pH units. In alkaline media, Ni electrodes spontaneously turn to $NiO/Ni(OH)_2$. At the pH unit and potentials required for the eAOR the presence of Ni^{3+}(NiOOH) is favored[17]. Also, according to the Bode cycle, when an electrical potential is applied to the two phases of Nickel, this would lead to the formation of two types of oxyhydroxides during the charge and discharge process, namely the γ-NiOOH and β-NiOOH, as shown in Figure 1.12[15-19]:

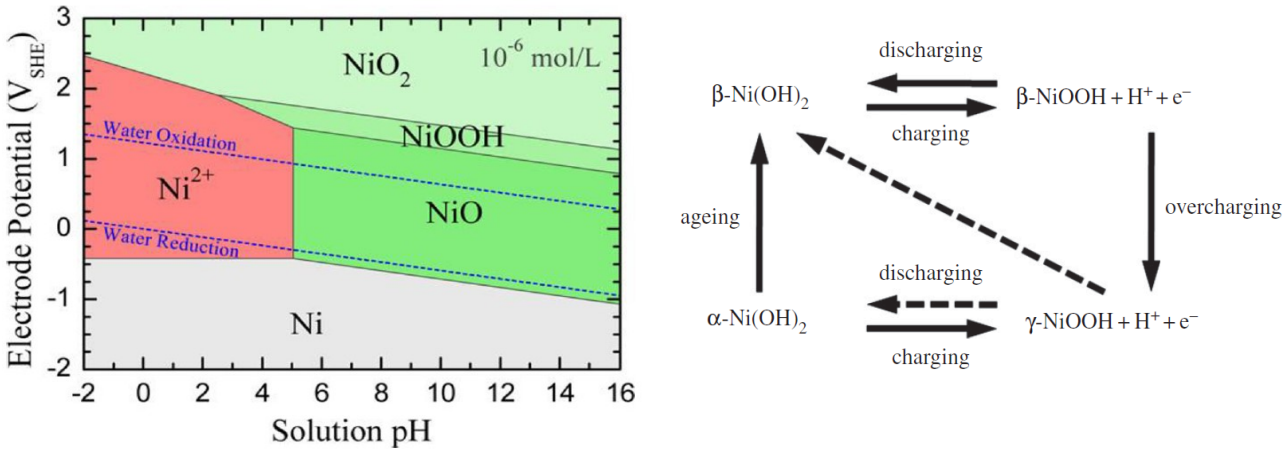

Figure 1.12: *Pourbaix diagram of Nickel (left) representing the stability of the different Ni oxidation states when a potential is applied as a function of a specific pH unit[19]. The Bode cycle (right) represents the possible pathways from the two stable forms of Nickel hydroxides (alpha- and beta-) to the oxyhydroxide (beta- and gamma-)[15]. Reprinted from (15).*

When looking at the electrochemical behavior of these electrodes in a basic media, such as NaOH + $NaClO_4$, and in the presence of ammonia a typical $Ni(OH)_2$ electrochemical response of the material during a Cyclic Voltammetry experiment would be as the one reported below:

A first oxidation peak can be appreciated at A_1 (0.35 V vs Mercury-mercurous Sulphate Electrode (MSE)) equivalent to the oxidation i.e the oxidation of $Ni(OH)_2$ to NiOOH (Ni^{2+}/Ni^{3+} couple) and a C_1 reduction peak (around 0.3 V vs MSE) corresponding to the backward redox process, that is the reduction from oxyhydroxide back to hydroxide. The presence of the A_2 peak suggests the oxidation

of ammonia concomitant to the presence of Ni^{3+}, as this is the stable species at this applied potential. In the literature, a direct electron transfer from ammonia to the catalyst is proposed, as represented in the following reaction:

$$NiOOH + NH_3 \rightarrow NiOOH(NH_{3,ads}) \rightarrow NiOOH + ½N_2 + 3H^+ + 3e^- \quad (1.1)$$

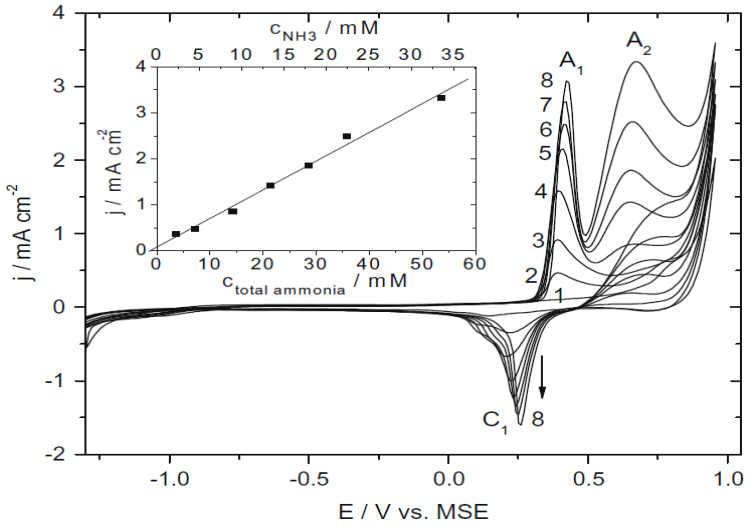

***Figure 1.13**: Typical electrochemical response of a Nickel-based catalyst used for the electrochemical oxidation of ammonia. A Cyclic Voltammetry is represented showing the oxidation peak of Ni^{2+} to Ni^{3+} followed by the A_2 peak corresponding to the oxidation of ammonia. The reduction of the oxyhydroxide back to hydroxide is visible[16]. Reprinted from (16).*

To further support this, the intensity of the C_1 peak does not decrease as the ammonia concentration is increased suggesting that NiOOH does not reduce back to the hydroxide form.

The pH of the solutions is not only important regarding the stability of the Ni catalyst but also for the ammonia itself. As mentioned above, the eAOR can be carried out both in acidic and basic media; however, as pH increases a shift toward a higher potential for the eAOR is visible, and a limit case in very basic solution where the oxidation overlaps with another reaction, namely the Oxygen Evolution Reaction (OER). Considering the oxidation of the hydroxide to the oxyhydroxide at a potential of 1.30-1.35 V vs RHE, and that the eAOR takes place at around 1.4 V vs RHE, it is also important to consider the Oxygen Evolution Reaction (OER) that takes place at potentials only ca. 0.02 V higher. This comes with some important consequences, as it lowers efficiency and leads to the formation of nitrogen oxides (NO_x), toxic and environmentally unfriendly compounds. Research papers suggest the formation of these species through oxidation processes of $NH_{x,ads}$ species[19]. For this reason, the comprehensive study of the whole reaction, both the mechanism and the selectivity, is important to

optimize energy efficiency, avoiding losses and production of toxic by-products that seem to predominate over the production of N_2 for potentials higher than 1.5 V vs RHE. Operando characterization techniques could play a big role in helping to determine the accurate reaction pathway, poisoning species, and reaction products as they allow to have insight into critical aspects of the reaction that are often not accessible with conventional ex-situ characterization techniques.

Modification of Ni-based materials with other metals is also a strategy to optimize this reaction. In particular, the addition of many metals like (Mn, Co, Ru, Au, and Ir) to the Nickel structures to study this reaction, is receiving great attention; however, studies show that only Cu seems to boost the reactivity[18,20]. Supposedly, Cu atoms can help the dimerization and allow better desorption of adsorbed products; the synergic effect of Ni and Cu could be the key to making eAOR kinetically faster[18-20]. Furthermore, the great abundance of Cu and its modest price would be greatly beneficial to these technologies, and sustainable in the long-term reducing manufacturing costs.

1.8 Thesis Project

This work focuses on the synthesis of $Ni(OH)_2$ nanoparticles with different morphologies to determine the activity of this material toward the eAOR. In particular, different morphologies, (as properly described in the Experimental Section) were tested to evaluate any structural preferences for the reaction of interest; eventually, modification of these morphologies was also studied and in particular, the activity toward the eAOR was evaluated after the introduction of Cu atoms, one of the other metals whose activity was proven as reported in the scientific literature available up to date. The materials were tested and characterized using conventional electrochemical techniques such as Cyclic Voltammetry (CV) and Linear Scanning Voltammetry (LSV) to determine information like the onset potential of the reaction. Additionally, differential electrochemical mass spectrometry (DEMS), was used for in-situ characterization of materials to obtain information on reaction products, particularly volatile or gaseous products such as O_2, N_2, and NO_x. Besides, physicochemical characterization techniques such as X-ray Diffraction (XRD), X-ray Photoelectron Spectroscopy (XPS), Scanning Electron Microscope and Energy Dispersive X-Rays Analysis (SEM/EDX), Inductively Coupled Plasma Mass Spectroscope (ICP-MS), and Transmission Electron Microscope (TEM) were used to obtain further information on the composition, the crystalline, and surface structure of the obtained materials and to verify the presence of the expected morphology.

Bibliography

1. *Climate Change and Human Behaviour. Nat. Hum. Behav.* **6,** 1441–1442 (2022).
2. Eyring, V., Gillett, N. P., Achuta Rao, K. M., Barimalala, R., Barreiro Parrillo, M., Bellouin, N., Cassou, C., Durack, P. J., Kosaka, Y., McGregor, S., Min, S., Morgenstern, O. & Sun, Y. Human Influence on the Climate System. In *Climate Change 2021: The Physical Science Basis. Contribution of Working Group I to the Sixth Assessment Report of the Intergovernmental Panel on Climate Change* [Masson-Delmotte, V., Zhai, P., Pirani, A., Connors, S. L., Péan, C., Berger, S., Caud, N., Chen, Y., Goldfarb, L., Gomis, M. I., Huang, M., Leitzell, K., Lonnoy, E., Matthews, J. B. R., Maycock, T. K., Waterfield, T., Yelekçi, O., Yu, R. & Zhou, B. (eds.)]. 423–552, Cambridge Univ. Press (2021).Paris Agreement. United Nations Treaty Collection, Chapter XXVII 7. d, adopted December 12, 2015, and in force November 4, 2016. Article. Available at: https://treaties.un.org/pages/ViewDetails.aspx?src=TREATY&mtdsg_no=XXVII-7-d&chapter=27&clang=_en.
3. *Paris Agreement.* United Nations Treaty Collection, Chapter XXVII 7.d (2015), available at https://treaties.un.org/pages/ViewDetails.aspx?src=TREATY&mtdsg_no=XXVII-7-d&chapter=27&clang=_en.
4. *Paris Agreement.* United Nations Treaty Collection, Chapter XXVII 7.d (2015), available at https://treaties.un.org/pages/ViewDetails.aspx?src=TREATY&mtdsg_no=XXVII-7-d&chapter=27&clang=_en.
5. McKinsey & Company, Global Energy Perspective 2023: Oil outlook , January 24, 2024, https://www.mckinsey.com/industries/oil-and-gas/our-insights/global-energy-perspective-2023-power-outlook.
6. Ma, N., Zhao, W., Wang, W., Li, X. & Zhou, H. Large scale of green hydrogen storage: Opportunities and challenges. *Int. J. Hydrog. Energy* **50,** 379–396 (2024).
7. Guthrie, S., Giles, S., Dunkerley, F., Tabaqchali, H., Harshfield, A., Ioppolo, B. & Manville, C. *Impact of ammonia emissions from agriculture on biodiversity: An evidence synthesis.* RAND Corporation, Santa Monica, CA (2018).
8. Lee, S. A., Lee, M. G. & Jang, H. W. Catalysts for electrochemical ammonia oxidation: Trend, challenge, and promise. *Sci. China Mater.* **65,** 3334–3352 (2022).
9. International PtX Hub. Ammonia Transport & Storage, January 2024. Available at: https://ptx-hub.org/wp-content/uploads/2024/01/International-PtX-Hub_202401_Ammonia-transport-and-storage.pdf.

10. Mohd Adli, N., Zhang, H., Mukherjee, S. & Wu, G. Review—Ammonia Oxidation Electrocatalysis for Hydrogen Generation and Fuel Cells. *J. Electrochem. Soc.* **165,** J3130–J3147 (2018).
11. Mohd Adli, Nadia & Zhang, Hao & Mukherjee, Shreya & Wu, Gang. (2018). Review—Ammonia Oxidation Electrocatalysis for Hydrogen Generation and Fuel Cells. Journal of The Electrochemical Society. 165. J3130-J3147. 10.1149/2.0191815jes.
12. Ritchie, H. Sector by sector: where do global greenhouse gas emissions come from? *Our World in Data* (2020). Available at: https://ourworldindata.org/ghg-emissions-by-sector.
13. Oswin, H. G. & Salomon, M. The anodic oxidation of ammonia at platinum black electrodes in aqueous KOH electrolyte. *Can. J. Chem.* **41,** 1686–1694 (1963).
14. Kapałka, A., Cally, A., Neodo, S., Comninellis, C., Wächter, M. & Udert, K. M. Electrochemical behavior of ammonia at Ni/Ni(OH)$_2$ electrode. *Electrochem. Commun.* **12,** 18–21 (2010).
15. Hall, D. S., Lockwood, D. J., Bock, C. & MacDougall, B. R. Nickel hydroxides and related materials: a review of their structures, synthesis and properties. *Proc. R. Soc. A* **471,** 20140792 (2015).
16. Vidal-Iglesias, F. J., Solla-Gullón, J., Feliu, J. M., Baltruschat, H. & Aldaz, A. DEMS study of ammonia oxidation on platinum basal planes. *J. Electroanal. Chem.* **588,** 331–338 (2006).
17. Łuczak, J. & Lieder, M. Nickel-based catalysts for electrolytic decomposition of ammonia towards hydrogen production. *Adv. Colloid Interface Sci.* **319,** 102963 (2023).
18. Herron, J. A., Ferrin, P. & Mavrikakis, M. Electrocatalytic oxidation of ammonia on transition-metal surfaces: A first-principles study. *J. Phys. Chem. C* **119,** 14692–14701 (2015).
19. Vidal-Iglesias, F. J., Solla-Gullón, J., Feliu, J. M., Baltruschat, H. & Aldaz, A. DEMS study of ammonia oxidation on platinum basal planes. *J. Electroanal. Chem.* **588,** 331–338 (2006).
20. Xu, W., Lan, R., Du, D., Humphreys, J., Walker, M., Wu, Z., Wang, H. & Tao, S. Directly growing hierarchical nickel-copper hydroxide nanowires on carbon fibre cloth for efficient electrooxidation of ammonia. *Appl. Catal. B Environ.* **218,** 470–479 (2017).

CHAPTER 2

2.1 Electrochemistry: Theory and Conventional Electrochemical Characterization

For the study of the eAOR, conventional electrochemical techniques like Cyclic Voltammetry (CV), and Linear Sweep Voltammetry (LSV) were used. Herein, the theoretical aspects of these techniques will be discussed, as well as the description of the electrochemical cell and its setup.

Electrochemistry is the branch of chemistry studying the redox process, any reaction involving an electron transfer in solution accompanied by a reduction reaction or oxidation reaction. To better understand an electrochemical process (Figure 2.1), it is helpful to think about it as a series of subsequent steps accompanied by at least an electron transfer (ET) process. A potential redox species in solution must diffuse from the bulk of the solution toward the interphase between the active surface and the electrolyte to undergo electron transfer and any redox reaction. The diffusion process is commonly referred to as the 'mass transfer' process, while the electron transfer process is referred to as the 'charge transfer' process. Also, the adsorption of the species on the surface and the subsequent desorption of the formed product are necessary conditions to be satisfied for an electrochemical process to take place. Each step can potentially represent the rate-determining step (r.d.s.), that is, the step by which the rate of the whole reaction is limited.

The definition of the rate-determining step often categorizes electrochemical processes, in particular:

- *Reversible Systems*: systems characterized by a fast electron transfer which are only limited by diffusion processes that are considered the rate-determining step. Diffusion from the bulk determines the number of species that will undergo a redox reaction.
- *Irreversible Systems*: systems characterized by a fast diffusion from the bulk of the solution to the interphase, yet slow charge transfer, thus making electron transfer the rate-determining step.
- *Quasi-Reversible Systems*: systems in which both diffusion processes and electron transfer processes are considered the rate-determining step.

A glass cell is filled with the supporting electrolyte (and any other solution containing reactants if necessary to the reaction), in which three electrodes are placed to perform the measurement. A brief description of the different components of the cell is given:

- Working Electrode (WE): this is the electrode where the reaction under investigation takes place. The catalytic material is often supported on an inert material, and the current variation as a function of the applied potential is registered.

- Counter Electrode (CE): is necessary to close the amperometric circuit formed together with the WE; usually the reaction occurring at the CE is the backward reaction concerning the one occurring at the WE.
- Reference Electrode (RE): is necessary to close the potentiometric circuit with the WE; this electrode has a very fast equilibrium, making it possible to appreciate the variation of applied potential to the WE concerning the RE, the unpolarizable electrode.

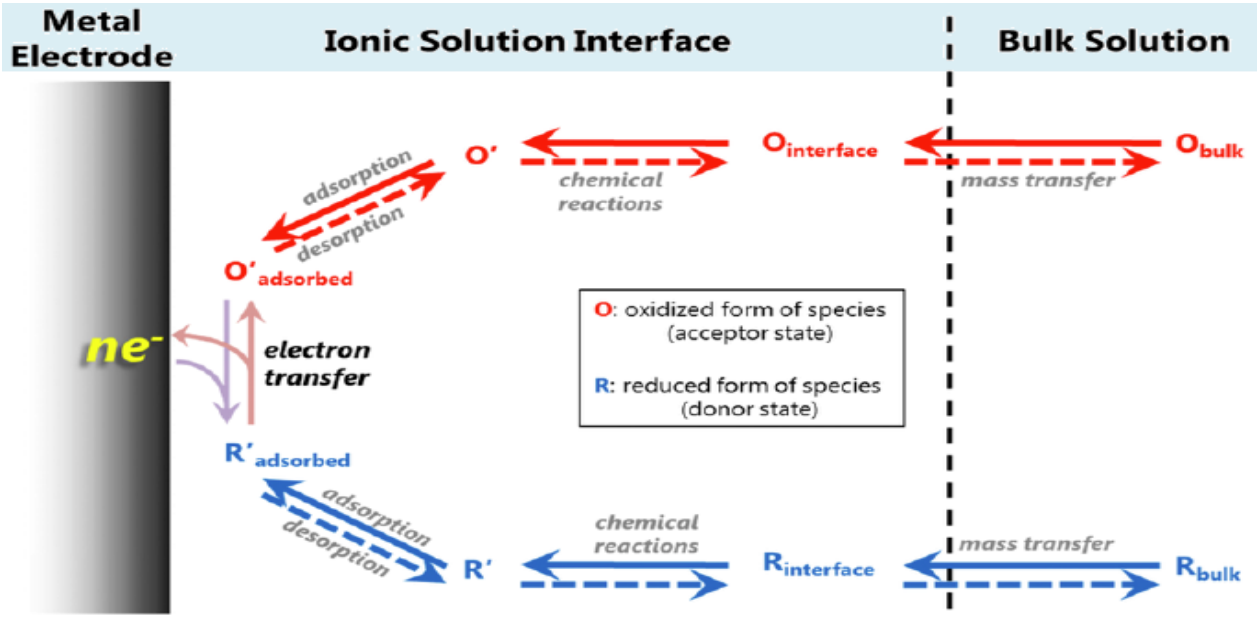

***Figure 2.1**: Schematic representation of a typical electrochemical process taking place. Mass transfer from the bulk of the solution, and charge transfer between the surface and the active chemical species takes place at the interphase. The adsorption and desorption processes of the oxidized and reduced species are also represented because of their importance in such a process. Reprinted from (1).*

The electronic hardware that allows the modification of the WE potential concerning the RE ongoing and the current response passing through the electrode as the electrochemical process is ongoing is called potentiostat. When working in such a system, i.e. an electrode in solution involving an electron transfer process, two limit cases are usually described, and necessary conditions are to be satisfied to properly describe the system. The first condition states that at equilibrium (when no net current is passing through the electrodes) the electrode's potential is determined by the concentration of oxidized and reduced species in solution, according to the Nernst equation[1]:

$$E = E° + (RT/nF)ln(C_R/C_O) \quad (2.1)$$

Where E^0 is the standard redox potential of the species in solution, 'n' is the number of exchanged electrons, 'F' the Faraday constant (96,485.33 C/mol), 'R' is the universal gas constant (8.314 J/mol K), and C_R/ C_O the ration between the concentration of reduced and oxidized species.

The other case describes the situation when a net current passes through the electrode; in this case, the potential of the electrode is dictated by the Tafel equation[1]:

$$\eta = a + blog(i) \tag{2.2}$$

The two parameters '*a*' and '*b*' are called Tafel constants, and they are characteristic of an electrochemical process. The parameter 'η' is known as 'overpotential', which is the potential difference between the applied and the theoretical potential ($\eta = E - E^0$) and is an important parameter to understand the system and how far the equilibrium condition is.

The overpotential can usually be attributed to different aspects such as charge or mass transfer effects, where in the first case the slowness of the electron transfer through the electrode's surface and the species in solution is responsible for the difference with the equilibrium potential, or in the latter case, the speed with which a redox species reaches or leaves the electrode's surface. Also, ohmic contributions are usually present, mainly due to the electrolyte composition or the electrode itself, and can cause electrical resistance. Lastly, chemical reactions can often be accompanied by sluggish kinetics and the presence of radicals, or intermediate species reacting with each other causing overpotentials[1,2]. It is clear then how overpotential affects an electrochemical measurement; higher overpotentials require more energy for the same reaction to occur whereas for lower overpotentials the energy demand is lower. The search for good catalysts and optimizing the experimental setup for the electrochemical reaction under investigation is therefore of paramount importance.

2.2 Cyclic Voltammetry (CV)

Cyclic Voltammetry (CV) is a powerful and largely employed electrochemical characterization technique that allows one to obtain information about the system under investigation[1,2]. Important information about the redox potential of species as well as thermodynamic parameters and kinetics of a reaction are accessible via this technique. In this technique, a linear potential is applied to the working electrode, and the electrochemical response, i.e. the current passing through the working electrode is registered. The applied potential varies within a specific potential window with a definite scan rate, usually taking the form of a pyramid shape curve; Overall, the potential variation can be expressed by the following mathematical equation[1,2]:

$$E(t) = Ei - 2v\lambda + vt \tag{2.3}$$

Where E_i is the initial applied potential, 'v' is the scan rate, 't' is the elapsed time, and 'λ' is a parameter linked to the inversion potential E_λ, that is the potential at the time at which the applied potential changes its sign. The mathematical relation described above represents the trend of the potential as a function of time, as shown in Figure 2.2.

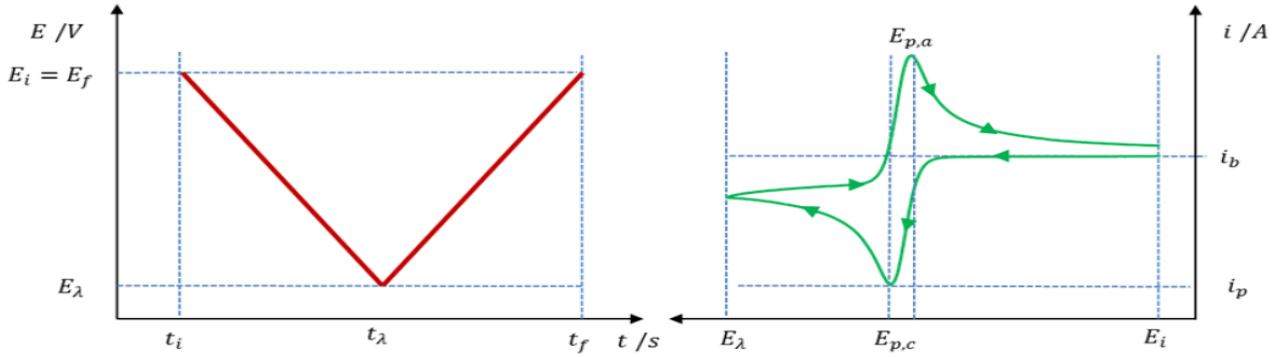

***Figure 2.2**: Scheme representation of the trend of the applied potential (left) in a Cyclic Voltammetry measurement. The common pyramid-shaped trend is appreciated; the initial potential E_i and the final potential E_f usually coincide in such measurements, although it is not strictly necessary. Also, the inversion potential E_λ is the potential's value before the trend reverses its sign. The common representation of the Cyclic Voltammetry measurement (right) is one where the registered current is plotted as a function of the applied potential. Important parameters such as the anodic peak potential value $E_{p,a}$ and the cathodic peak potential value $E_{p,c}$ can be retrieved. Reprinted from (2).*

However, for a typical CV experiment, it is preferred to represent the registered current as a function of the applied potential, as shown on the right side of the (above) picture. As the applied potential varies, the current response can be divided into capacitive current and faradaic current. The first is the current due to the polarization of the electrode and the presence of the double layer, which is the accumulation of counterions near the electrode surface, concomitant with the depletion of co-ions due to the polarization of the electrode's surface. These currents are very low and are responsible for the current being different from zero when no electron transfer process is happening between a redox species and a catalyst. When the applied potential equals the potential at which a redox reaction can occur, the current response will dramatically vary, producing a characteristic peak in the voltammogram corresponding to an oxidation process ($i > 0$) or a reduction process ($i < 0$) (or multiple peaks if a specie is capable of undergo multiple ET processes in the same potential window). This is the faradaic response, i.e. when an electron transfer process is occurring between a catalyst and a redox specie in solution.

The electrode potential influences the concentration profiles of the redox species, thus the shape of the voltammogram carries useful information and particular attention may be given to the peak position, height, width, and separation of the peaks. When the potential applied is less than the redox potential of the species, the concentration profiles of the oxidized and reduced species are equal, and only capacitive currents are registered. By increasing the applied potential, the concentration gradient varies and so does the current response up to the half-wave potential, where the concentration of the oxidized species is the same as the reduced one; at peak potential, the concentration gradient will have its highest value. Beyond the peak, even if applying higher potentials, the current values will decrease according to the Cotrell equation ($i \propto t^{-1/2}$), decaying exponentially with time as mass transfer processes become the rate-determining steps[3].

With this knowledge of the facts, it is possible to understand a voltammogram and why significant differences arise in the case of a reversible or irreversible process, as the behavior of the redox species and the electrode is influenced by diffusion and charge transfer, as mentioned above. In the first case, the process is also called 'Nernstian', and is characterized by a fast equilibrium, or in other terms, a fast electron transfer process. A reversible process is also characterized by a peak width (E_p-$E_{p/2}$) of 56.5/n mV at T = 25°C. This is a characteristic value for Nernstian processes and has been proven independent of the scan rate. The current response and therefore the shape of the peak is determined by the Randles-Sevcik equation reported below[1,2]:

$$i_{p,rev} = 0.4463nFAC_0D_0^{1/2}(nF/RT)^{1/2}\nu^{1/2} \quad (2.4)$$

where 'n' is the number of exchanged electrons, 'F' the Faraday constant (96485.33 C/mol), 'A' (cm^2) the surface area of the electrode, 'C_0^*' (mol/cm^3) the bulk concentration of the species, 'D_0' (cm^2/s) the diffusion coefficient of the specie, 'T' the temperature, 'R' the universal gas constant (8.314 J/mol K) and 'ν' (mV/s) the scan rate.

The latter case is characteristic of a slow electron transfer process so that the diffusion processes are faster than the charge transfer process: in this case, the oxidation and reduction peaks will show a greater separation when compared to a Nernstian process, or there will be the complete absence of the backward peak in the chosen potential window. The mathematical expression is the following and it introduces a parameter 'α' known as the 'electron transfer coefficient' ($0 < \alpha < 1$)[1,2]:

$$i_{p,irr} = 0.4958nFAC_iD_i^{1/2}(\alpha F/RT)^{1/2}\nu^{1/2} \quad (2.5)$$

Usually, $i_{p,\,irr} << i_{p,\,rev}$, and it is interesting to note the square root dependence of the scan rate 'ν' (mV/s). This is an essential aspect of electrochemistry as the scan rate variation allows modification

of the double layer thickness, dramatically altering the electrochemical response, i.e. recording higher currents for higher scan rates. However, for a Nernstian process, one can prove that the peak potential is determined by the following relation[1,2]

$$E_P = E_{1/2} - 1.109(RT/nF) = E_0 - (RT/nF)ln(D_O/D_R)^{1/2} \quad (2.6)$$

That highlights the remarkable fact that the peak potential is not a function of the scan rate 'ν' (mV/s) and that thermodynamical parameters such as the standard redox potential E^0 of that species is an accessible piece of information. On the contrary, for an Irreversible process, the peak position is a function of the scan rate 'ν' (mV/s).

2.3 Linear Sweep Voltammetry (LSV)

Linear Sweep Voltammetry (LSV) is another common and powerful electrochemical characterization technique. As for the CV, a potential is applied to the working electrode concerning the reference electrode; however, the potential varies linearly starting from an initial value of E_i to a final value of E_f. These two values are different, so the potential trend is linear and not a pyramid-shaped trend as in the CV.

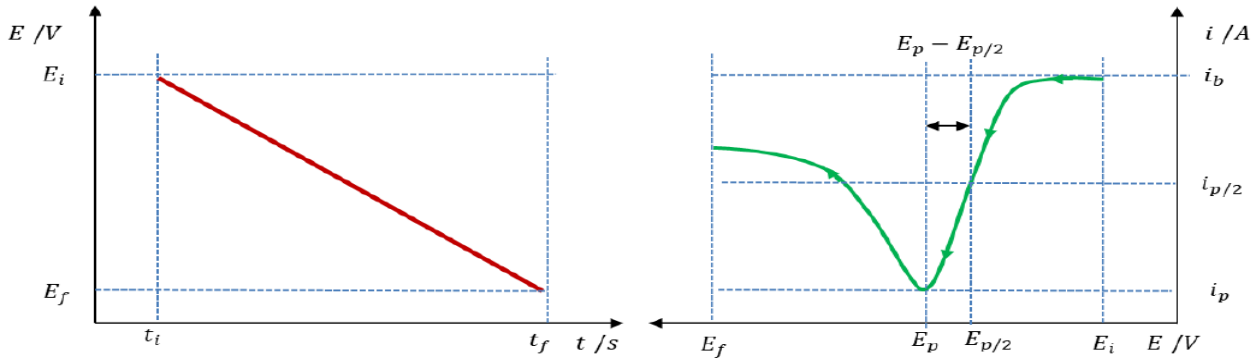

***Figure 2.3**: Scheme representation of the trend of the applied potential (left) in a Linear Sweep Voltammetry measurement. The linear trend of the potential is appreciated; the initial potential E_i is linearly increased with time to reach the final potential E_f. The common representation of the Linear Sweep Voltammetry measurement (right) is one where the registered current is plotted as a function of the applied potential. Important parameters such as the peak potential value E_p, the peak width $E_p - E_{p/2}$, and halfwave potential $E_{p/2}$ cn be retrieved. Reprinted from (2).*

The shape of the peak follows the same theoretical guidelines as the one described for Cyclic Voltammetry. The initial applied potential is not enough to alter the equilibrium condition; therefore, the registered current only refers to a capacitive current. As the applied potential increases so does the current, highlighting the variation in the concentration gradient of the oxidized and reduced

species. The peak value of the current is reached as the concentration gradient reaches its highest value. Again, as the applied potential increases beyond the peak value of the current, the registered current decays exponentially as described by the Cotrell equation[3]. As for the CV, useful information about the process under investigation is found in the onset potential E_{on}, the peak width (E_p-$E_{p/2}$), and the peak current i_p.

2.4 Tafel Analysis

The Tafel analysis in electrochemistry is a method used to study the kinetics of electrode reactions. Classically, Tafel analysis has been used to great effect in the analysis and elucidation of the catalytic activity of various metal surfaces towards the hydrogen evolution reaction and oxygen evolution reaction[4]. It involves plotting the logarithm of the current density, i.e. the net current normalized by the electrochemical surface area or geometrical area of the electrode, against the overpotential to determine the Tafel slope. The Tafel slope provides information about the reaction mechanism and rate-determining steps (rds) of the electrochemical process; by analyzing this slope, it is possible to access information about the reaction kinetics and mechanisms occurring at the electrode surface by looking at parameters such as the exchange current density j_0, that is the total current flowing across the interface when the potential is equal to the reversible or equilibrium potential of the reaction; and the transfer coefficient 'α', that is a kinetic parameter which serves as an objective descriptor of how the electrodes' potential variation affects the activation energies of the cathodic and anodic processes and the slope value $\frac{\delta\eta}{\delta log i}$.

Typical Tafel slope values are linked to a specific process happening in the electrochemical system. The Oxygen Evolution Reaction (OER) is part of the water splitting reaction, and it is considered the bottleneck in total efficiency due to its sluggish kinetics[7,8,9]; in fact, the standard potential is 1.23 V, however the real potential is usually much higher, reaching up to 2.0 V[8,9]. Its mechanism is composed of four electron transfer steps, both in acidic and alkaline media; under acidic conditions, water is oxidized, producing H^+ and e^- species, as well as releasing O_2, hence the name of the reaction. In basic media, OH^- groups are oxidized to water and oxygen, releasing electrons in the process. Equations (2.7)-(2.11) describe the mechanism for the OER in alkaline media and the values for the different Tafel slopes when each step acts as *rds*[9]:

$$OH^-_{aq} \rightleftarrows OH_{ads} + e^- \qquad (\mathbf{118\ mV\ dec^{-1}})(\mathbf{2.7})$$

$$OH^-_{aq} + OH_{ads} \rightleftarrows O_{ads} + H_2O + e^- \qquad (\mathbf{40\ mV\ dec^{-1}})(\mathbf{2.8})$$

$$OH^-_{aq} + O \rightleftarrows HOO_{ads} + e^- \qquad (\mathbf{24\ mV\ dec^{-1}})(\mathbf{2.9})$$

$$OH^-_{aq} + HOO_{ads} \rightleftarrows OO_{ads} + H_2O + e^- \qquad (\mathbf{20\ mV\ dec^{-1}})(\mathbf{2.10})$$

$$OO_{ads} \rightleftarrows O_{2_g} \qquad (\mathbf{17\ mV\ dec^{-1}})(\mathbf{2.11})$$

It is possible to see that all the reaction intermediates are bound to the surface; the properties of these species and their stability depend on the reaction conditions (such as pH) and the catalyst materials, and each one of them can represent the rds and so affect the general rate of the reaction[9]. The value of the slopes is an important indicator of the activity of a catalyst, as this means a smaller overpotential is required to reach a higher current density; as mentioned above, the overpotential is a crucial aspect in electrochemistry, therefore the Tafel analysis is a powerful tool to evaluate the catalyst performance toward the reaction of interest.

Different reactions can follow various paths, however, the Tafel analysis remains a valuable tool for elucidating any dependence on adsorption or desorption mechanisms and their energetics, in particular in understanding the rate-determining step. Therefore, it is important to know which processes are taking place in the reaction of interest to perform the correct Tafel analysis.

This can be useful to understand better the rate determining step in ammonia oxidation and any possible effect induced by the Oxygen Evolution Reaction (OER) happening at very close potential. In the case of eAOR two mechanisms are proposed as already mentioned (Oswin-Solomon or Gerischer-Mauerer). Ammonia oxidation involves consecutive adsorption-desorption steps and multiple electron transfers and the two mechanisms proposed slightly different reaction pathways, therefore, determination with Tafel analysis of the rate-determining step could help to understand the preferred reaction pathway better, and in particular, if the electron transfer process involved in the dehydrogenation of the $NH_{x,ads}$ species is indeed a rate-determining step. Ultimately, it will give additional and valuable information about the catalytic performance of the catalyst toward this multistep-mechanism reaction.

2.5 Electrochemically Active Surface Area (*ECSA*)

Current scientific endeavors are focused on finding better catalysts for many important electrochemical reactions and exploiting them to realize new technologically relevant devices. The amount of data collected throughout different laboratories with different experimental setups is huge, therefore, the definition of the correct 'figure of merits' to ensure a fair comparison of the performance of these materials is critical[8]. Key factors such as activity, selectivity, and durability are crucial

parameters when a new catalyst is tested and evaluated. It is now widely accepted, yet still highly debated, that the evaluation of a specific electrochemical parameter called 'Electrochemically Active Surface Area' *(ECSA cm^2)* represents an important and reliable figure of merit that allows the comparison of different structural properties of a catalyst from an electrochemical point of view.

The *ECSA* can be calculated with a variety of methods; one method is the determination of the coulomb charge associated with adsorption and desorption processes such as hydrogen adsorption/desorption for materials like Platinum. An example of the peak integration method can be seen in Figure 2.4.

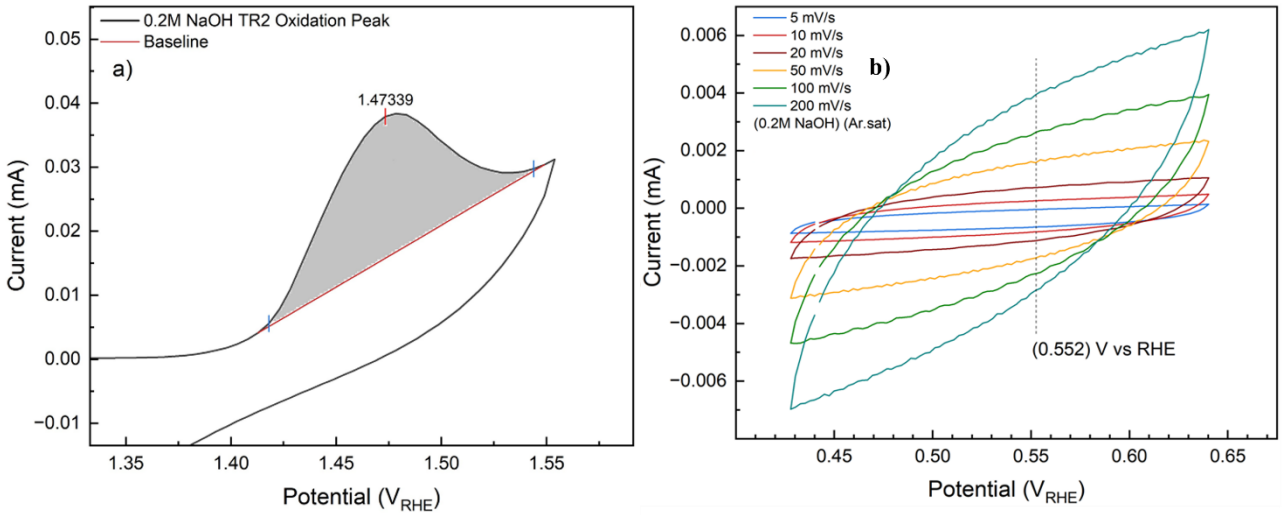

***Figure 2.4**: Peak integration method for the ECSA determination (left). The area under the peak is proportional to the charge and therefore to the number of active catalyst sites. The double-layer or capacitance method (right) showcasing different CV at increasing scan rate, with current values selected at 0.552 V vs RHE*

A second procedure to determine the active surface area is the 'double-layer' or 'capacitance methods' which defines the *ECSA* as[8.11]:

$$ECSA(cm^2) = \frac{C_{dl}}{C_s} \tag{2.12}$$

Where C_{dl} is the double-layer capacitance, often expressed as (µF), and C_s is the specific capacitance of the material under investigation, expressed in (µF/ cm^2). However, the exact determination of the latter parameter is difficult and not yet strictly regulated; as a matter of fact, it is common practice to use a single value for this parameter leading to large over- or underestimation. To obtain the double-layer capacitance it is necessary to conduct several Cyclic Voltammetry at different scan rates of the material under investigation in a potential window where no faradaic processes are being carried out, and the only contribution to the registered current is that of capacitive processes, i.e. the double-layer of the electrode under study. To calculate the double-layer capacitance C_{dl} one must select a specific

value of the registered current for every scan rate, then, when plotting the current versus the different scan rates one can obtain the double-layer capacitance with a linear regression of the plotted data.

The ECSA with the double-layer method is finally obtainable by applying the mathematical relation mentioned above. Another common way to establish the *ECSA* is by integrating the area under the redox peaks obtained in the electrochemical measurement. In this way, a more accurate value is obtained as it is known that the area under the curve is proportional to the charge which is proportional to the precise number of the catalyst's electroactive sites generating that redox peak, i.e. the registered current corresponding to a Faradaic process. When the area under the curve is known, one can divide this value with specific charge density 'q_s', which is the value describing the two-electron transfer to form one monolayer of $Ni(OH)_2$, and for the scan rate 'ν_{scan}'[10,11,12]. Once the area under the curve (A) is known, the correct mathematical expression is[8,11]:

$$ECSA\ (cm^2) = \frac{A}{q_s \nu_{scan}} \tag{2.13}$$

In this way, the ECSA with the peak integration method is calculated.

2.6 Experimental Procedure and Setup: Electrochemical Cell Setup

For this study, NOVA Software connected to a Potentiostat (MetroOhm Autolab) was used to control the voltage applied to the electrode concerning the reference electrode and collect the current signal corresponding to the electrochemical process in the cell. The cell was a glass cell equipped with a five-hole plastic cap, through which the various electrodes and other components such as Luggins tube or a bubbler were inserted. The WE consisted of a Glassy Carbon Electrode (GCE) on a Rotating Disk Electrode (RDE) Tip, on top of which the synthesized catalyst was deposited. The CE was a Glassy Carbon Electrode rod, and the RE was a Reversible Hydrogen Electrode (RHE). This consisted of a sealed glass tube in which a Platinum wire was inserted; the sealing is necessary to allow the introduction of the electrolytic solution in the glass chamber where the platinum wire is inserted, to allow the electrical connection and ensure the same pH and solution as the electrochemical cell. With the help of a power supply generator, the RHE was activated producing a hydrogen bubble inside the glass cavity by applying around 10 V, and it was then inserted into a Luggins tube filled with the same supporting electrolyte as the one inside the cell, and finally introduced into the electrochemical cell. As mentioned above, the WE consisted of the catalyst deposited on a glassy carbon electrode. To do this, the material must be dispersed in ink before drop-casting it on the electrode's surface.

2.7 Catalyst Ink

An ink is usually composed of a catalyst, an ionic conductor, and solvents like a solution of alcohol and water. The typical preferred ionic conductor is Nafion. This was developed in the late 60s through a modification of Teflon (a perfluoro polyethylene chain) by adding side chains of perfluoro ethylene oxide sulfonic groups in the polymeric structure. Nafion possesses great mechanical properties and chemical inertness and shows good ionic electrical conductivity. To ensure this, Nafion has to be hydrated to serve as a proton conductor. The water molecules allow the dissociation of the sulphonic acid, releasing protons that can move via the Grotthus mechanism, a mechanism in which protons are transported by hydrogen bond-mediated rearrangement of water molecules and hydronium ions, ensuring the characteristic high proton conductivity in aqueous solutions[12,13,15]. Besides the Grotthus mechanism, the structure of Nafion guarantees high ionic electrical conductivity (cation transport number tends to 1) since the counterion is chemically linked to the polymeric backbone. For these unique properties, Nafion is largely used in the construction of proton membrane fuel cells.

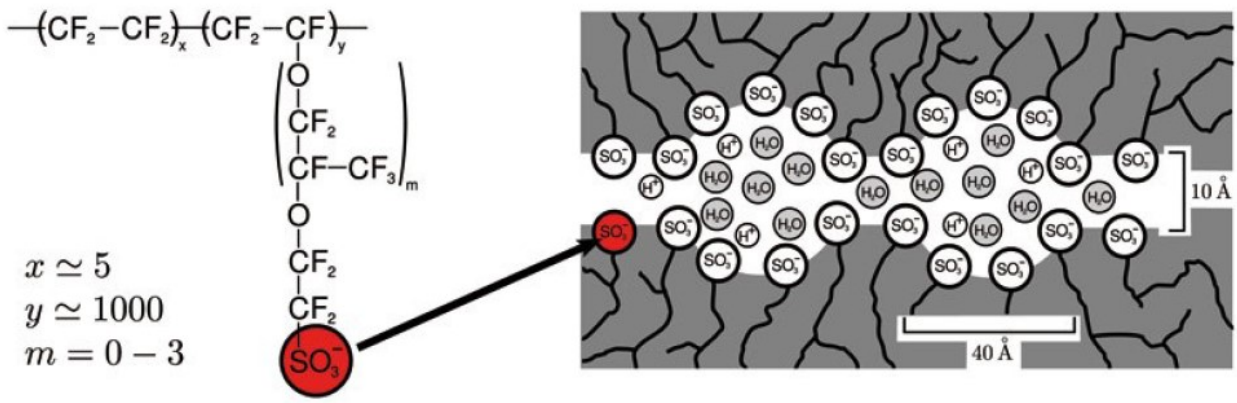

Figure 2.5*: Schematic representation of Nafion structure where the polymeric structure of this chemical can be appreciated. Water provides the environment to ensure good protonic conductivity following the Grotthus mechanism. Reprinted from (13).*

2.8 Deposition Techniques

To load the catalyst on the inert working electrode a plethora of techniques can be utilized, but one should not forget that the choice of deposition technique depends on many factors such as the type of material and its physicochemical properties, as well as the characteristics of the substrate (roughness, adherence, temperature sensitivity), the desired properties of the material (like thickness and purity of a film) and also a time factor. Therefore, choosing the right deposition technique is a crucial aspect of preserving the properties of a material[16].

In this project, the ink was loaded on the glassy carbon electrode's surface via Drop Casting. This is a simple and fast deposition technique that allows no waste of material and consists of the withdrawal of a fixed amount of a solution with a micropipette, to then dropping it on the substrate allowing evaporation of the solvent. The solvent evaporation can be a key parameter given that the substrate's temperature and the eventual use of an inert gas flow influence the final state of the film. Despite being one of the most widespread deposition techniques, this process presents some major drawbacks. The sample uniformity can be heavily influenced by the user's dexterity and is limited in the amount of the material that can be dropped and the deposition area, making it the nonoptimal technique when dealing with larger substrates. In Figure 2.6 a schematic representation of a typical drop casting process is depicted.

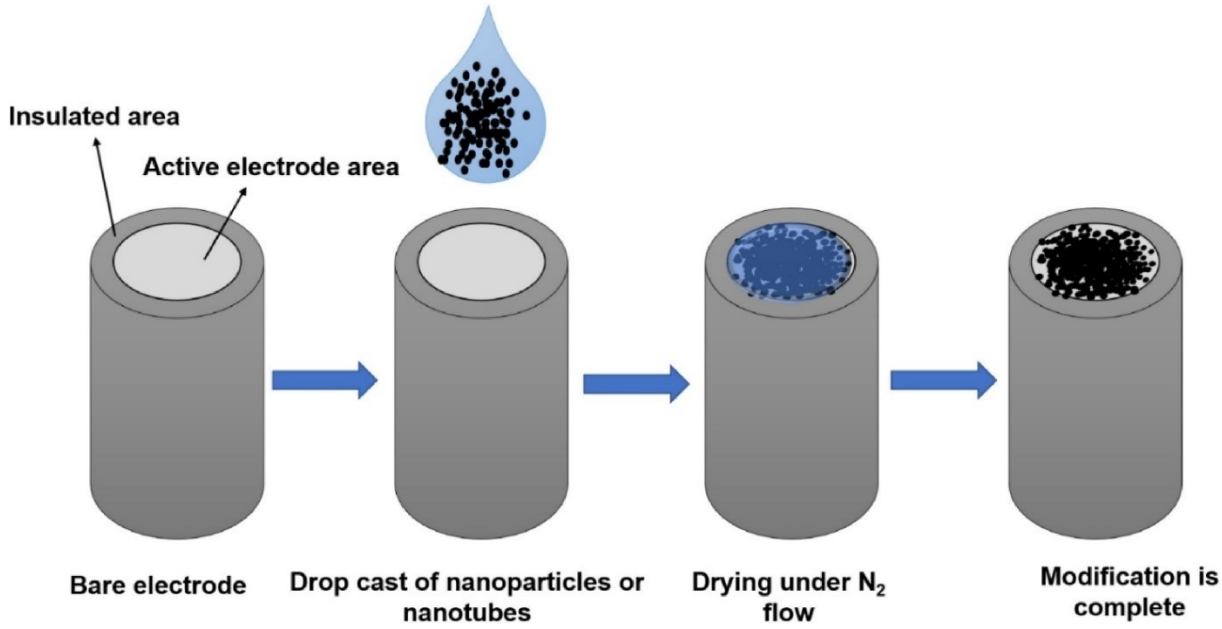

***Figure 2.6**: Schematic representation of a drop-casting process: the polished electrode's surface is covered with the ink loaded with the help of a micropipette. Then, the drying process can be carried out either with the help of an inert gas flow or left to air dry. The ink should homogeneously cover all the electrode's active surface to ensure the correct electric and catalytic behavior. Reprinted from (16)*

The electrochemistry principles and most common techniques have been discussed along with the basic knowledge needed to perform a good-quality analysis of electrochemical data; parameters such as ECSA, and Tafel slope have been described and their importance is now understood. Also, an introduction to other important aspects like the quality of ink and the deposition techniques to prepare a good and performing electrode to be used in electrochemical experiments. These concepts were used as guidelines during the experimental procedures to ensure a methodical and correct approach to perform and study the electrochemical ammonia oxidation reaction.

Bibliography

1. Bard, A.J., Faulkner, L.R. *Electrochemical Methods: Fundamentals and Applications.* 3rd edn. (2022).
2. Elgrishi, N., Rountree, K.J., McCarthy, B.D., Rountree, E.S., Eisenhart, T.T. & Dempsey, J.L. A practical beginner's guide to cyclic voltammetry. *J. Chem. Educ.* **95**, 197–206 (2018).
3. Inzelt, G. Chronoamperometry, Chronocoulometry, and Chronopotentiometry. In *Encyclopedia of Applied Electrochemistry* (Springer, 2014).
4. Li, D., Lin, C., Batchelor-McAuley, C., Chen, L. & Compton, R.G. Tafel analysis in practice. *J. Electroanal. Chem.* **826**, 117–124 (2018).
5. Petrii, O.A., Nazmutdinov, R.R., Bronshtein, M.D. & Tsirlina, G.A. Life of the Tafel equation: current understanding and prospects for the second century. *Electrochim. Acta* **52**, 3493–3504 (2007).
6. Anantharaj, S. & Noda, S. How properly are we interpreting the Tafel lines in energy conversion electrocatalysis? *Mater. Today Energy* **29**, 101123 (2022).
7. Ferriday, T.B., Middleton, P.H. & Kolhe, M.L. Review of the hydrogen evolution reaction—a basic approach. *Energies* **14**, 8535 (2021).
8. Morales, D.M. & Risch, M. On the mechanism of the oxygen evolution reaction: a perspective. *J. Phys. Energy* **3**, 034013 (2021).
9. Plevová, M., Hnát, J. & Bouzek, K. Electrocatalysts for the oxygen evolution reaction in alkaline and neutral media. A comparative review. Journal of Power Sources 507, 230072 (2021).
10. Antipin, D. & Risch, M. Calculation of the Tafel slope and reaction order of the oxygen evolution reaction between pH 12 and pH 14 for the adsorbate mechanism. *Electrochem. Sci. Adv.* **3**, e2100213 (2023).
11. Martínez-Hincapié, R., Wegner, J., Anwar, M.U., Raza-Khan, A., Franzka, S., Kleszczynski, S. & Čolić, V. The determination of the electrochemically active surface area and its effects on the electrocatalytic properties of structured nickel electrodes produced by additive manufacturing. *Electrochim. Acta* **476**, 143663 (2024)
12. Grotthuss, C.J.T. Sur la décomposition de l'eau et des corps qu'elle tient en dissolution à l'aide de l'électricité galvanique. *Ann. Chim.* **58**, 54–74 (1806).
13. Kumsa, D.O., Bhadra, N., Hudak, E.M., Kelley, S.C., Untereker, D.F. & Mortimer, J.T. Electron transfer processes occurring on platinum neural stimulating electrodes: a tutorial on the i(Ve)i(V_e)i(Ve) profile. *J. Neural Eng.* **13**, 052001 (2016).

14. Xu, K. Diffusionless charge transfer. *Nat. Energy* **4**, 93–94 (2019).
15. Grot, W. Fluorinated ionomers: history, properties, and applications. In *Introduction to Fluoropolymers*, (ed. Ebnesajjad, S.), 277–291 (William Andrew Publishing, 2013).
16. Selva Kumar, A.K., Zhang, Y., Li, D. & Compton, R.G. A mini-review: How reliable is the drop casting technique? *Electrochem. Commun.* **121**, 106867 (2020)

CHAPTER 3

3.1 Solvothermal synthesis

Solvothermal synthesis is one of the most widespread, eco-friendly, and cost-effective procedures used in chemistry to obtain a variety of materials such as metal oxides, hydroxides, and halides[1]. A typical solvothermal synthesis requires the introduction of the precursor in an inert sealable Teflon container inserted in a stainless-steel autoclave. As a result of the increasing pressure and temperature inside the autoclave, which can go way beyond the boiling point of the solvent, the solubility and reactivity significantly increase leading to a dissolution and recrystallization process that favors the production of otherwise unstable products and even unstable morphologies as compared with other conventional synthesis methods[1]. Controlling the pH, the temperature, the solvent nature, the precursor concentration, the presence of any capping agents or additives, and the reaction time is a key point to promote nuclei growth and subsequent crystallization and obtain the desired particle size and morphology.

Solvothermal synthesis is analogous to hydrothermal synthesis, as they both use a Teflon liner inserted in a stainless-steel autoclave. The only difference between the two is the different nature of the precursor's solution: in a hydrothermal process the solution is aqueous whereas in a solvothermal synthesis, the solution is a non-aqueous compound with examples including ammonia, dimethylformamide (DMF), and various alcohols. A typical solvothermal reactor is depicted in Figure 3.1.

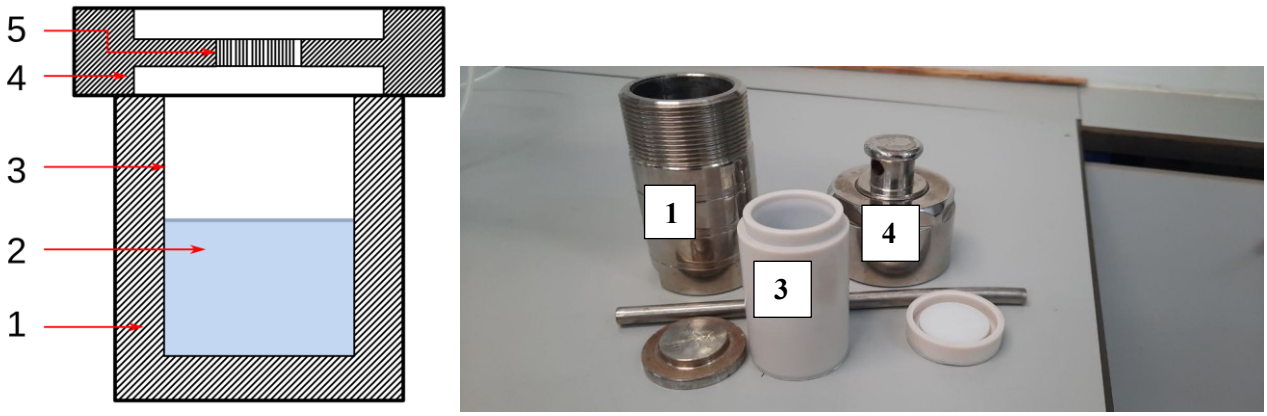

Figure 3.1*: (1) stainless steel autoclave (2) precursor solution (3) Teflon liner (4) stainless steel lid (5) spring (left). Actual solvothermal reactor used for the synthesis of Ni-based materials. Reprinted from (1). Stainless steel autoclave (1) Teflon liner (25-50 mL) (3) stainless steel lid (4) (right).*

After a brief discussion of the theory behind the solvothermal synthesis used to prepare the materials characterized during the internship, an explanation of the basic principles of the physicochemical characterization techniques employed will be given.

3.2 X-Ray Diffraction (XRD)

Since their discovery, X-rays have proven to be a powerful tool for scientists to explore new concepts and push the boundaries of science experiments. Soon enough, scientists like Ewald, Laue, and Bragg realized that X-rays could be employed to explore the crystalline structure of materials. X-rays fall deep into the electromagnetic spectrum, with a characteristic wavelength in the range between 10^{-8} and 10^{-12} nm (from so-called "soft" to "hard" X-rays) and are therefore able to interact with atoms in a crystal lattice, whose spacing is in the order of Å (10^{-10} nm) and whose placing obey the symmetry rules dictated by the crystal system they belong to[(2)].

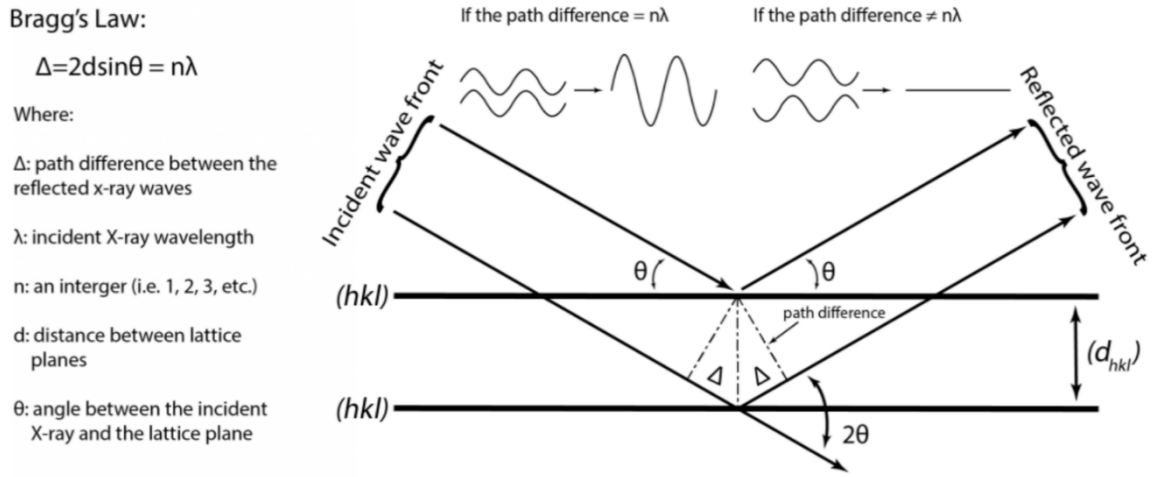

Figure 3.2*: Schematic representation of a crystal diffraction experiment and the Bragg law of diffraction. The picture shows the conditions that satisfy Bragg's law when interacting with crystal planes. Pecharsky, V. K., & Zavalij, P. Y. (2003). Reprinted from (2).*

This allows scientists to retrieve information about the crystalline structure of a material. Bragg's law of diffraction dictates the behavior of the interaction between the incident wave and the crystal lattice as stated:

$$\boldsymbol{2dsin(\theta) = n\lambda} \qquad \boldsymbol{(3.1)}$$

where ‘d’, represents the distance between two atomic planes, θ the angle of diffraction or Bragg's angle, ‘n’ is an integer number representing the diffraction order, and ‘λ’ is the incident wave wavelength[2,3].

In an X-ray diffraction (XRD) experiment, a sample composed of the material to analyze interacts with incident X-rays to produce a diffractogram. This technique is a common (usually non-destructive) characterization technique that allows identification of the crystal structure and often the composition of a sample in a solid or powder form. The monochromatic X-rays are generated via the thermionic effect, this is a phenomenon involving the heating of a tungsten metal wire to release electrons that are accelerated thanks to a potential difference toward a target anode composed of materials such as Cu, Co, and Mo; the incident electron loses its energy due to the electric field of the target’s nucleus releasing energy in the form of X-ray radiation, known as ‘Bremsstrahlung’ which has to be ultimately filtered out to avoid covering the characteristic radiation of the target.

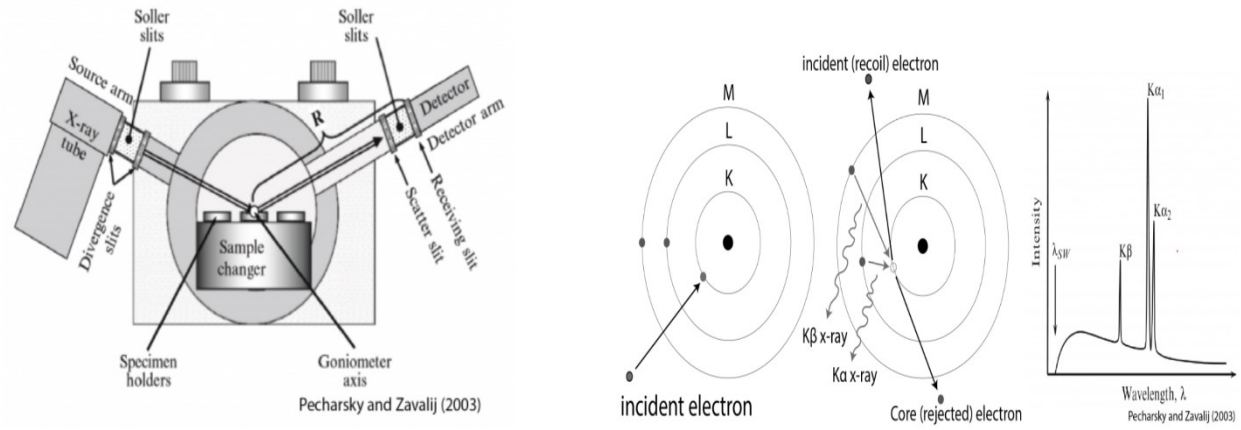

Figure 3.3*: Schematic representation of an XRD experiment geometry (left) and X-ray emission processes (right). Reprinted from (2).*

Upon impact, a dislocated electron leaves a vacancy in the innermost shells which is immediately filled by a higher shell electron, releasing excess energy as characteristic monochromatic X-ray radiation. This is focused with the help of specific optical components to reflect off the sample. Multiples focusing geometry are allowed as the X-ray tube and the detector are attached to a goniometer allowing full screening throughout a 2θ angle range, the most common of which being the Bragg-Brentano (BB) or θ:2θ geometry, where the incident angle ‘ω’ between X-ray source and the sample is always 1/2 of the detector angle 2θ. Suppose Bragg’s law of diffraction is satisfied upon reflection off the sample’s crystallographic planes. In that case, constructive interference will occur, and the detector records the peak position and intensity which is then displayed on a diffractogram. The mathematical condition to be satisfied is therefore that the path difference is an integer multiple

of the wavelength (nλ). Otherwise, destructive interference will occur producing no intensity in the recorded diffractogram, specifically in the condition when the path difference is a half-integer multiple of the wavelength.

Wave mechanics describes the behavior of any electromagnetic radiation, according to that, when two waves overlap constructive interference can occur when the overlapping waves possess the same phase producing a greater amplitude than each wave, or destructive interference can occur when the waves possess opposite phases resulting in lesser amplitude. The diffraction pattern is determined by the arrangement and spacing of atomic planes in the crystal. Different sets of planes will diffract the X-rays at different angles, and particularly the smaller the spacing between planes, the higher the diffraction angle. When registered, the diffractogram is analyzed with the help of international crystallographic databases to retrieve the structure, that is the crystalline group to which it belongs and carry a phase identification if needed. For this project, the XRD equipment used is a PANalytical Empyrean X-Rays Diffractometer as Figure 3.4 shows, and in particular, Cu K-α (1.54 Å) radiation was utilized as incident wavelength.

***Figure 3.4**: PANalytical Empyrean XRD Diffractometer SEGAI Labs at ULL used for the XRD characterization of the samples. The radiation used for the experiment was the Cu K-α (1.54 Å) wavelength.*

Scherrer formula estimates the average size of the crystallites in the direction perpendicular to the crystallographic planes causing the diffraction. A crystallite is a domain of solid-state matter that has the same structure and crystallographic orientation and ultimately is regarded as a structural parameter[3,4]. For a single crystal, the diffraction peaks will appear sharp and narrow. However, for polycrystalline samples containing small crystallites, the diffraction peaks broaden[3,4]. This is directly

related to the size of the crystallites, as smaller crystallites cause more significant broadening due to fewer atomic planes contributing to the coherent scattering. The formula mathematically states the following relation:

$$D = \frac{\lambda\beta}{L\,cos(\theta)} \tag{3.2}$$

where 'λ' is the wavelength of the X-ray; 'β' is the full width at half maximum (FWHM), the width of the diffraction peak selected for the analysis; 'θ' is the diffraction angle (Bragg's angle); and 'k', an adimensional constant also known as 'shape factor' with a value between 0.95-0.98[4]. For this project, the XRD equipment used is a PANalytical Empyrean X-Rays diffractometer as Figure 3.4 shows, and in particular, Cu K-α (1.54 Å) radiation was utilized as incident wavelength. Moving on, electron microscopy was employed to gain insight into the samples' morphology, dimensions, and elemental composition.

3.3 Scanning Electron Microscope (SEM) & Energy dispersive X-ray analysis (EDX)

Scanning Electron Microscope (SEM) is a characterization technique used to obtain information about the morphology, texture, and size distribution of a sample. Also, an elemental distribution map is accessible when coupled with an energy dispersive X-rays analysis (SEM-EDX). Based on the same constituting principle as an optical microscope, a SEM focuses an electron beam rather than photons to magnify. The electron beam is usually obtained from a so-called electron gun through the thermionic effect (the same phenomenon described for XRD) and accelerated thanks to a proper potential difference. The electron beam passes through electromagnetic lenses, usually solenoids, that are used to adjust the focus on the sample. The sample is usually placed on a plate that serves as a sample holder. Finally, the detector is made up of several detectors able to differentiate the secondary electrons, backscattered electrons, and diffracted backscattered electrons; these are two forms of electrons used in imaging, the first ones arise from the sample as a result of inelastic scattering between the atoms of the sample and the incident electron beam, while the latter ones are reflected electrons as the result of elastic scattering process.

A correlation between the atomic number and the brightness of backscattered electrons exists, allowing elemental identification, while with secondary electrons greater surface details can be reached[5]. The functioning of the detectors highly depends on parameters such as the voltage speed

and the materials' density and composition. The resolution of modern SEMs can fall somewhere between less than 1 and 20 nanometers[5].

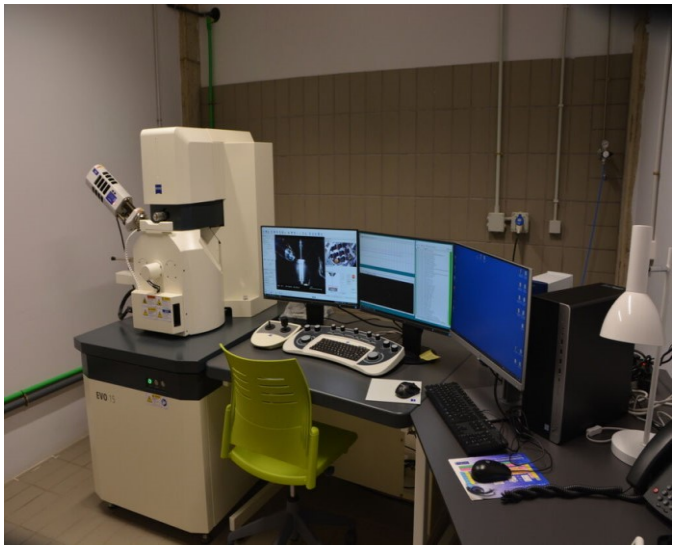

***Figure 3.5**: SEM\EDS at SEGAI Laboratories at University of La Laguna used for samples characterization.*

Coupling SEM with energy-dispersive X-ray (EDX) analysis allows a more accurate and complete analysis of a sample, allowing additional information about the chemical composition to be retrieved, including what elements are present and their distribution and concentration. EDX exploits the uniqueness of X-ray energies of a specific element to produce mapping and line scans and identify each element present in the sample[6]. When the incident electron beam hits the sample, given that the energy is sufficient, it can expel an electron from the innermost shell leaving a vacancy behind. This vacancy will be filled by an outer layer electron emitting a unique X-ray radiation in the process, with a unique wavelength unique to the element composing the material. This is the reason this technique is extensively utilized for both qualitative and quantitative non-destructive analysis, enabling users to identify both the type of elements that are present as well as the percentage of each element's concentration within the sample. Figure 3.5 shows the SEM instrument available at SEGAI Laboratories of the University of La Laguna that was used to characterize the synthesized materials.

3.4 Transmission Electron Microscopy (TEM)

Transmission Electron Microscopy (TEM) is a powerful technique providing information about the crystal structure and orientation, defects, dislocations, grain boundaries, nanoparticle size, and shape of the sample under analysis, as well as the chemical composition when coupled with complementary techniques such as Energy-Dispersive X-ray Spectroscopy (EDS)[7]. TEM analysis, therefore, is more

powerful when compared to the similar characterization technique known as SEM, which can only reveal a sample's morphology; however a fundamental prerequisite and sometimes a possible limitation for this analysis is the need for a conductive sample. The analysis is carried out by focusing a beam of electrons, accelerated through a high voltage (typically between 100 to 300 kV), and directed onto the thin conductive sample. As the electrons pass through the sample, the interaction with atoms causes various scattering phenomena, producing contrast and carrying information about the internal structure of the material, which is magnified and projected onto a detector to form an image. The working principle and components of the instrument are similar to the SEM described above. The electron beam is produced usually with a thermionic effect and is accelerated by applying a proper electrical potential (100-300 kV), giving the electron beam a wavelength much smaller than visible light, allowing for much higher resolution imaging. Again, the lenses are a series of electromagnetic ones (condenser, objective, and projector lenses) to focus and direct the electron beam, and the detector is usually an electron-multiplying detector used to amplify the signal[7,8].

Finally, the electron beam interacts with the atom of the sample resulting in elastic (no energy transfer occurs between electron and atoms in the sample) or inelastic scattering (energy from the electron beam is transferred to the atoms of the sample). In particular, one can exploit these phenomena to perform the analysis: looking at the transmission electrons (those electrons that pass through the sample without any interaction), the electrons scattered by the atomic nuclei or electron clouds without energy loss (elastic scattering) contributing to contrast in the image, or those electrons losing energy as they interact with atoms producing additional signals, such as X-rays or secondary electrons, which can provide chemical information (inelastic scattering). Image formation depends on which electrons are observed. Different operating regimes are possible such as dark field, which is when only the scattered electrons are used to form the image, allowing specific details (such as crystal defects or inclusions) to be highlighted; or bright field, in which unscattered electrons are used to form the image, and thicker or denser regions of the sample will scatter more electrons, appearing darker in the image.

TEM can reach extremely high resolution owing to the incredibly short wavelength that the electrons in the beam possess; the resolution range depends on the specific instrument and the accelerating voltage used, but generally, for conventional TEM the limit is around 0.1-1 nm, while for High-Resolution TEM (HR-TEM) one can go as low as 0.05 nm, enabling the visualization of individual atoms[7,8].

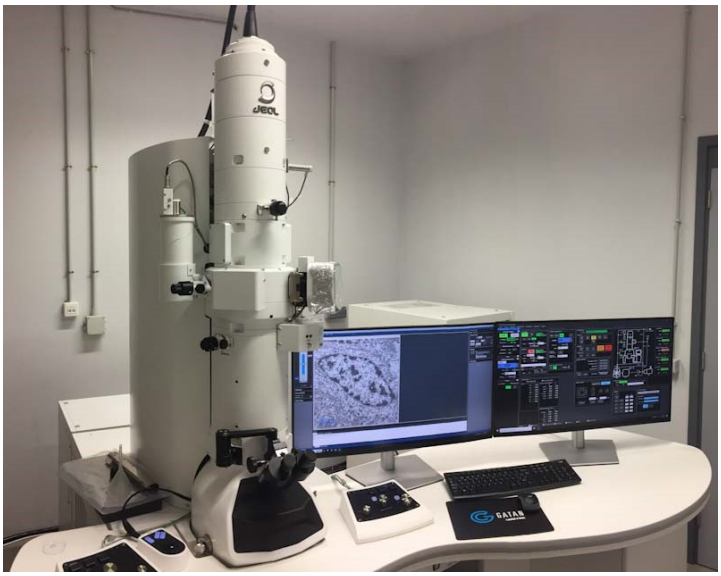

Figure 3.6*: TEM at SEGAI Laboratories at University of La Laguna used for samples characterization.*

Sample preparation is relatively straightforward, requiring only the suspension of the powdered sample in a solvent, typically an alcohol such as isopropanol (IPA). The solution is then deposited onto the sample holder, the solvent is allowed to evaporate, and the measurement is ready to start. Figure 3.6 shows the TEM instrument available at SEGAI Laboratories of the University of La Laguna that was used to characterize the synthesized materials. Inductively coupled plasma mass spectrometry was employed to obtain accurate information about the bulk elemental composition of our samples.

3.5 Inductively Coupled Plasma Mass Spectrometry (ICP-MS)

Inductively Coupled Plasma Mass Spectrometry (ICP-MS) is a common elemental analysis technique employed for its great versatility and sensibility, as this technique can potentially measure almost every element in all forms, except for elements such as Hydrogen, Helium, Argon, Nitrogen, Oxygen, Fluoride, and Neon with a detection limit as low as 0.1 part per trillion (ppt)[(9)]. ICP-MS operates by exploiting Argon plasma to ionize the samples; these ionized species are then channeled thanks to the vacuum system into the quadrupole mass filter and ultimately into the detector. In a typical ICP-MS instrument, the following components are present, and a brief description of their use is given[(9,10,11)]:

- A sample introduction system. These are usually in a liquid form and with the help of a nebulizer an aerosol is produced and transported along with Argon gas to reach the plasma.

- The induced coupled plasma is generated with the ionization of the Argon gas. The energy necessary for sparking the plasma is usually provided by a radio frequency (RF) generator; this energy is transferred to the Argon gas flow by inductive coupling from a load coil wrapped around the outside of a quartz tube. The RF causes the oscillation and consequent collision of free electrons with Argon atoms, eventually ionizing them and producing plasma. Because of the plasma, extremely high temperatures, as high as 10,000 °C, are reached.
- A vacuum interface is necessary to separate the quadrupole from the extremely hot plasma and to allow the transportation of the ionized samples to the detector. Metallic parts specifically designed for vacuum and plasma technologies are exploited.
- Ion focusing lenses are exploited to deflect and channel the ionized species. These lenses consist of multiple vacuum and plasma-resistant metallic plates to which a variable electrical potential is applied.
- Collision and reaction cells are used to improve the accuracy and precision of measurements by reducing spectral interferences, as many species could have similar m/z ratio.
- A quadrupole mass spectrometer to filter ions by their charge-to-mass ratio (*m/z*) to yield the mass spectrum. The quadrupole's magnets are usually metallic rods to which an RF frequency and variable DC current are applied to create an adequate magnetic field and sort out the ionic species.
- An electron-multiplying detector that receives the selected ions which strike the surface of the detector, releasing electrons. These are then amplified through a cascade process where secondary electrons are generated in multiple stages, leading to a significant increase in the signal.

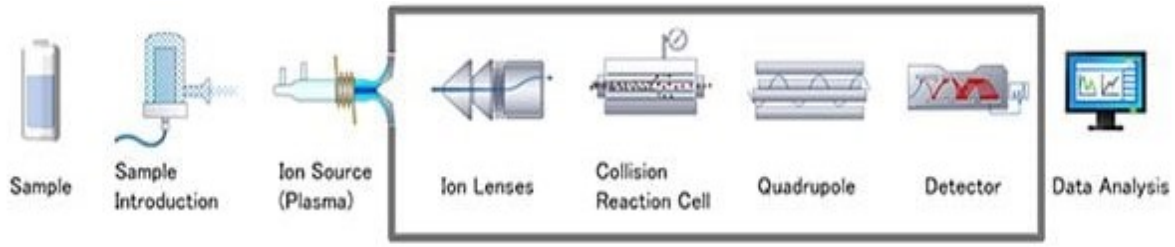

Figure 3.7*: Schematic representation of the principal components of a common ICP-MS instrument[8]. These include the sample introduction nozzle to produce the aerosol that will reach plasma, generated by an ion source. Ion lenses are used to channel the ionized species toward the collision and reaction cell that produces a more accurate signal, ultimately reaching the quadrupole for ion separation on the base of the m/z ratio before reaching the detector. Reprinted from (8).*

The last physicochemical characterization technique exploited again X-ray properties to access surface stoichiometry and the chemical state of the element present on the surface.

3.6 X-ray Photoelectron Spectroscopy (XPS)

X-ray Photoelectron Spectroscopy (XPS) is a surface-sensitive characterization technique, in which X-rays strike a material's surface and the emitted photoelectron's kinetic energy is registered. This analytical technique allows the surface composition investigation, particularly to access the chemical state of the elements in the sample, and to determine surface elemental stoichiometry[12]. When an X-ray hitting the sample surface successfully transfers its kinetic energy to a core-level electron, this can leave the nucleus, and its kinetic energy is registered. The mathematical expression states that the binding energy (B.E.), that is how strong the electron is bound to the nucleus, is equal to the energy of the incident photon (hν), the kinetic energy of the emitted electron (K.E.), and the Fermi level (ϕ_{Fermi}) of the sample[12]:

$$B.E.(eV) = h\nu - K.E. + \phi_{sample} \tag{3.3}$$

An emitted photoelectron leaves a core hole behind that can be filled by a valence orbital electron, this relaxation process results in the emission of a photon of energy (hν'), a process known as X-ray fluorescence. A second competitive process is Auger emission: the energy is transferred to another electron, typically an outer shell electron, which is then ejected from the atom. The kinetic energy of the Auger electron is independent of the incident X-ray energy and is determined solely by the energy levels of the atom itself. These electrons, when detected, appear as distinct peaks at specific energies, characteristic of the element, and they provide additional information about the electronic structure and can be used to complement photoelectron peaks for elemental and chemical analysis.

The main components of an XPS instrumentation will be briefly described. Starting from the X-ray source, the most employed ones are Al (1486.6 eV) or Mg (1253.6 eV), and the decision of one or the other will affect the transitions that can be observed, the spectral resolution that can be achieved, and the depth of analysis. XPS is usually considered an ultra-high vacuum (UHV) technique, therefore it is carried out inside a vacuum chamber necessary to maintain the sample in a clean, contaminant-free environment and to ensure that the photoelectrons travel unimpeded from the sample to the detector, operating at pressures around 10^{-9}-10^{-10} mbar, which minimizes the scattering of electrons by gas molecules[12,13]. A sample stage holds and positions the sample during analysis, allowing for manipulation such as rotation, tilting, or translation, and in some cases, it is also possible to heat the sample holder to study temperature effects on the materials under investigation. The introduction of the sample is a step mechanism, passing through multiple locks and barriers to avoid compromising the vacuum level inside the main chamber. Inside this, another important instrumentation is present, that is a so-called flood gun, used to compensate for any positive charge

buildup on the sample surface by supplying additional low-energy electrons or ions, stabilizing the charge. Connected to the vacuum chamber, usually placed above the sample holder the analyzer is found; The most common type is the hemispherical electron analyzer consisting of two curved, electrically charged hemispheres. A voltage is applied to the hemisphere, with the outer side usually held at negative potential concerning the inner side. The electrons enter the analyzer through a slit, and only electrons with a specific energy will be able to travel through the analyzer. Those with higher energies will crash on the outer hemisphere walls, while lower energies electrons will collide with the inner wall. The voltage can be varied to allow a range of acceptable energies for the incoming electrons. Finally, the detector counts and records the photoelectrons that pass through the electron analyzer; the most common are the 'channeltron' or a 'multichannel plate' detector[13]. The working principle of these detectors is straightforward, so when a photoelectron hits the detector, it generates a cascade of secondary electrons that are amplified, producing a measurable signal proportional to the number of photoelectrons at a given energy.

The whole XPS signal is conventionally called 'Survey' showing a counting versus the binding energy of the corresponding emitted photoelectrons, Auger electrons, and secondary electrons, responsible for the increasing background at higher binding energies. The survey includes all the signals corresponding to the elements of the sample (and also impurities like Carbon (C 1s), almost always present as a contaminant) however, the single isolated peaks can be individually scanned numerous times (that is the number of sweep, an important parameter necessary for area normalization) and analyzed to allow the deconvolution of the signal to identify the chemical state of the element producing that peak at that specific binding energy.

To calculate the surface stoichiometry, several parameters are needed such as 'α' and 'β' which are parameters derived by the photoionization cross-section (σ), that is the probability that an atom will absorb the incident X-ray and emit a photoelectron from a specific core level; these are tabulated and widely accessible in the literature and in many XPS opensource software. Another parameter is the inelastic mean free path (IMFP) of a photoelectron, later called λ (Å), and it is defined as the average of distances, measured along the trajectories, that particles with a given energy travel between inelastic collisions in a substance[14]. It depends strongly on the kinetic energy of the photoelectrons and is influenced by inelastic scattering processes within the material; this makes the value of the IMFP strongly dependent on the matrix of the material and is calculated with the help of QUASES IMFP software that allows retrieving the value for different elements inside a specific matrix.

Finally, once the total area under the peak is known, it can be divided this value by the number of sweeps, that is the number of times that peak has been detected, to calculate the sensitivity factor

(S.F.), which is essential for accurately quantifying surface elemental composition, as it corrects for differences in photoelectron emission probabilities across different elements, allowing for the calculation of relative atomic concentrations on the surface. The atomic concentration of an element (C_i) can be determined from its photoelectron peak intensity (I_i) normalized by the number of sweeps and the corresponding sensitivity factor (S_i) using the following formula[15]:

$$C_i = \frac{\frac{I_i}{S_i}}{\Sigma_j \frac{I_j}{S_j}} \tag{3.4}$$

So far, an introduction to the principle of the synthetic procedure and materials characterization has been given; this concluded the plethora of physicochemical characterization techniques employed to understand the fundamental properties of the synthesized materials during the internship. In the next paragraph, the last characterization technique used during the experimental period will be described, that being the in-situ electrochemical characterization technique that allows a deeper understanding of the electrochemical processes involved.

3.7 Differential Electrochemical Mass Spectrometer (DEMS)

Herein, the theoretical principles behind Differential Electrochemical Mass Spectroscopy (DEMS) will be briefly discussed, whereas the description of the cell and the experimental parameters will be explained in the Experimental Section. DEMS is a powerful in-situ electrochemical characterization technique that couples a mass spectrometer with an electrochemical cell to allow the analysis of gaseous and volatile products. It can deliver potential-, time-, mass-resolved signals which facilitate the understanding of reaction kinetics, and this allows one to obtain accurate information about the reaction under investigation as it bypasses the typical limitations of conventional electrochemistry[16,17].

Electrochemistry is often referred to as a blind characterization technique, meaning that one can only observe that a redox reaction is occurring inside a specific potential window, within predetermined experimental conditions such as electrolyte composition, temperature, pH, pressure, and so forth, but no information about the final products of the reaction is given. Therefore, most of the time one can assume within an agreeable range that the reaction is proceeding in the desired direction. DEMS allows access to accurate information about the formed products, as it precisely links the electrochemical response with a mass spectrometer signal, ensuring that the signal the user is observing is due to the presence of a specific species at that applied potential. A mass spectrometer is

an instrument that allows to identify chemical species, translating their mass to charge ratio (m/z) into an ionic current. A vacuum system connected to the mass spectrometer allows the capture of volatile or gaseous species in an inlet, and there, gases are ionized and separated, typically using a quadrupole on the base of their m/z ratio. Then, a detector measures an ion current, that is a measure of the partial pressure of the respective gas component or of fragments of the same mass generated in the ion source[11,19].

An example of a DEMS signal is reported in Figure 3.8: the blue line in the bottom part corresponds to the electrochemical response, that is the Faradaic current, while the red curve on top is the m/z for the OER. From this, one can accurately link the formation of O_2 molecules as the reaction products at an exact faradaic potential. From this, it is possible to understand the precious qualitative analysis offered by DEMS, allowing to retrieve deeper information on those processes with different reaction pathways and selectivity limitations, helping in the identification of the numerous amounts of different species. The registered signal of a selected species is unequivocally due to the presence of that species at that specific applied potential. This has tremendous implications, especially because it can accurately detect the onset potential of a redox reaction. A quantitative analysis is also accessible when using DEMS if proper calibration technique using chemical standards is carried out.

When the reaction of interest takes place in the cell, the gaseous products formed on the electrode's surface flow through a hydrophobic membrane placed in very close contact with the electrode's surface and are driven by the vacuum system composed of the vacuum pumps directly to a mass spectrometer. A first vacuum chamber connected to a rotary pump is responsible for preliminary vacuum; pressions of around 10^{-6} mbar are reached by purging the gas present in the chamber before connecting to the ionization chamber. Here, a turbomolecular pump allows higher vacuum levels to be reached, as low as 10^{-8} mbar. When a reaction produces gaseous products, these pass through the membrane, and flow first through the preliminary chamber and then to the ionization chamber, where they are ionized by an incandescent filament and are subsequently analyzed by a mass spectrometer to yield a charge-to-mass ratio (m/z).

Proprietary software allows to simultaneously visualize multiple parameters such as the applied potential, ionic current, and the pressure of the chamber. In this way, it is possible to simultaneously correlate the ionic current produced by the mass spectrometer and the faradaic current registered with the potentiostat during an electrochemical measurement with great accuracy. The sweep speed at which the cyclic voltammetry can be performed influences the instrument's responsiveness. The usual sweep speed is in the range of 0.5-2 mV/s, because it is important to allow enough time for the volatile products to pass through the membrane, reach the filament be ionized, and be carried to the mass

spectrometer to yield the m/z signal before any significant electrochemical change happens due to changes in the applied potential[18].

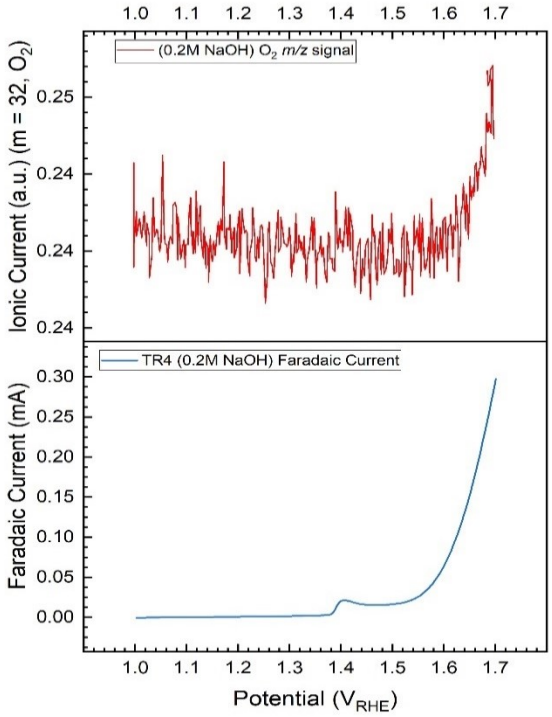

Figure 3.8: *Typical DEMS signal for an electrochemical process. The blue line represents the Faradaic current, that is the current registered by the potentiostat, while the red one corresponds to the m/z signal, in this case monitoring the O_2 mass as the OER is taking place. This technique allows accurate analysis of formed products and electrochemical parameters such as real onset potential are accessible.*

Bibliography

1. Demazeau, G. Solvothermal and hydrothermal processes: the main physico-chemical factors involved and new trends. *Res. Chem. Intermed.* **37**, 107–123 (2011).
2. Pecharsky, V. K. & Zavalij, P. Y. *Fundamentals of Powder Diffraction and Structural Characterization of Materials* (Kluwer Academic Publishers, 2003).
3. Harrington, G. F. & Santiso, J. Back-to-Basics tutorial: X-ray diffraction of thin films. *J. Electroceram.* **47**, 141–163 (2021).
4. Hassanzadeh-Tabrizi, S. A. Precise calculation of crystallite size of nanomaterials: A review. *J. Alloys Compd.* **968**, 171914 (2023).
5. ThermoFischer Scientific, Scanning Electron Microscope Working Principle, https://assets.thermofisher.com/TFS-Assets/MSD/Reference-Materials/WP0016-scanning-electron-microscopy-working-principle.pdf
6. Goldstein, J. *et al. Scanning Electron Microscopy and X-ray Microanalysis* (Springer, 2017).
7. Egerton, R. F. *Electron Energy-Loss Spectroscopy in the Electron Microscope* (Springer, 2011).
8. Williams, D. B. & Carter, C. B. *Transmission Electron Microscopy: A Textbook for Materials Science* (Springer, 2009).
9. Agilent, *An Introduction to the Fundamentals of Inductively Coupled Plasma – Mass Spectrometry (ICP-MS)*, https://www.agilent.com/en/product/atomic-spectroscopy/inductively-coupled-plasma-mass-spectrometry-icp-ms/what-is-icp-ms-icp-ms-faqs.
10. Montaser, A. *Inductively Coupled Plasma Mass Spectrometry* (Wiley-VCH, 1998).
11. Ammann, A. A. Inductively coupled plasma mass spectrometry (ICP MS): a versatile tool. *J. Mass Spectrom.* **42**, 419–427 (2007).
12. Simon, P., Baldovino-Medrano, V. G. & Wojcieszak, R. X-ray photoelectron spectroscopy (XPS): principles and application for the analysis of photoactive materials. In *Springer Handbook of Inorganic Photochemistry* (eds Bahnemann, D. & Patrocinio, A. O. T.) (Springer Handbooks, Springer, Cham, 2022).
13. Krishna, D. N. G. & Philip, J. Review on surface-characterization applications of X-ray photoelectron spectroscopy (XPS): recent developments and challenges. *Appl. Surf. Sci. Adv.* **12**, 100332 (2022).
14. Jablonski, A. & Powell, C. J. Relationships between electron inelastic mean free paths, effective attenuation lengths, and mean escape depths. *J. Electron Spectrosc. Relat. Phenom.* **100**, 137–160 (1999).
15. Shard, A. G. J. Vac. Sci. Technol. A **38**, 041201 (2020).

16. Zhao, K., Jiang, X., Wu, X., Feng, H., Wang, X., Wan, Y., Wang, Z. & Yan, N. Recent development and applications of differential electrochemical mass spectrometry in emerging energy conversion and storage solutions. *Chem. Soc. Rev.* **53**, 6917–6959 (2024).
17. Chen, W., He, F. & Chen, Y.-X. On the accurate calibration of differential electrochemical mass spectrometry. *Curr. Opin. Electrochem.* **42**, 101393 (2023).
18. Rizo, R. Catalizadores de Pt-Sn para la reacción de oxidación de etanol. PhD thesis, Universidad de La Laguna (2017).
19. Kero, F.A., Pedder, R.E. & Yost, R.A. Quadrupole mass analyzers: theoretical and practical considerations. In *Encyclopedia of Genetics, Genomics, Proteomics and Bioinformatics* (eds Jorde, L.B., Little, P.F.R., Dunn, M.J. & Subramaniam, S.) (2005).

CHAPTER 4

4.1 Synthetic Procedures

TR1 $Ni(OH)_2$ Hexagons

The TR1 $Ni(OH)_2$ nanoparticles synthesis proceeds with a facile solvothermal synthesis according to a previous work found in the literature[1]. The expected morphology corresponds to hexagonal $Ni(OH)_2$ nanoparticles. To start the synthesis, $Ni(NO_3)_2 \cdot 6H_2O$ (0.1099 g, 0.375 mmol) were dissolved into 15 mL MilliQ water. Then, 0.375 µL of triethylamine were added drop by drop to the solution under stirring. At this point, the solution was brought to volume (50 mL) with MilliQ water transferred into a Teflon container and then put in a stainless-steel autoclave and kept in an oven at 180°C for 24 hours. The material was then recovered by centrifugation at 4000 rpm for 5 minutes per washing using ethanol and MilliQ water (3 EtOH, 2 MilliQ water), before pouring it onto a Petri dish and left to dry at 60°C overnight. Finally, the recovered material was weighted, and 0.0189 g was recovered.

TR2 $Ni(OH)_2$ Spheres

To synthesize TR2 $Ni(OH)_2$ nanoparticles 1.4544 g of $Ni(NO_3)_2 \cdot 6H_2O$, 2.00 g of glycine, 2.00 g of Na_2SO_4 salt were dissolved in 25 mL of MilliQ water as indicated in literature work[2]. Later, 10 mL of NaOH (2.0803 g) solution was added dropwise into the water solution under magnetic stirring. The blue solution was then transferred into a 80 mL Teflon container and then put in a stainless-steel autoclave and kept in an oven at 180°C for 24 hours. The material was then recovered using a centrifuge at 4000 rpm for 5 minutes per washing using ethanol and MilliQ water (3 EtOH, 2 MilliQ water), before pouring it onto a Petri dish and left to dry at 60°C overnight. Finally, the recovered material was weighted, and 0.3918 g was recovered.

TR3 $Ni(OH)_2$ Flowers

The TR3 $Ni(OH)_2$ nanoparticles are synthesized in a similar manner as the TR1 sample[1]. In particular, 0.3288g of $NiSO_4 \cdot 6H_2O$ was dissolved in 25 mL of MilliQ water and subsequently, 3.75 mL of a solution of NH_3 2M was added under stirring for 20 minutes. After that time, the solution containing the precursors was added to a 20 mL Teflon container inserted in a stainless-steel autoclave and set to 180°C for 24 hours in an oven. The material was then recovered using a centrifuge at 4000 rpm for 5 minutes per washing using ethanol and MilliQ water (3 EtOH, 2 MilliQ water), before pouring it onto a Petri dish and left to dry at 60°C overnight. Finally, the recovered material was weighed, and 0.1041 g was recovered.

TR4 $Ni(OH)_2$ Hollow Cages

The synthesis of the TR4 sample involves the coordination, etching, and precipitation mechanism starting from a Cu_2O nanocages template to obtain $Ni(OH)_2$ nanoparticles as reported in literature[3]. To obtain the hollow nanocages structure that distinguishes this sample, the first step is to synthesize a Cu_2O template. For that, in an Erlenmayer flask, 0.8525g of $CuCl_2 \cdot 2H_2O$ were dissolved in 500 mL of MilliQ water. The solution was set to 55 °C for 3 minutes. Then, 50 mL of a 2M NaOH solution were added and was left stirring for 30 minutes at the same temperature. After that, 50 mL of a solution containing 5.2832g of Ascorbic Acid was added to the flask, and it was left at 55 °C and stirred for 3 hours. After this time, the material was recovered using a centrifuge, washed three times with ethanol and 2 times with MilliQ Water, and then left to dry in an oven at 60 °C. 100 mg of Cu_2O template and 40 mg of $NiCl_2 \cdot 6H_2O$ were added and dissolved in a 100 mL solution of EtOH and MilliQ Water (1:1 ratio) contained into a new Erlenmayer flask. The flask was then put under sonication for ten minutes, then 3.3 mg of Polyvinylpyrrolidone (PVP) was added. The solution was kept under stirring for 30 minutes. After that time, 40 mL of a solution containing 6.3244 g of $Na_2S_2O_3$ were added to the flask and left stirring for three hours. Finally, to recover the material, the solution was vacuum filtered, and the recovered material was left to dry in an oven overnight at 60 °C.

TR5 $Ni(OH)_2$ Cubes

ZIF-8 derived $Ni(OH)_2$ nanoparticles were synthesized starting from a ZIF-8 (Zeolitic Imidazolate Framework) precursor[4]. This was synthesized by adding 1.9709 g of 2-methylimidazole in 25 mL of methanol. To this, 1.7854 g of $Zn(NO_3)_2 \cdot 6H_2O$ dissolved in 25 mL of methanol were added and then sonicated for 20 mins. The solution was heated to 40 °C for 24h. After this time, the material was recovered using a centrifuge, washed three times with ethanol and 2 times with MilliQ water, and then left to dry in an oven at 60 °C. To synthesize the $Ni(OH)_2$ nanoparticles, 0.1707 g of ZIF-8 precursor were added into a beaker with 0.3565 g of $NiCl_2 \cdot 6H_2O$ and 15 mL of methanol. The solution was then transferred into a 50 mL Teflon container and then put in a stainless-steel autoclave and kept in an oven at 120°C for 1 hour. The material was then recovered using a centrifuge at 4000 rpm for 5 minutes per washing using ethanol and MilliQ water (3 EtOH, 2 MilliQ water), before pouring it onto a Petri dish and left to dry at 60°C overnight.

TR6 Cu_2O-$Ni(OH)_2$ Cubes

To obtain the TR6 40.6 mg of $NiCl_2 \cdot 6H_2O$ were dissolved in 50 mL of ethylene glycol, adding 100 mg of the Cu_2O template used for the TR4 preparation. After that, 40.7 mg of PVP were added to the solution and heated with a reflux at 140°C. 1.6294 mg of $NaBH_4$ were added and the solution was left at reflux for 2 hours at the same temperature; after this time, 125 mL of acetone were used to separate and isolate the formed particles that should possess a cubic morphology with an ideal monolayer of Ni particles adsorbed on the surface of the copper cubes. This sample differentiates itself from the TR4 for the bulky cubic structure, unlike the hollow cage structure of this, and the higher amount of copper as the template is not etched and precipitated.

Once the materials were synthesized and recollected, a small amount of the samples were sent to SEGAI (General Research Support Service) of the University for the physicochemical characterization. In the meantime, the conventional electrochemical characterization was carried out. The first step was the electrode preparation. An ink composition study was carried out to ensure the best dispersion on the electrode's surface.

4.2 Ink Composition Study

Before dropping the ink on top of the electrode, it is a good practice to optimize the ink, to ensure the best performance of the material. As already discussed, conductive inks are mostly formulated with three main components: the conductive material, a binder agent, and the solvent; therefore, an ink composition study was carried out to evaluate the best solvent to disperse the synthesized materials that would eventually be drop-cast on a glassy carbon electrode[(6)]. Ethanol (EtOH) and isopropyl alcohol (IPA) were chosen as solvents and to evaluate the dispersion, various inks of variable composition of these solvents were prepared. For every ink, 2 mg of catalyst was weighed and added to an Eppendorf tube with 15 μL Nafion and different ratios of alcohol and MilliQ water. Table 4.1 and Table 4.2 summarize the alcohol:MilliQ water ratio and volumes.

Figure 4.1 shows the optical microscope images of the dispersion of some of the inks prepared and deposited on the electrode's surface. From all the ink compositions studied, only the ones shown in the figure reported below were looked at under the optical microscope, whereas the other compositions were not further characterized due to the impossibility of having a correct dispersion and eventually depositing them on the electrode's surface. It is clear from these pictures that different solvents influence the result, and it is possible to see how the drying process affects the result as well. In particular, these inks were left to air-dry after the deposition and one can see how in certain cases

the material would start to peel off because of oxidative processes associated with the humidity present in the room. The best dispersion was obtained with a composition of 30% EtOH, also, this composition resulted as the easiest to deposit on the electrode's surface as a result of the good dispersion of the catalyst; therefore the final ink is prepared by weighing 2 mg of catalyst in an Eppendorf tube and pounding it with a mortar to reduce the particle size before adding 15 µL Nafion, 150 µL EtOH, 335 µL MilliQ water to obtain a total volume of 500 µL. Before every drop cast procedure, the ink was sonicated using an ultrasound machine for 30 minutes to ensure good dispersion of the catalyst. To study the AOR, 7.1 µL of the selected ink was drop cast on the glassy carbon electrode's surface using a micropipette to obtain a catalyst loading of 0.4 g/cm^2.

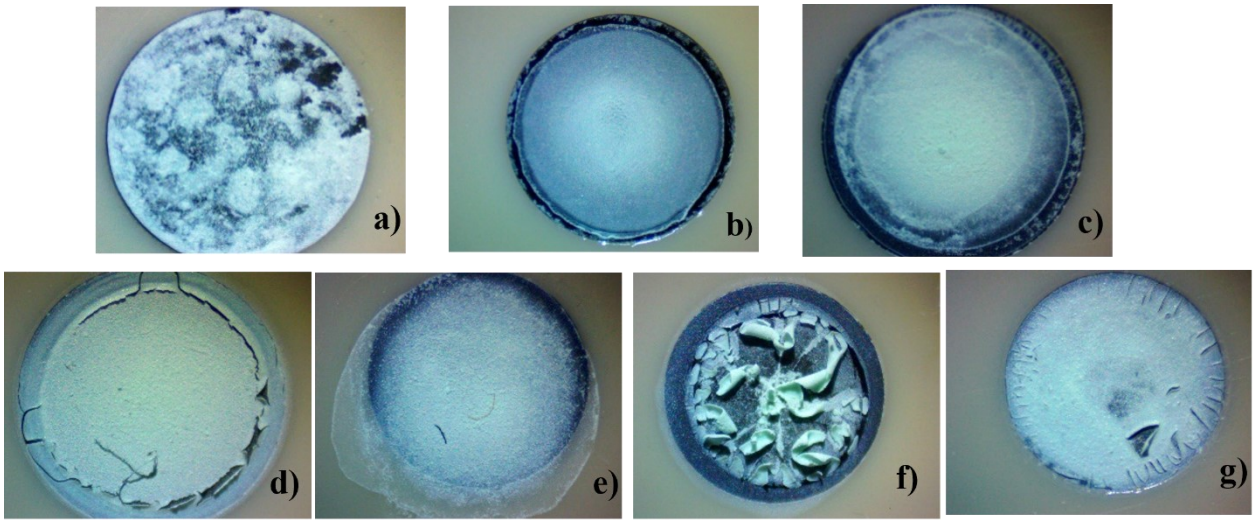

Figure 4.1*: Optical microscope images of the different ink compositions after the drop-casting and drying process. From left to right (first row): 20% EtOH(a), 30% EtOH(b), 40% EtOH(c). From left to right (bottom row): 20% IPA(d), 30% IPA(e), 40% IPA(f), 50% IPA(g). The best dispersion was obtained with the 30% EtOH (b) composition. Also, the influence of the atmospheric humidity can be appreciated by looking at the cracks or by looking at the catalyst film as it peels off the surface (f).*

The following tables summarize the ink composition for the two different solvents, providing the exact tested concentration and the values withdrawn for the Nafion, the solvent, and Milli-Q Water. Total volume is V_{total} = 500 µL.

For the sake of completeness, it is important to specify that the ink composition study and any ink prepared during the experimental procedures were dispersed with the use of an Ultrasound sonicator. This is currently one of the most common procedures for dispersing a catalyst in solution with an ionomer, obtaining in this way the ink. However, particular attention should be given to the frequency

of the ultrasound bath as this could dramatically influence the catalyst and the ionomer dispersion, as well as the time of the dispersion. For each one of the inks prepared, the ultrasound sonication was carried out for 30 minutes before any drop-casting procedure; also, since the drop-casting was performed by depositing smaller volumes multiple times (due to the small surface area of the glassy carbon electrode), ultrasound sonication was repeated during the drying process between each deposition if any noticeable inhomogeneity sign of the ink was noticed.

Table 4.1*: Ink Composition Study Summary. The table reports the composition of the ink using EtOH as a solvent. The final volume of the ink was 500 µL stored in an Eppendorf test tube.*

Ethanol %	**Final Composition (V_{total} = 500 µL)**
20%	15 µL Nafion + 100 µL EtOH + 385 µL H_2O
30%	15 µL Nafion + 150 µL EtOH + 335 µL H_2O
40%	15 µL Nafion + 200 µL EtOH + 285 µL H_2O
50%	15 µL Nafion + 250 µL EtOH + 235 µL H_2O
60%	15 µL Nafion + 300 µL EtOH + 185 µL H_2O
70%	15 µL Nafion + 350 µL EtOH + 135 µL H_2O
80%	15 µL Nafion + 400 µL EtOH + 85 µL H_2O

Table 4.2: *Ink Composition Study Summary. The table reports the composition of the ink using IPA as a solvent. The final volume of the ink was 500 µL stored in an Eppendorf test tube.*

IPA %	**Final Composition (V_{total} = 500 µL)**
20%	15 µL Nafion + 100 µL IPA + 385 µL H_2O
30%	15 µL Nafion + 150 µL IPA + 335 µL H_2O
40%	15 µL Nafion + 200 µL IPA+ 285 µL H_2O
50%	15 µL Nafion + 250 µL IPA + 235 µL H_2O

4.3 Glassy Carbon Electrode Polishing Procedure

Surface cleanliness is a critical property for every electrode and all redox systems. For that, a polishing treatment may be required[7,8]. A typical polishing treatment can be carried out with a polishing kit consisting of a fine grit polishing pad and Al_2O_3 powder (1 µm, 0.3 µm, 0.05 µm), as shown in Figure 4.2.

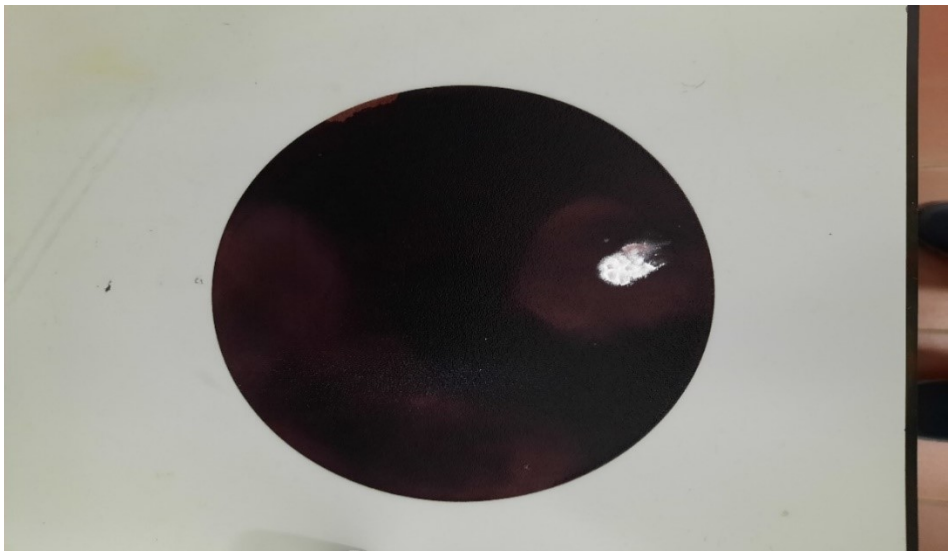

***Figure 4.2**: The polishing pad used for the polishing procedure. Alumina powder of the desired size is deposited on the corresponding area ready to be used for polishing the electrode. The polishing pad needs to be wet before every application and thoroughly washed to ensure the elimination of any alumina powder and also to prevent contamination.*

The polishing pad is divided into three zones with different grain sizes, on top of which the corresponding alumina powder will be added. As the first step, one must wet the surface of the grit with MilliQ water and then add the desired alumina powder to the corresponding grid zone. The polishing must always go from the thicker to the finer powder. After that, the electrode's surface is polished with a movement that resembles a figure eight for several minutes, to ensure a homogeneous polishing effect for all the electrode's surface; this would not be possible with a circular movement. Afterward, the electrode's surface is rinsed with water and the procedure is repeated with the finer grain size.

4.4 Drop Casting Procedure

Once the ink is well dispersed, it can be drop cast with a micropipette on the clean and polished glassy carbon electrode's surface. The electrode is a Rotating Disk Electrode (RDE) tip. A total volume of 7.1 µL is loaded on the electrode's surface by depositing 2.5 µL, 2.5 µL, and 2.1 µL and left to air dry. Figure 4.3 shows the RDE tips as the ink is drying; the drying process can be either carried out with the help of an argon flow (right image) or left to airdry (left image), the first being significantly faster. The latter is significantly slower than the first one and can expose the material to atmospheric oxygen and humidity which can alter the catalyst film on the electrode's surface. Once dry, the electrochemical cell can be assembled.

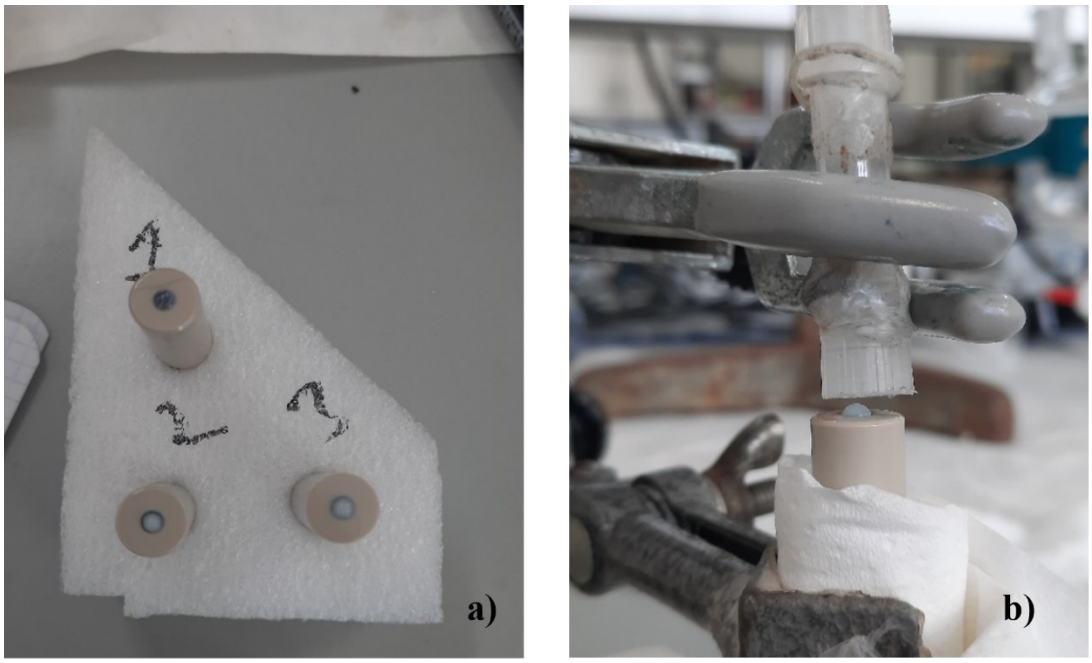

***Figure 4.3**: Rotating Disk Electrode Tips composed of a Glassy Carbon Electrode as they are left to air dry (a) after the drop-casting process to load the catalyst on the electrode's surface, and inert gas-mediated drying process (b). In this case, Argon gas was used as an inert gas.*

4.5 Electrochemical Cell Cleaning Procedure

All the glass equipment used during the electrochemical measurements was put into a $KMnO_4$ bath for 24 hours before the experiment. Afterwards, Piranha solution was used to remove the $KMnO_4$ presence, and then thoroughly washed with MilliQ water several times. This is a very effective and standard technique for removing organic species, ensuring the cleanliness and readiness of the glassware, and allowing reproducibility[7,8,9].

4.6 Electrochemical Cell Assembly

The electrochemical cell used for the electrochemical Ammonia Oxidation Reaction (AOR) is the one depicted in Figure 4.4. The glass cell is equipped with a five-hole plastic cap in which a Luggins tube containing the reference electrode (a Reversible Hydrogen Electrode RHE), a counter electrode (CE a glassy carbon rod), and the working electrode (WE) are inserted. The remaining entrance hole is closed in the case of a non-controlled environment measure, while when the cell is deoxygenated, a bubbler tube is introduced in the cell to ensure an argon flow.

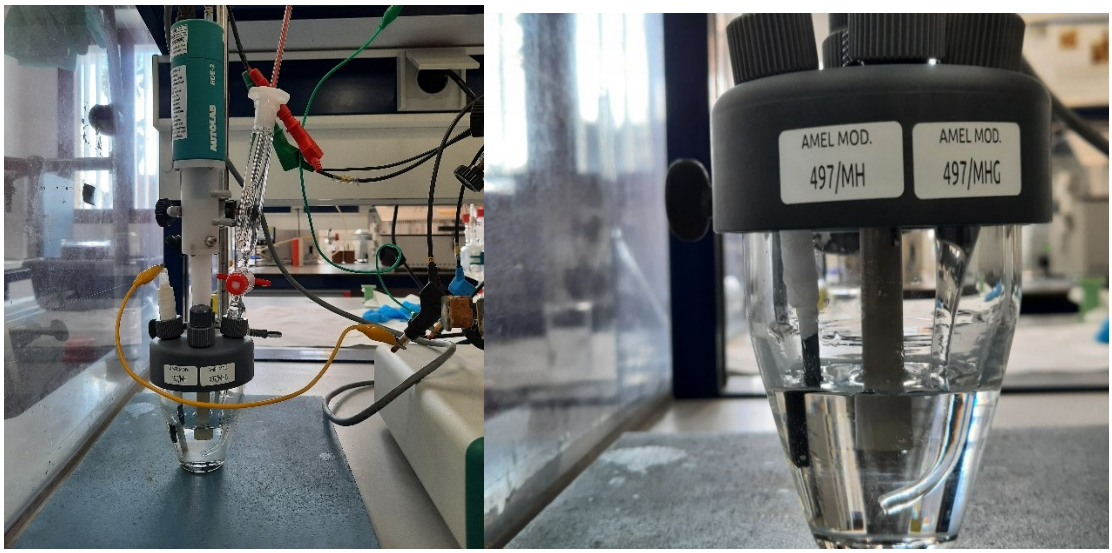

***Figure 4.4**: The image shows the cell setup ready for the electrochemical measurement (left). Connected to the yellow cable is the glassy carbon electrode Rod employed as counter electrode, the green cable is connected to the reversible hydrogen electrode employed as the reference electrode, while the red and the green banana connector are respectively wired to the working electrode and the ground connection. Cell close up displaying WE, CE, and the Luggins tube (right).*

The AOR tests were carried out both in an inert environment (introducing argon) as well as in an atmospheric environment. In particular, the cell was filled with 63 mL of supporting electrolyte, namely 0.1 M NaOH. The working electrode, the counter electrode, and the Luggins Tube containing the reference electrode were also added to this cell to perform the first part of the procedure; in particular, a linear sweep voltammetry using a Pt wire as WE was first done as reference for any possible shift due to the reference electrode. Then, the Ni-catalyst was put into solution and the pre-test was carried out to verify the correct behavior of the electrode. Subsequently, the 200 cycles activation process was performed, followed by the CV and the LSV in the supporting electrolyte. Afterward, the analyte, namely $(NH_4)_2SO_4$ was added to the solution to perform again the Pt LSV, then CV test and the LSV test for the Ni electrode with the parameters described in Table 4.3 were performed. The composition of the solution for the ammonia measurements consisted of 0.2 M NaOH + 0.1 M $(NH_4)_2SO_4$.

When the cell is working in an inert environment, argon is bubbled inside the cell for at least 1 hour, to ensure the elimination of all the oxygen present in the basic solution, usually considerably harder to deoxygenate concerning an acidic media. The complete elimination of oxygen is tested by carrying out a CV with a Pt wire to see the adsorption and desorption peaks of hydrogen on the three exposed

faces of the Pt. For the measurements in a controlled environment, the cell was filled with a total and fixed volume of 63 mL of supporting electrolyte, and 3.31 mL of 2M $(NH_4)_2SO_4$ to ensure the same molarity, and therefore, the same experimental conditions as in the non-deoxygenated cell test configuration.

4.7 Electrochemical Procedure

Once the cell setup is completed, whether in the presence of oxygen or an inert environment, the following electrochemical procedure was applied to the synthesized materials to test their activity towards the AOR. The electrochemical procedure with the specified parameters is reported in Table 4.3 and was applied as follows: a CV and a LSV of a Pt were carried out to monitor the presence of oxygen and eventually to solve any problem that may arise from the reference electrode. The Pt wire used for testing was first wet and put under flame to ensure the cleanliness and readiness of the Pt surfaces.

Subsequently, a pre-test CV was executed to ensure the actual presence of the catalyst and its response, to then pass to a 200 cycles activation process to allow good hydration of the catalyst and ensure the exposure of the maximum possible number of active nickel sites. A CV and a LSV were then carried out to establish the performance of the material. In particular, the focus was set on the Ni^{2+}/Ni^{3+} oxidation peak (around 1.35-1.45 V vs RHE) and the presence of Oxygen Evolution Reaction (OER) occurring at very similar potential as the nickel oxidation (around 1.55-1.6 V vs RHE)[5].

Finally, the activity towards the ammonia oxidation reaction was evaluated by performing the same CV and LSV in the presence of the ammonia. This procedure was used to test and evaluate all the available nickel morphologies. Since one of the materials, namely the sample TR4, was synthesized using a Cu_2O template, the electrochemical response of this material and the pure glassy carbon electrode electrochemical response were studied with the parameters found in Table 4.3. Here, the parameters for evaluating the electrochemical behavior of the Cu_2O template and pure glassy carbon electrode are also reported. The parameters reported in this table are:

- Start potential (V): The initial potential applied to the electrode, that is the starting point of the electrochemical measurement and the starting point of the chosen potential window.
- Upper vertex potential (V): The maximum value of the potential applied to the electrode; in the case of a CV this is the upper limit of the applied potential before inverting the sign of the potential. In the case of a LSV, the upper vertex potential is replaced by the stop potential.

For that, in the following table, the symbol '/' in the UVP box will denote the uselessness of the parameter.

- Lower vertex potential (V): The lowest value of the potential applied to the electrode; in the case of a CV, this is the lower limit of the applied potential before inverting the sign of the potential. In the case of a LSV, the lower vertex potential is replaced by the start potential. For that, in the following table, the symbol '/' in the LVP box will denote the uselessness of the parameter.
- Stop potential (V): The value of the applied potential at which the electrochemical measurement stops.
- Scan rate (V/s): The speed at which the potential applied to the electrode is varied.
- Number of cycles: In the case of a CV, this is the number of times the chosen potential window is applied to the electrode. In the case of a LSV, this parameter is not required, as the linear scan does not perform a cycle. For that, in the following table, the symbol '/' in the number of cycles box will denote the uselessness of the parameter

***Table 4.3**: Experimental parameters used for the conventional electrochemical characterization of the samples.*

Name	Start potential (V)	Upper vertex potential (V)	Lower vertex potential (V)	Stop potential (V)	Scan rate (V/s)	Number of cycles
Pt CV	0.4	1.5	0.05	0.41	0.05	10
Pt LSV	0.4	/	/	-0.1	0.002	/
Pre-test	0.8	1.6	0	0.81	0.1	3
Activation	1	1.6	1	1.01	0.1	200
Test CV	1	1.55	1	1.01	0.005	6
Test LSV	1	/	/	1.6	0.002	/
Ammonia Test CV	1	1.55	1	1.01	0.005	6
Ammonia Test LSV	1	/	/	1.6	0.002	/
Cu_2O Test	0.2	1.5	-0.35	0.2	0.05	10
Glassy Carbon Test	0.2	2	-1	0.2	0.1	10

The complete procedure is valid for any environment present in the cell, whether exposed to air, or saturated with argon gas or oxygen. The only difference arises in the cell setup as the deoxygenation procedure is introduced. In the case of oxygen saturation, oxygen flow was introduced into the cell for at least 30 minutes to ensure the saturation of the cell.

4.8 Differential Electrochemical Mass Spectrometry (DEMS)

The *in-situ* DEMS characterization was carried out to register the m/z ratio of oxygen, molecular nitrogen, and any other NO_x products generated during the eAOR. The DEMS electrochemical cell is represented in Figure 4.5 (a). The cell presents a hole in the bottom part, on top of which a porous steel frit and a Gore-Tex membrane are placed. This hole ensures connection to the vacuum chamber underneath it and the collection of volatile products, avoiding any liquid leaks into it.

Figure 4.5*: The electrochemical cell used in the DEMS system (a) with the glassy carbon rod used as CE, the RHE used as RE inserted in the Luggins tube, and the Teflon-wrapped glassy carbon rod touching the WE carbon cloth placed right on top of the Goretex membrane and the steel fritz above the connection to the vacuum chamber.*

The working electrode consists of a 6 mm diameter carbon cloth on top of which 10 µL of TR4 catalyst is dropcasted. Once dried, the carbon cloth is placed in contact with the Gore-Tex membrane on the bottom, and a Teflon-wrapped glassy carbon rod is lowered and placed in contact with the upper surface of the cloth, both to ensure the proximity and stability of the membrane-cloth system and for electrical connection. The Teflon wrapping is necessary to isolate the rod's side surfaces from the liquid, that would cause electrochemical reaction to proceed along the exposed surface. In this way, only the glassy carbon rod lower surface will transfer the electrical potential to the catalyst cloth to allow the electrochemistry to proceed, and volatile and gaseous products will immediately flow

through the membrane into the connected vacuum chamber. The CE consists of the classic glassy carbon rod and the RE consists of a RHE inserted inside a Luggin's tube filled with the same solution of the cell. A bubbler is also added to allow the flow of gases to change the environment of the cell, in this case pumping a flow of argon gas to ensure an inert environment or an oxygen flow. The cell was filled with 17 mL of supporting electrolyte (0.2 M NaOH) and 4 mL of $(NH_4)_2SO_4$ was added when needed. The parameters for the measurements are described in Table 4.4.

Once the cell setup is complete, a rotatory pump is switched on to reach the working pressure of the first vacuum chamber before opening the connection to the ionization chamber. Then, the two chambers can be connected and once the vacuum level is stable it is mandatory to allow the stabilization of the filament to serve as a cathode for the mass spectrometer. This is a critical step, as it can have potentially negative influence over the measurement and alter the status of the apparatus. This procedure is carried out by selecting the m/z signal with the software and switching on the filament for at least 3-4 hours to let any dirt particles or other surface contaminants leave the surface of the incandescent filament, leaving it ready for measurement and avoiding characteristic peaks, noise, and overall signal alteration coming from species not involved in the reaction of interest. After this time, if the differential pressure signal of the selected species in the chamber is stable, the measurement can proceed. The software QADSTAR-32 bits controls the instrument, which allows the optimization of the remaining parameters on the screen, in order to have better visualization of the signals like the ionization chamber pressure signal (PKR), the applied potential signal, and the ionic current, which corresponds to the m/z signal of the species.

The whole measurement procedure for the eAOR, O_2 (m/z=32), N_2 (m/z=28), NO (m/z=30), and NO_2 (m/z=44), species detection both in argon-saturated and oxygen-saturated cells will be described. After the stabilization of the cathode, the cell was initially filled with argon gas to ensure an inert environment, essential to proceed with an efficient activation of the catalyst and prepare the electrode's surface. Then, with the help of the NOVA and QADSTAR-32 bits softwares, the electrochemical and m/z parameters were set. CVs and MSCVs were recorded at 0.5 mV/s. In the case of the argon measurement no further setup is needed as the cell is already filled with inert gas, while for the oxygen measurement, argon is removed after the activation procedure by pouring oxygen gas and allowing complete saturation. For both cases, after the environment of the cell was established, a preliminary CV in supporting electrolyte was launched following the m/z signals indicated. This was done to detect any strange behavior of the catalyst, or the presence of undesired products; as a matter of fact, if only the supporting electrolyte is present the only detectable signal should be the oxygen coming from the Oxygen Evolution Reaction (OER) and no nitrogen species

should be present. For these preliminary tests, the signals for the OER, N_2, NO, N_2O, and the m/z = 22 in an argon- and oxygen-saturated environment were recorded. The latter m/z signal was monitored to make sure that the m/z= 44 signal, which can be attributed to both the N_2O species and the CO_2, was indeed proof of the N_2O presence. The signal m/z = 22 is related to [CO_2^{++}] species, an ion fragment deriving from carbon dioxide, which could potentially come from the oxidation of the carbon cloth. Thus, the absence of a contribution to this m/z ratio ensures the absence of CO_2 production. This procedure was employed both for the argon-saturated cell and for the oxygen-saturated cell in supporting electrolyte, and in the presence of ammonia.

For the ammonia measurements, 4 mL of $(NH_4)_2SO_4$ was added recording the same m/z signals. This time the mass spectrometer should yield the expected nitrogen and nitrogen dioxide species formed on the catalyst surface, as well as the oxygen coming from OER. It is important to specify that, while it is convenient to monitor multiple m/z simultaneously, there is an intrinsic limit to the instrument's sensitivity, which is greatly affected by the number of preset m/z signals. The spectrometer can only analyze one ionized species at a time, so there can be a great delay between the detection of the first species and the immediately following ones, and as the electrochemical reaction proceeds, this can affect the correlation between the detected ions and the faradaic curve. However, this can be overcome by selecting the relevant mass signals and optimizing other parameters such as the potential window and the scan rate to ensure the best response of the instrument.

In summary, the synthesis of all the materials has been discussed, along with the description of experimental setups and the electrochemical parameters needed to characterize the samples. The obtained results will be discussed trying to correlate the information obtained from all the physicochemical characterization techniques employed with the electrochemical response of these materials. Also, the problems faced during the experiments will be addressed, as well as the impact they had on the results. Possible solutions to these problems and how to optimize these procedures will be debated.

Bibliography

1. Zhao, W., Zhang, C., Geng, F., Zhuo, S. & Zhang, B. Nanoporous hollow transition metal chalcogenide nanosheets synthesized via the anion-exchange reaction of metal hydroxides with chalcogenide ions. *ACS Nano* **8**, 10909–10919 (2014).
2. Wang, Y., Zhu, Q. & Zhang, H. Fabrication of β-$Ni(OH)_2$ and NiO hollow spheres by a facile template-free process. *Chem. Commun.* **41**, 5231–5233 (2005).
3. Tian, L., Yang, T., Pu, W. *et al.* Synthesis of cubic $Ni(OH)_2$ nanocages through coordinating etching and precipitating route for high-performance supercapacitors. *Nanoscale Res. Lett.* **14**, 264 (2019).
4. Xu, F., Hu, K., Wang, S. *et al.* ZIF-8 derived $Ni(OH)_2$ hollow nanocages for non-enzymatic glucose electrochemical sensing. *J. Mater. Sci.* **57**, 18589–18600 (2022).
5. Łuczak, J. & Lieder, M. Nickel-based catalysts for electrolytic decomposition of ammonia towards hydrogen production. *Adv. Colloid Interface Sci.* **319**, 102963 (2023).
6. Camargo, J.R., Orzari, L.O., Araújo, D.A.G. *et al.* Development of conductive inks for electrochemical sensors and biosensors. *Microchem. J.* **164**, 105998 (2021).
7. Swain, G.M. Solid electrode materials: Pretreatment and activation. In *Handbook of Electrochemistry* (ed. Zoski, C.G.) 111–153 (Elsevier, 2007).
8. Napporn, T.W., Holade, Y., Kokoh, B. *et al.* Electrochemical measurement methods and characterization on the cell level. In *Fuel Cells and Hydrogen* (eds Hacker, V. & Mitsushima, S.) 175–214 (Elsevier, 2018).
9. Arulmozhi, N., Esau, D., van Drunen, J. & Jerkiewicz, G. Design and development of instrumentation for the preparation of platinum single crystals for electrochemistry and electrocatalysis research: Part 3—final treatment, electrochemical measurements, and recommended laboratory practices. *Electrocatalysis* **9**, 1–11 (2018).

CHAPTER 5

5.1 Results and Discussion

In this section, the electrochemical responses of the synthesized materials towards the eAOR will be evaluated and linked to the information retrieved thanks to the physicochemical characterization techniques employed during the study.

5.2 Scanning Electron Microscope (SEM) & Energy Dispersive X-Ray Spectroscopy (EDS)

SEM images of the different synthesized materials are reported in Figure 5.1. Regarding the TR1 sample (Figure 5.1 (a)), the images reveal the absence of the desired hexagonal structures for this sample[(1)], the absence of nanoparticles and the presence of large agglomerates. For sample TR2 (Figure 5.1 (b)), a spherical morphology is observed. Several two-dimensional nanosheets make up the microsphere structure, and the dimensions align with the expected values of 1-3 μm diameter[(2)]. Sample TR3 (Figure 5.1 (c)) also did not show the expected nanoflower shape (1). No discernible morphology is observed with agglomerates of material of varying sizes. The TR4 sample (Figure 5.1 (d)) was synthesized starting from a cubic Cu_2O template as explained in the Experimental Section and SEM images confirm the presence of $Ni(OH)_2$ hollow nanocages[(3)]. The images confirm the issues encountered in the synthesis of sample TR5 (Figure 5.1 (e)). TEM characterization (next section) will confirm the disordered cluster obtained for the TR5. Sample TR6 was not characterized with SEM as it was synthesized later on and was only characterized with Transmission Electron Microscopy.

EDS analysis provided the average atomic composition of the obtained materials, confirming the nickel hydroxide formation. It showed the presence of Cu atoms in TR4; this sample was the only one synthesized with the help of a copper template, therefore no copper presence is expected for the other samples. Later, the Cu presence in TR4 will be more accurately identified thanks to ICP-MS. Sample TR6 was not characterized with EDX as it was synthesized later on in the project and will be characterized by means of ICP-MS to retrieve the atomic composition.

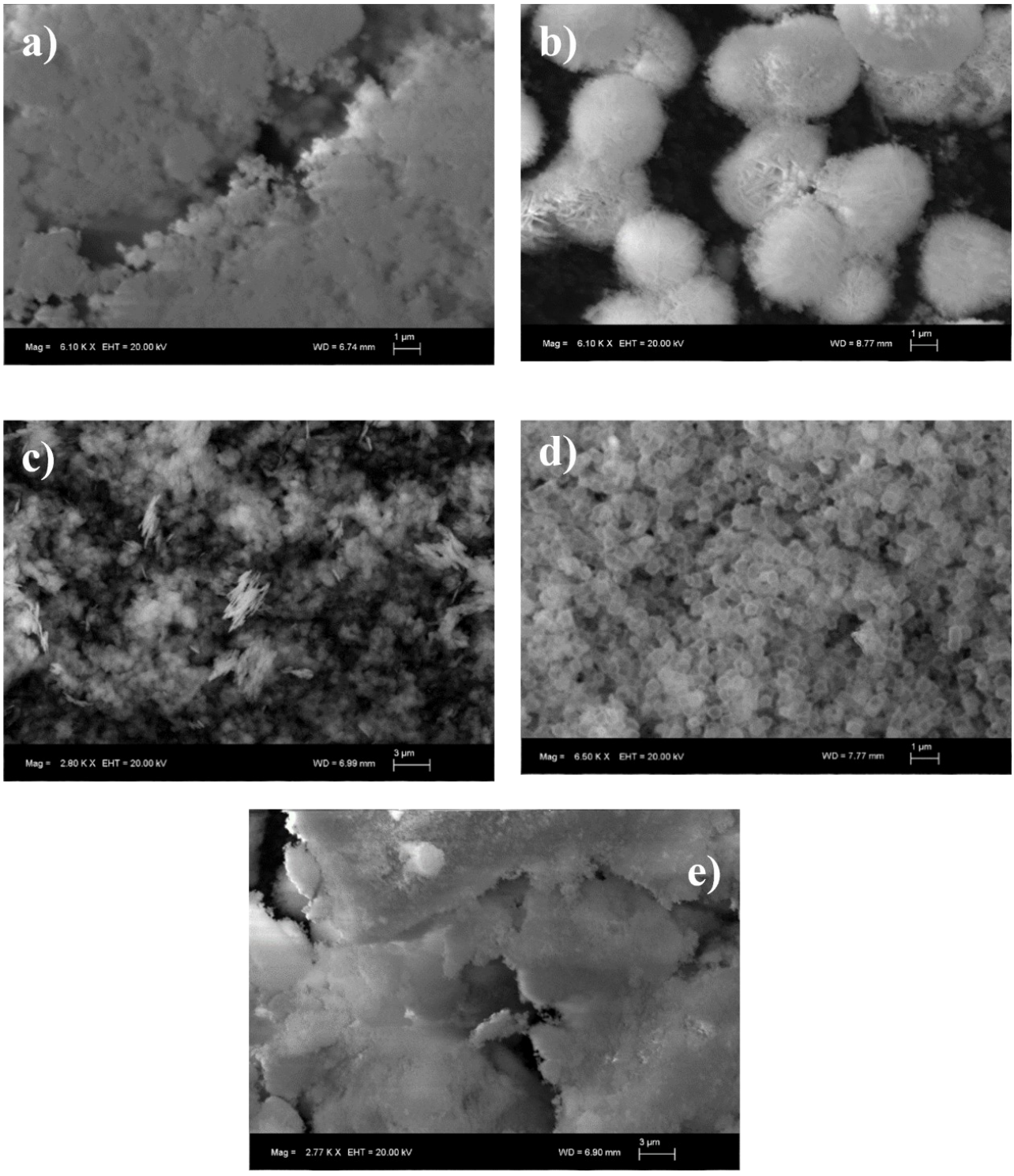

Figure 5.1*: SEM images of the samples showing the resulting morphologies for TR1 sample (a), TR2 (b), TR3 (c), TR4 (d), and TR5 (e).*

***Table 5.1**: EDX analysis results expressed in atomic percentage for the different elements composing synthesized materials.*

Sample	Ni atomic %	O atomic %	Cu atomic %
TR1	37.34	62.66	/
TR2	38.47	61.53	/
TR3	29.08	70.92	/
TR4	21.18	71.30	7.52
TR5	41.15	58.85	/

An example of EDS analysis is given below in Figure 5.2, showing the elemental composition and distribution for TR4 throughout the selected area. As already discussed, this is a widely employed and useful technique to establish the elemental composition, although sensitivity is often a limiting factor. In this case, the right layered image (b), represents the superposition of all the different elemental mapping shown for O (c), Ni (d) and Cu (e). In all cases, a uniform distribution of the elements is observed.

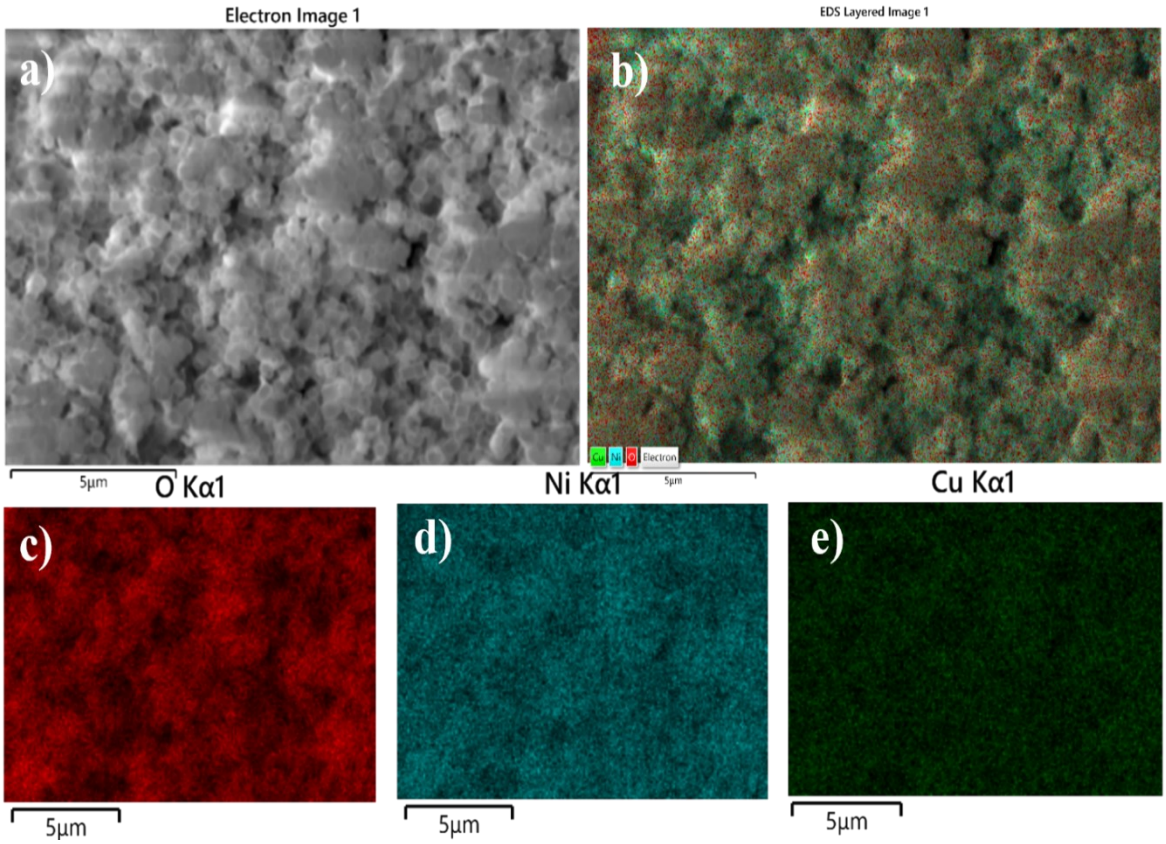

***Figure 5.2**: EDS elemental mapping for the sample TR4. Image (a) shows the SEM image of the selected area, while (b) shows the elemental mapping, statistical distribution of the elements in that same area. Images (c), (d), and (e) represents individual elemental mapping for O, Ni and Cu elements, respectively.*

5.3 Transmission Electron Microscope (TEM)

Figure 5.3 shows the TEM images of TR4, TR5, and TR6 samples. They provide further information about their morphology, and the dimensions of the synthesized nanoparticles. Figure 5.3 (a)-(b) displays agglomerates and single particles of the copper template and its cubical morphology, as expected from literature work confirming the successful synthesis[3,4,5]. The darker area highlights the bulk nature of the template that, as explained in the Experimental Section, will adsorb Ni atoms on its surface following an etching and precipitation reaction to form the $Ni(OH)_2$ hollow nanocages. This fact is further confirmed when looking at Figure 5.3 (c)-(d), showing the TR4 hollow structure, and the lighter contrast with respect to the template's structure. From these pictures it is possible to suggest that remaining copper particles stuck near the freshly synthesized hollow nanostructure in the form of small clusters.

As already mentioned for SEM characterization, TEM images of the TR5 sample in Figure 5.3 (e)-(f) prove the issues encountered during the multiple syntheses where a random and most likely layered assortment of particles is seen.

Lastly, Figure 5.3 (g)-(h) reports TR6 images, characterized by the presence of Ni atoms on the surface, ideally forming a monolayer. These images allow to appreciate the differences in the synthesis routes for the preparation of the TR4 and TR6 samples, as it is evident how the etching and precipitation mechanism was carried out successfully for the TR4, leaving behind the hollow structure, while for the TR6 the whole and bulk nature of the copper templated is preserved.

5.4 Inductively Coupled Plasma-Mass Spectrometry (ICP-MS)

ICP-MS was used to analyze the atomic composition of TR4 and TR6 samples. Both samples were synthesized starting from Cu_2O precursor to obtain the desired morphology; therefore, this type of characterization was used to evaluate and quantify the presence of Cu atoms and their ratio with respect to the Ni atoms in the bulk of the materials. In Table 5.2, the elemental percentage values obtained with the characterization are reported.

Table 5.2*: ICP-MS analysis for the TR4 and TR6 samples.*

SAMPLE	Ni atomic %	Cu atomic %
TR4	74.1	25.9
TR6	10.4	89.6

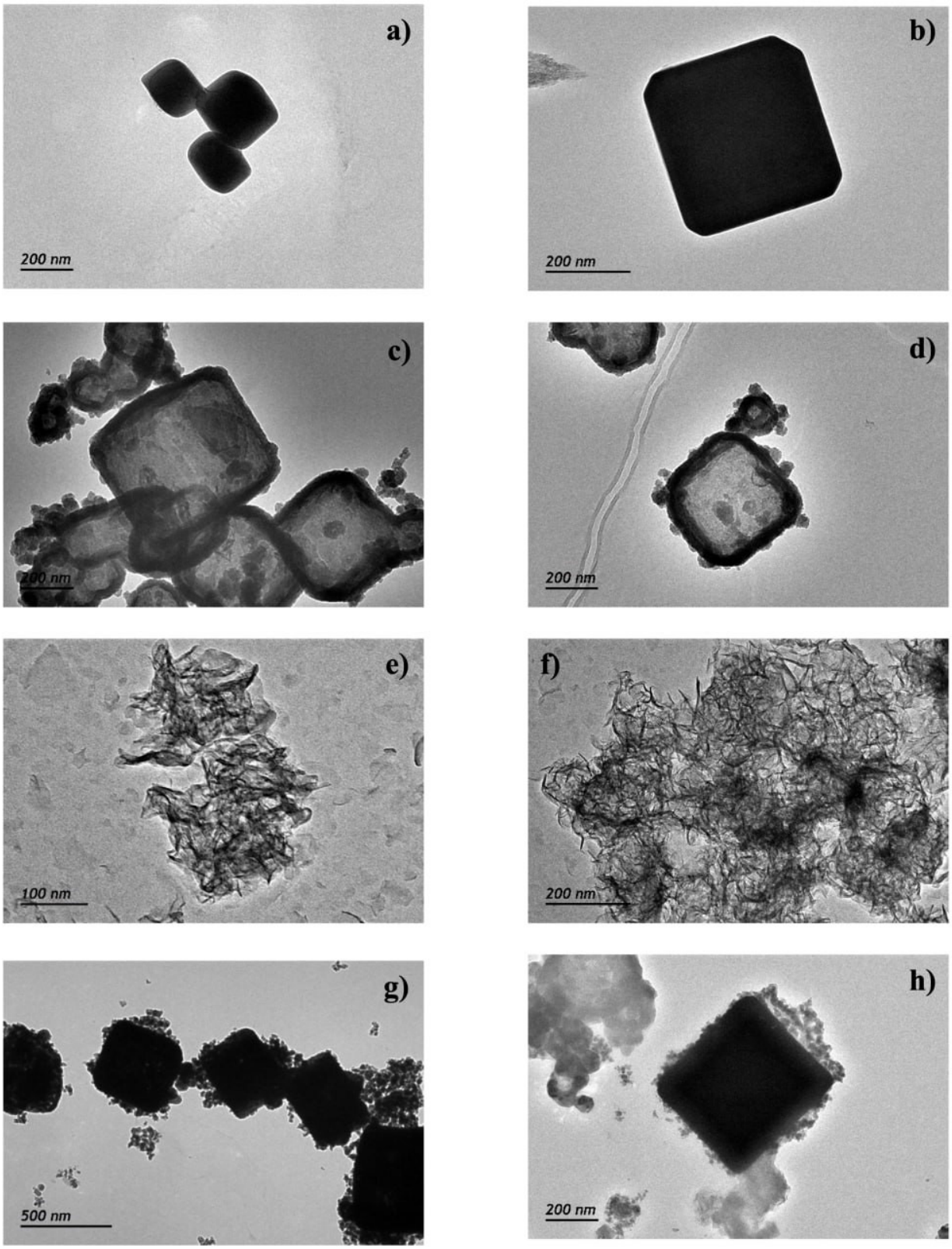

***Figure 5.3**: TEM images for the sample Cu_2O template(a)-(b), the TR4 hollow cages structure (c)-(d), the morphology of the TR5 (e)-(f), and the TR6 sample (g)-(h).*

The atomic percentage of Cu in the TR4 confirms the non-complete precipitation and dissolution of the copper precursor, to form the core-shell structure, since a complete synthesis would result in complete etching and precipitation of the Cu template, ultimately filtered, thus leaving no trace of Cu atoms. As expected, the TR6 sample shows a predominance of Cu with respect to Ni as the target morphology is a nanocage structure with ideally a monolayer of Ni atoms on the surface of the cages. However, it is important to specify that these values are representative of the bulk of the materials, and only XPS analysis will give access to surface composition and stoichiometry of the synthesized catalyst.

5.5 X-Ray Photoelectron Spectroscopy (XPS)

XPS measurements were carried out to determine the surface composition and the oxidation state of the different elements[6,7]. The surface composition can be directly related to the reactivity of these samples since only the surface of the nanoparticles will be in contact with the electrolyte and the reactants. For this reason, it is very important to investigate the species present on the surface. In particular, the Ni 2p, O 1s and Cu 2p XPS regions were acquired and analyzed.

Figure 5.4 (a) displays the Ni 2p region of all the synthetized catalysts. All the samples show a similar spectrum, which is characteristic of $Ni(OH)_2$[8,9]. It has two main peaks at 855.0 eV and 875.0 eV attributed to Ni $2p_{3/2}$ and Ni $2p_{1/2}$, and two satellite peaks at 865.0 and 880 eV[5]. Surprisingly, the intensity of the Ni 2p region for the TR6 sample was very low, compared with the other samples, indicating that the amount of nickel at the surface was small, in agreement with the ICP analysis presented above. This result will be further discussed below.

To confirm the presence of $Ni(OH)_2$ and/or other nickel species at the surface, the Ni 2p region was deconvoluted into chemically shifted components. Since the Ni 2p spectrum was the same for all the samples, the fit of the Ni $2p_{3/2}$ peak for TR5 is reported in Figure 5.4(b) as an example. It has to be highlighted that the chemical state XPS analysis of nickel and their oxides and hydroxides is challenging due to the complexity of their 2p spectra resulting from peak asymmetries, complex multiplet splitting, shake-up and plasmon loss structure[8,9]. For the fit, the method described by Biesinger in (9) was followed. The analysis was started just using the $Ni(OH)_2$ component that consists of six peaks and, as can be seen in Figure 5.4 (b), and a good fit was obtained. Therefore, no other components were included..

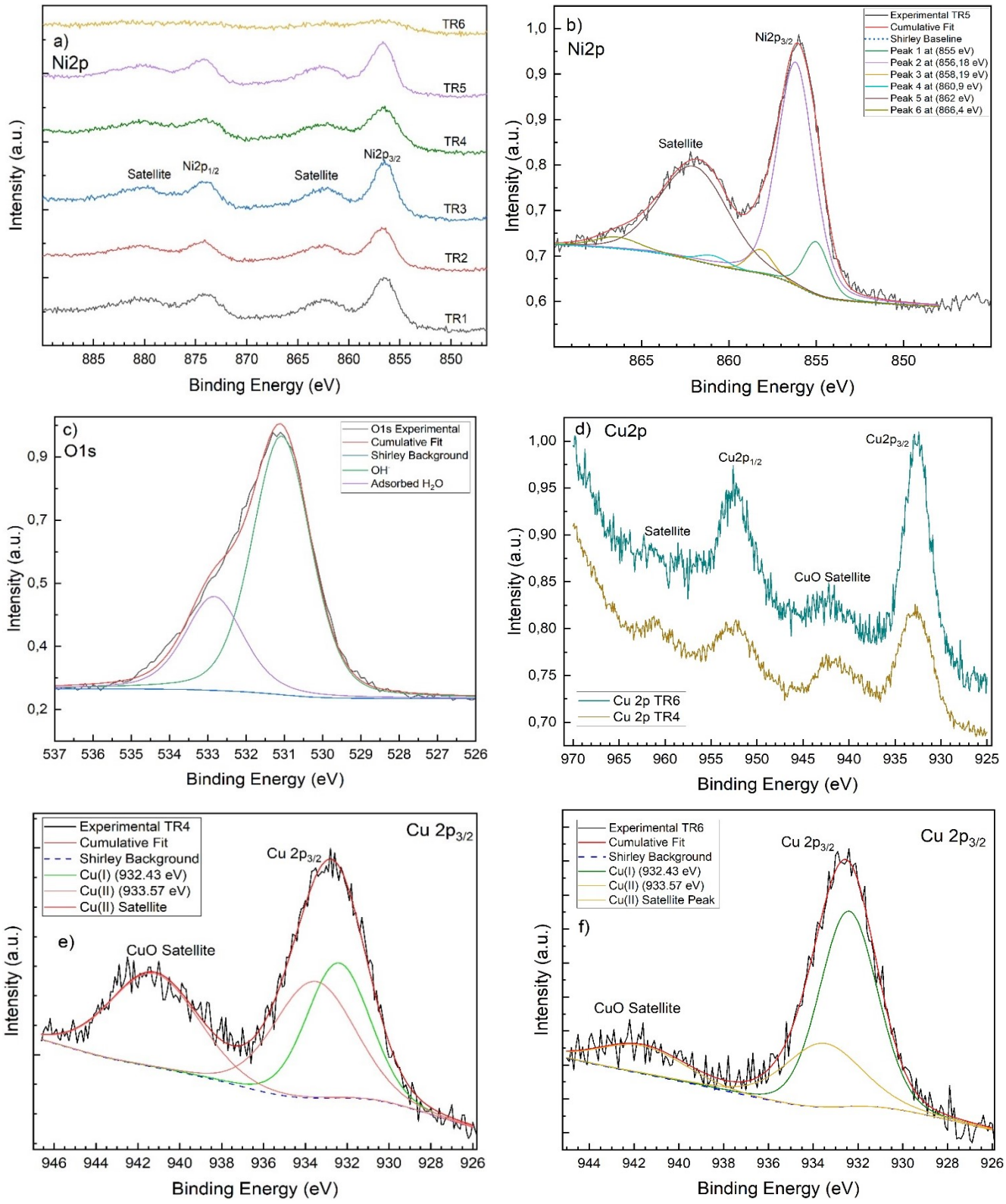

***Figure 5.4**: Ni 2p XPS region for all the $Ni(OH)_2$-based samples (a), example of deconvolution of the Ni $2p_{3/2}$ peak into chemically shifted components for TR5 (b). Example of deconvolution of the O 1s spectrum into chemically shifted components for TR5 (c), Cu 2p XPS region for samples TR4 and TR6 (d), and its deconvolution into chemically shifted components (e and f, respectively).*

All the samples presented two components in the O 1s regions with different ratio between them. For this reason, the deconvolution of the O 1s XPS region of the TR5 sample is shown in Figure 5.4 (c) as an example. The component located at 531.1 eV is typical feature of the Ni-O-Ni bond in the $Ni(OH)_2$ structure[8,9]. In addition, a second component centered at 532.9 eV was also present and can be attributed to adsorbed water.

The Cu 2p XPS region was analyzed for TR4 and TR6 and reported in Figure 5.4 (d). From the intensity of the satellite, it can be deduced that the oxidation state of copper in the two samples is different. To analyze the copper species, present in these samples, the deconvolution into different chemical components was performed (Figures 5.4 (e) and (f)). As can be observed, both samples contain Cu_2O and CuO species. In the case of the TR4 sample, CuO is the majority component and only a small amount of Cu_2O is present. On the contrary, the main component in TR6 is Cu_2O with only a small amount of CuO.

Figure 5.5 reports the survey spectra of TR4 and TR6 samples. Their comparison clearly shows that the surface Ni:Cu ratio is different in both cases. TR4 presents a small amount of copper, while TR6 shows a small amount of nickel. These results agree with the ICP data reported above. This is likely due to an incorrect synthesis in TR6, resulting in much more exposed copper than nickel on the surface.

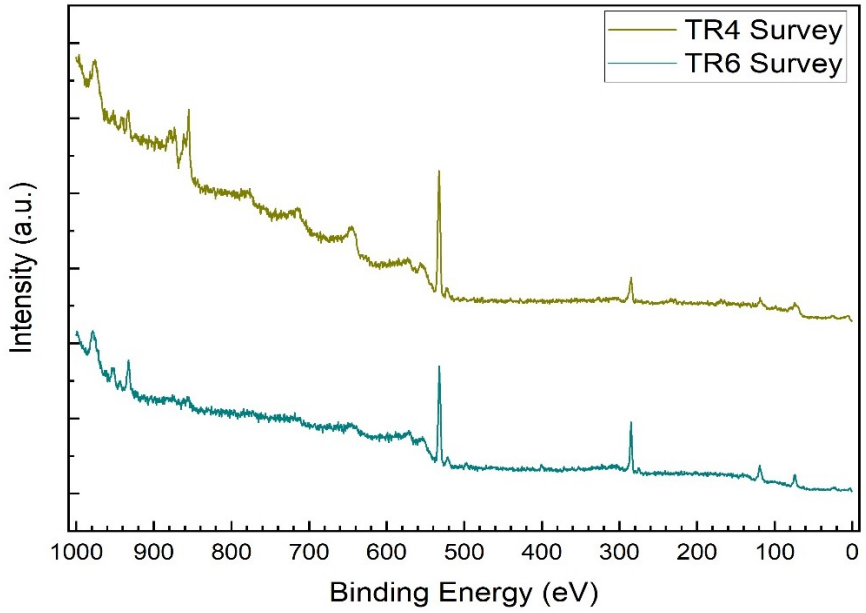

Figure 5.5: *XPS survey for the TR4 and TR6 samples.*

.

The surface stoichiometry was calculated considering the area of each region and the corresponding sensitivity factor. Results are reported in Table 5.3.

The atomic Ni:O ratio of 1:2 expected for $Ni(OH)_2$ is respected for samples TR1, TR2, and TR5. For sample TR3, the Ni:O ratio is slightly higher than expected, which could be attributed to the presence of a small amount of NiO due to the oxidation when exposed to air. TR4 displays a slightly smaller Ni:O ratio due to the presence of Cu. The TR6 displays a different ratio as well due to the presence of copper. From the TR6 stoichiometry we can see that the little amount of Ni (also confirmed with ICP-MS) present in this sample is predominantly present on the surface of the cubes, as visible in Figure 5.3 (g-h), where Ni is deposited on the surface of the Cu_2O cages.

Table 5.3*: Surface stoichiometry values were calculated for all the samples. The Ni:O ratio and the Cu presence have been evaluated confirming in most cases the 1:2 ratio for the* $Ni(OH)_2$.

Surface stoichiometry	**TR1**	**TR2**	**TR3**	**TR4**	**TR5**	**TR6**
Ni (at%)	36.2	32.0	41.5	23.2	38.7	3.6
O (at%)	63.8	68.0	58.5	65.6	61.3	89.2
Cu (at%)	/	/	/	11.2	/	7.1
Ni:O:Cu	1:1.8:0	1:2.1:0	1:1.4:0	2:5.8:1	1:1.6	1:24.7:1.9

5.6 X-Ray Diffraction (XRD)

Figure 5.6 (a) presents the diffractograms recorded for TR1, TR2, and TR3 samples, compared to a reference diffractogram obtained from international crystallography databases (Inorganic Crystal Structure Database (ISCD)). The analysis shows the presence of the crystalline structure of $Ni(OH)_2$, which aligns perfectly for samples TR1, TR2, and TR3 with the reference standard, specifically β-$Ni(OH)_2$, which belongs to the hexagonal crystal structure, P3m1 (No.164)[10]. For samples TR4 and TR5, however, notable differences are evident in Figure 5.6 (b), with a structure more closely resembling α-$Ni(OH)_2$, which includes intercalated water. It could also indicate a significant amorphous character due to high noise levels and the complete absence of peaks corresponding to some, if not many, crystal planes, as it is known that the low degree of crystallinity decreases the intensities of the peaks[11].

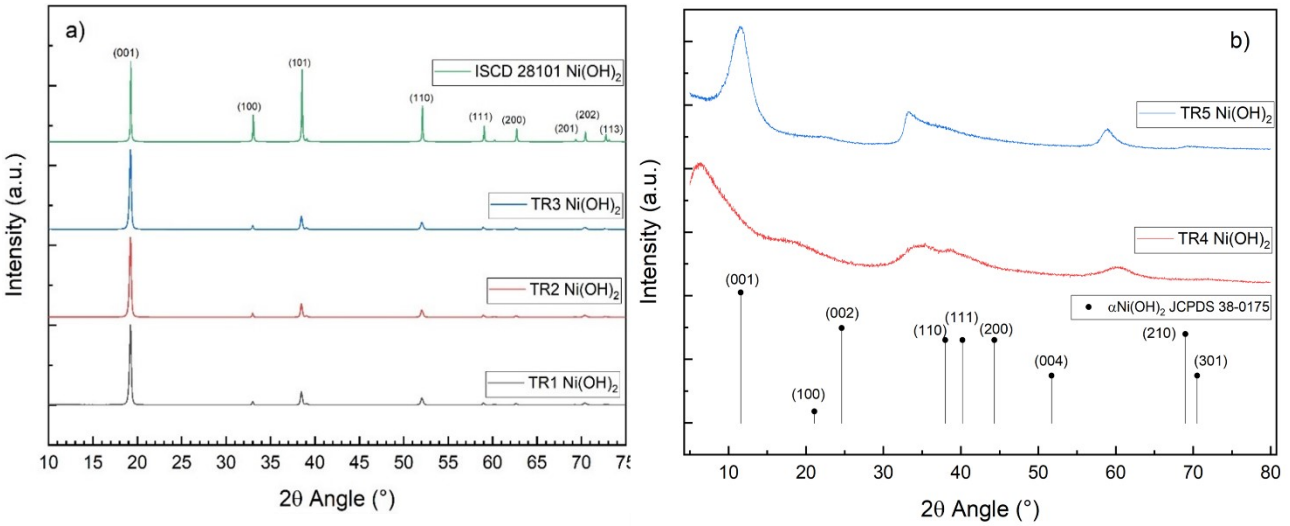

Figure 5.6: *XRD pattern for TR1, TR2, TR3 samples, and ISCD 28101 β- $Ni(OH)_2$ reference (a), and (b) XRD patterns for sample TR4, TR5, and JPCSD 38-0175 α-$Ni(OH)_2$ reference. The amorphous nature of TR4 and TR5 catalysts is observable although there is a clear resemblance to the alfa hydroxide structure.*

Regarding the TR6 sample, XPS characterization showed the low amounts of Ni present in the structure, and in fact, the XRD diffractogram also proves the absence of Ni, suggesting the superposition of these peaks with the Cu ones, or more likely (according to other physicochemical results) confirming the little amount of this element. The XRD diffractogram of the Cu_2O template is also reported.

Using Scherrer analysis, the average crystallite size was determined for all the samples, allowing the analysis to fit the peak to determine the FWHM. These values were first calculated by obtaining the interplanar distance ('d-spacing' (Å)) using Bragg's law, then applying the equation governing hexagonal crystal systems to determine the cell parameters 'a'='b' and 'c'. The equation is described as follows:

$$\frac{1}{d^2}(\text{Å}) = \frac{4}{3}\left(\frac{h^2 + hk + k^2}{a^2}\right) + \frac{l^2}{c^2} \qquad (5.1)$$

Where '*d*' represents the interplanar distance ('d-spacing' in Å), and '*h*', '*k*', and '*l*' are the Miller indices, while '*a*' and '*c*' are the cell parameters. The desired values are obtained by selecting the *h, k, and l* indices of two distinct peaks and solving the equation for the cell parameters. The values found in the literature are *'a'* = 3.125 Å and *'c'* = 4.605 Å[10]. The calculated values for the samples TR1, TR2, and

TR3 are ‘a’ = 3.13 Å, ‘c’ = 2.30 Å. Intense and sharp peaks are observed for these samples, meaning that the crystallites producing that signal are bigger than if the peaks were broader.

The average crystallite size calculated for all catalysts is reported in Table 5.4. The particle sizes agree with those observed from SEM and TEM images. For the TR4 and TR5, the amorphous nature of the samples and the consequent broadening of the peaks did not allow a facile Scherrer analysis and determination of the lattice parameter. However, the calculated crystallite dimensions are reported as well, and they appear significantly lower than the other samples.

***Table 5.4**: Average crystallite size calculated with the Scherrer formula for the samples analyzed. These values were calculated by retrieving the FWHM of the peaks and using mathematical relations to correlate the crystallite dimensions to the signal. X-ray radiation of Cu Kα (1.54 Å) was used.*

Sample	***Average Crystallite Size (nm)***
TR1	32.90
TR2	32.80
TR3	32.91
TR4	2.13
TR5	3.40
TR6	14.6

5.7 Electrochemically Active Surface Area (ECSA)

ECSA calculated values (in cm^2) are reported in Table 5.6 for all the synthesized materials. The procedures to obtain this parameter have been explained in the Introduction and Experimental Section. ECSA can be determined from the coulombic charge associated to characteristic reactions occurring on the surface of some electrodes, such as hydrogen underpotential deposition[12]. In the case of the catalyst studied in the present work, these values are calculated from the integration of the peak observed for the redox process between Ni^{2+} and Ni^{3+}, as shown in Figure 5.7. The charge associated with this reaction is 514 μC cm^2, which corresponds to the 2-electron transfer to form one monolayer of $Ni(OH)_2$[13,14,15]. All the samples characterized in this work presented these peaks, and the calculated values are reported in Table 5.6. In some cases, there are discrepancies between the values calculated from the oxidation and reduction peaks, a result explained of the overlapping between the currents associated to the redox process Ni^{2+}/Ni^{3+} and the OER. An example of the fitting

process for the peak integration method is reported in Figure 5.7, which shows both integrated peaks for the sample TR2.

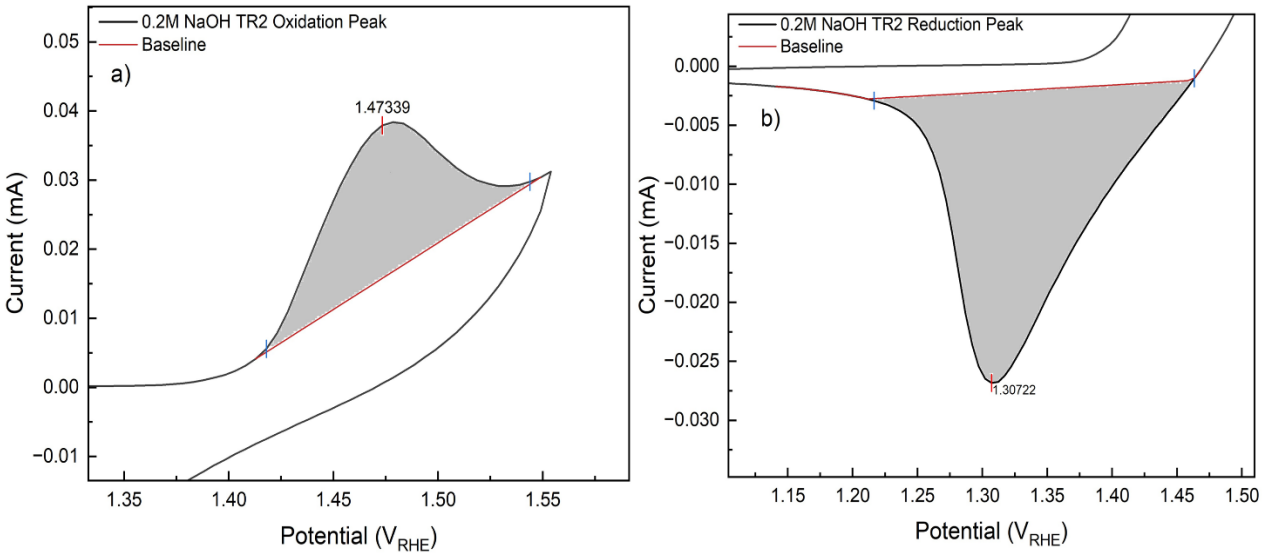

Figure 5.7*: Example of the oxidation (a) and reduction (b) peak integration method for the ECSA calculation for the sample TR2. The integrated area, showed in grey, is directly proportional to the charge and so to the number of active catalytic sites.*

Regarding TR1 and TR3 samples, the calculated values do not significantly differ between the two peaks, although the oxidation peak value is smaller than that of the reduction peak, probably highlighting the interference of the OER as aforementioned. For TR2 it is plausible that the overlapping currents are higher, resulting in a bigger discrepancy between the values.

The integrated peak method is based on the presence of the Ni^{2+}/Ni^{3+} redox pair. However, it was previously established that Cu is present on the surface of the catalyst for TR4 and TR6 samples, therefore lowering the number of Ni active sites. Then, for these catalysts, the double layer or capacitance method has been employed to calculate a more accurate value of the ECSA. This experiment consists of obtaining CV curves for monitoring the collected current as a function of the applied potential at increasing scan rates, ranging from 5 mV/s up to 200 mV/s (see Figure 5.8 (a)). Afterwards, the value of the anodic and cathodic current at a specific potential of the double layer formation is selected for the different voltammograms at several scan rates. The difference between the selected cathodic and anodic values are fitted to a linear trend, as shown in Figure 5.8 (b). The slope of this curve (applying Equation 2.12) and a constant value for the specific capacitance C_s of 40 μF cm^{-2} [12,15,16] are used to calculate the ECSA values, which are reported in Table 5.7. For sample

TR4, the potential value chosen for the analysis was 0.552 V vs RHE, whereas for the TR6 it was fixed at 0.90 V vs RHE. Both potentials are in the range where the double layer formation takes place.

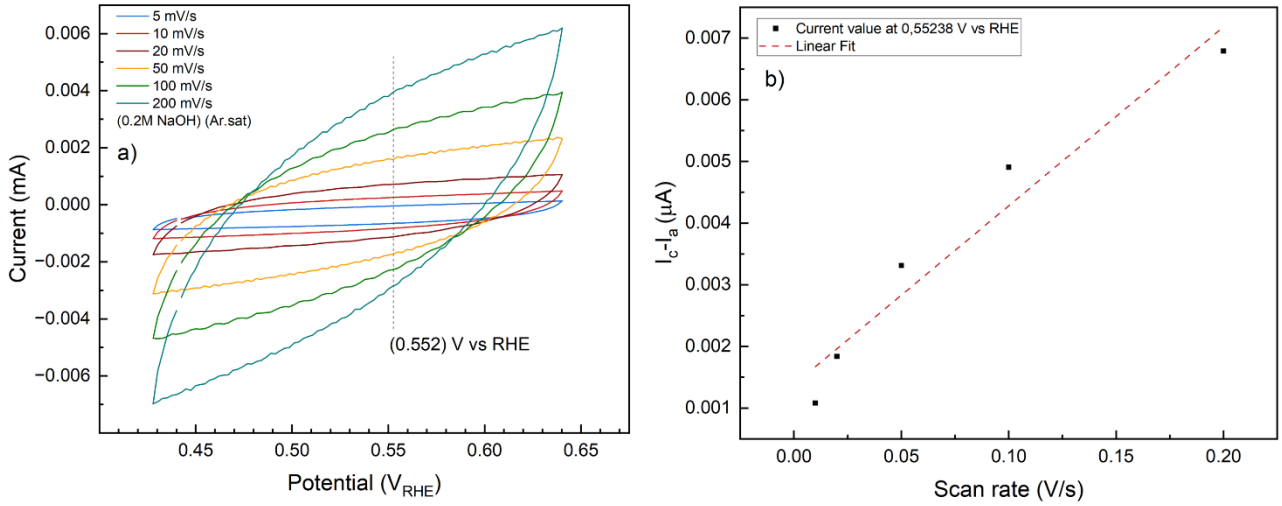

***Figure 5.8**: Cyclic voltammetry (a) for the TR4 sample at increasing scan rates to determine the ECSA with the double-layer or capacitance method; and (b) linear fit of the branch current vs scan rate plot used to determine the slope of the plot.*

***Table 5.5**: ECSA values calculated with the redox peak integration method for all the synthesized samples.*

Sample	*ECSA* (cm^2) Oxidation Peak Integration	*ECSA* (cm^2) Reduction Peak Integration
TR1	0.61	0.71
TR2	0.55	1.03
TR3	0.47	0.51
TR4	0.012	0.012
TR5	5.16	2.45
TR6	0.49	1.59

***Table 5.6**: ECSA values calculated with the double-layer method.*

Sample	*ECSA* (cm^2)
TR4	0.72
TR6	0.35

Comparing the value obtained for TR4 using the peak integration method with that in Table 5.6, the difference is striking. The value is 70 times higher in Table 5.5, probably because of the contribution of all active sites, including those originating from copper, which were not considered in the integration of the redox peaks of Ni. As previously explained, in the integrated peak method, the area was related only to the number of active Ni sites. It is remarkable that in the TR4 sample, CuO is the predominant oxide. In contrast, for the TR6 sample, ECSA values are in the same range with both methods. This could be explained by the hypothesis that, in this case, the amount of copper is considerably higher than that of Ni (ICP-MS analysis) and a very small amount of superficial Ni is present in the sample (XPS spectra); but as a difference with the TR4, Cu_2O is the more relevant oxide in the sample and it seems to be less active, not contributing to the electroactive area.

5.8 Conventional Electrochemical Characterization

LSV curves at 2 mV/s in the base electrolyte and in ammonia solution were recorded for all the materials. Results are given in Figure 5.9 for those catalysts containing only Ni (TR1, TR2, TR3, and TR5 samples) and Figure 5.10 for those containing Ni and Cu (TR4 and TR6 samples). The electrochemical measurements are normalized by the ECSA determined in the previous section; therefore, the reported values are given as current density 'j' (mA/cm^2) which is the amount of current flowing per electrochemical active area. ECSA calculated from the peak integration method was used for TR1, TR2, TR3, and TR5 samples, whereas that obtained from the double layer procedure was applied for the TR4 and TR6 materials.

It is observed in Figure 5.9 that the reactivity towards the electrochemical oxidation of ammonia (eAOR) for the Ni-containing materials is very low. As already discussed, the first step for the ammonia oxidation involves the formation of the active catalyst, namely NiOOH. The blue curves in Figure 5.9 display the LSV in the deoxygenated supporting electrolyte. The onset potential for the transition of the Ni^{2+}/Ni^{3+} is found at 1.305 V vs RHE and 1.370 V vs RHE, for TR1 and TR2, respectively. The transition from $Ni(OH)_2$ to NiOOH is clearly highlighted by the oxidation peak at 1.359 V vs RHE for TR1, and at 1.437 V vs RHE for TR2.

On the other hand, the red curve corresponds to the LSV after the ammonia sulphate is added to study the eAOR. An increase in the oxidation peak current is detected for the TR1 and TR2 samples, reaching current values of 29.0 μA/cm^2 and 16.30 μA/cm^2, respectively, higher than the values of 15.7 μA/cm^2 and 8.90 μA/cm^2 achieved in the absence of ammonia, for TR1 and TR2, respectively. However, the net increase in the current is small, indicating a remarkable degree of inactivity of the materials that could be due to many factors: the presence of a passivation layer of inactive nickel oxide, the incomplete and inhomogeneous activation of the surface; or a high resistance due to an incorrect dispersion and loading of the catalyst ink on the surface of the electrode. Additionally, SEM images of the TR1 sample highlight the lack of the desired morphology, which could be the reason for the inactivity obtained with respect to that described in the literature[(1)].

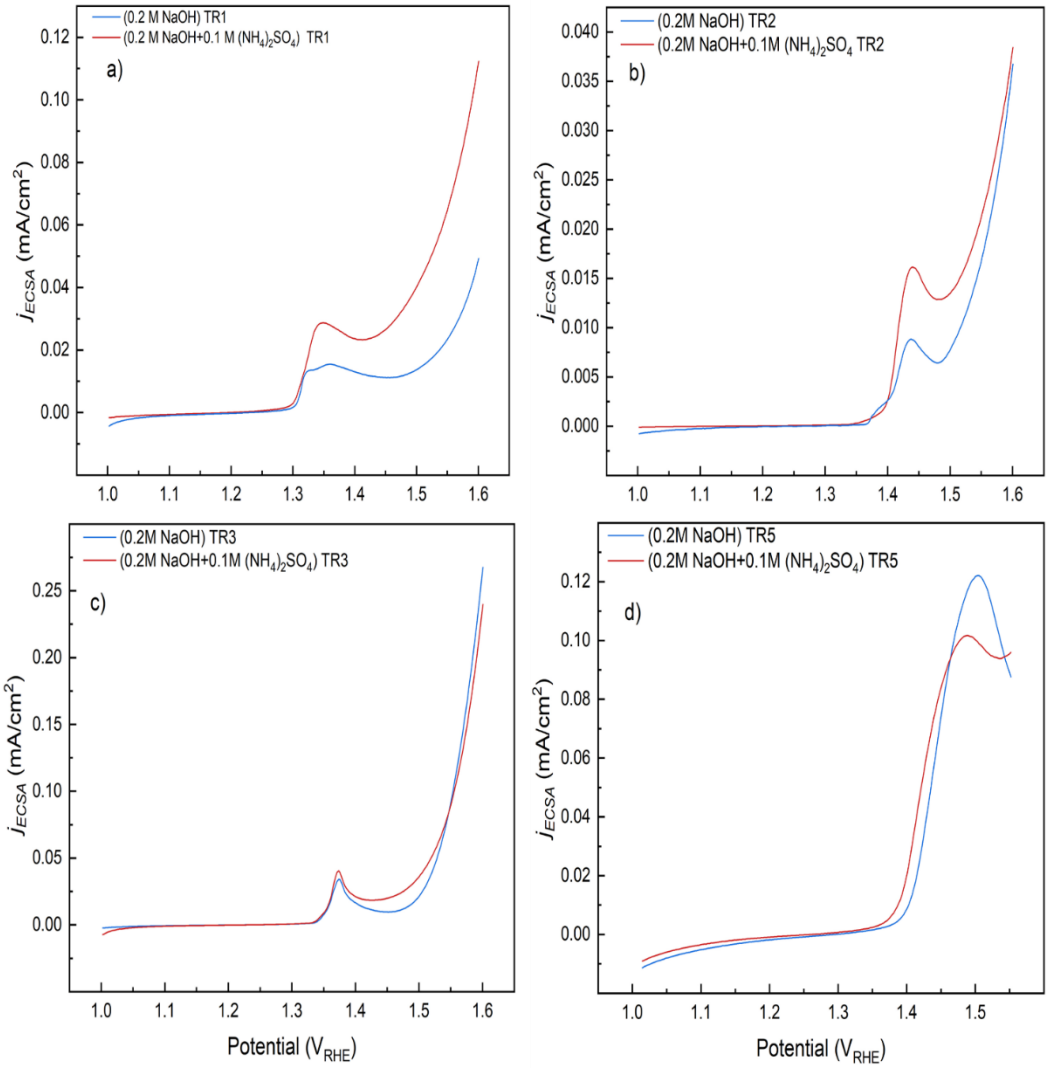

Figure 5.9: *The recorded LSV in the potential window 1.0-1.6 V vs RHE for the TR1 (a), TR2 (b), TR3 (c), and TR5 (d) samples are reported; the blu line refers to the LSV conducted in supporting electrolyte, namely NaOH while the red line showcases the electrochemical response when $(NH_4)_2SO_4$ is added.*

Looking at the TR3 sample, the Ni^{2+}/Ni^{3+} redox couple appears at 1.373 V vs RHE in both the supporting electrolyte and in the presence of the ammonia, and almost no difference in the current density arises. For the TR5 sample, the peak for the nickel redox couple is not apparent in the corresponding potential region, and the current response is similar in both media. Therefore, it is concluded that for these materials the catalytic activity towards ammonia oxidation is very low. The physicochemical characterization of these catalysts, with SEM images showing no recognizable morphology, could explain this behavior.

On the contrary, materials containing Cu (TR4 and TR6) develop improved activity towards eAOR. Figure 5.10 shows the electrochemical response of the TR4 sample and highlights the high current densities achieved with this material. The Ni^{2+}/Ni^{3+} redox couple onset potential in the electrolyte is set at 1.364 V vs RHE, with the oxidation peak centered at 1.377 V vs RHE. However, once the analyte $(NH_4)_2SO_4$ is introduced, ammonia oxidation starts at 1.392 V vs RHE reaching significantly high current values. Thus, it seems that the presence of copper is a determining factor since it is known to be the only other element active for this reaction[17]. Both EDS and ICP-MS analyses confirmed the presence of copper in the structure of this sample. Specifically, as previously mentioned, the cubic structure of this sample can be defined as a core-shell structure, where copper atoms are encapsulated within the framework, as evident from SEM images, and more precisely, from the TEM images of TR4, where a darker region can be observed inside the shell.

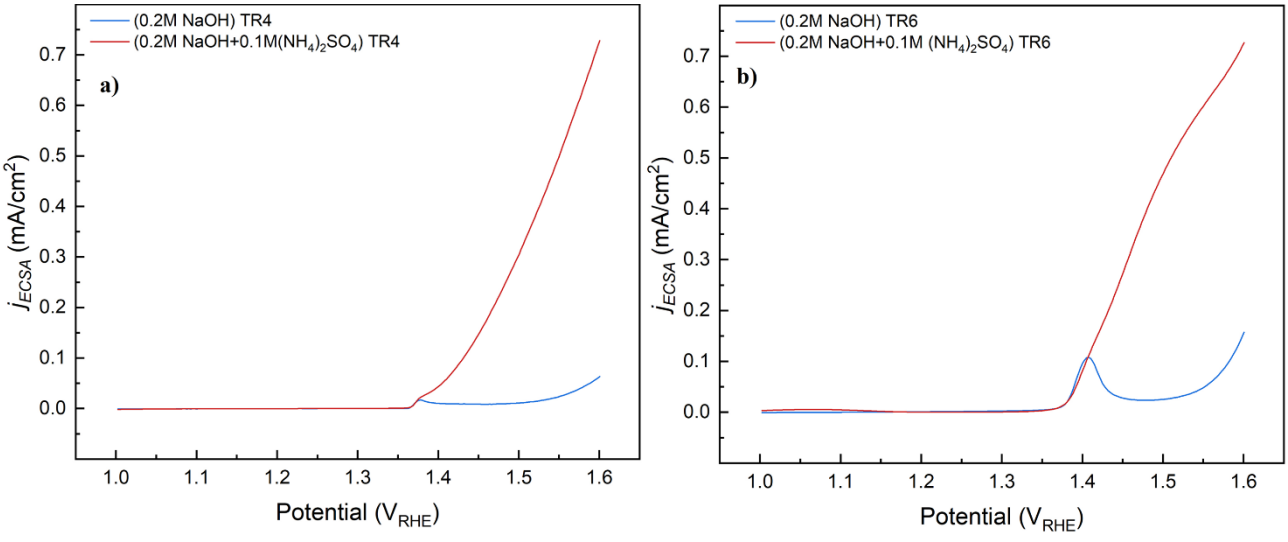

***Figure 5.10**: LSV recorded at 2 mV/s in the potential window 1.0-1.6 V vs RHE for TR4 (a), and TR6 (b). The blue line refers to the LSV conducted in NaOH while the red line shows the electrochemical response when $(NH_4)_2SO_4$ is added.*

To test the hypothesis of the relevance of Cu in these catalysts, another copper-containing sample was synthesized. The synthesis of the TR6 sample, previously discussed in the Experimental Section, resulted in a material with a morphology of cubes decorated with a thin monolayer of Ni atoms. The electrochemical response (Figure 5.10) displays the Ni^{2+}/Ni^{3+} transition peak at 1.406 V vs RHE with the eAOR starting at 1.415 V vs RHE, producing a significant current density increase.

Again, EDS and ICP-MS analyses were used to quantify the ratio of copper and nickel present for the bulk structure. As expected, since Cu_2O nanocubes were used as the template, the amount of copper is approximately three times that of nickel, and TEM images confirm this morphology. However, from these images, it is also difficult to distinguish the ideal monolayer of Ni on the surface of the copper template, so XPS analysis was used to establish the surface composition. This revealed very low amounts of superficial Ni on the Cu_2O cubes suggesting higher exposure for the copper active sites rather than nickel. From these results, it seems that the presence of $Ni(OH)_2$, and particularly the NiOOH species, is not enough to act as a good catalyst for the eAOR, leading to think that instead, the synergic effect of nickel and copper is the key to the successful electrooxidation of ammonia. It has been reported that Cu itself does not promote the adsorption of NH_3 (contrary to the Ni), and the synergic effect leads to the easier formation of $Ni_{1-x}Cu_xOOH(NH_3)$, a species achieving high activity towards eAOR[17,18].

Useful information can be accessed when comparing which species provides the catalytic sites at lower potential (NiOOH or Ni-Cu couple), as the presence of NiOOH should correspond to earlier and faster ammonia oxidation. Figure 5.11 (a) shows the LSV for both the TR4 (black line) and TR6 (green line) in argon-saturated 0.2 M NaOH cell around the onset potential for Ni^{2+}/Ni^{3+}. It is observed that TR4 displays lower onset potential than TR6, and the peak corresponding to the NiOOH formation is found at 1.377 V vs RHE, a value 29 mV lower than the 1.406 V vs RHE for TR6, therefore decreasing the onset potential for ammonia oxidation. Figure 5.11 (b) displays the NaOH and ammonia LSV for both samples in air (that is, in the presence of oxygen), showing that TR4 exhibits a lower onset potential for ammonia oxidation. The reason for this behavior can be explained from the exposition of catalytic sites at lower potentials than those of TR6, promoting the eAOR at more negative potentials. Also, it is observed that the presence of oxygen in the base electrolyte influences the eAOR.

Bearing in mind that that the cell environment could influence the electrochemical behavior of the catalysts, the electrochemical response in different conditions has been evaluated, namely under inert conditions saturating the cell with Ar gas, in air (without deoxygenation of the solution), and in an oxidating environment saturating the cell with O_2. TR4 sample was selected for further studies, as it

is the one with the best physicochemical characterization and electrochemical response. Figure 5.12 (a) presents the electrochemical response of the TR4 sample in an argon-saturated cell, a non-controlled environment cell (in air), and an oxygen-saturated cell, and how this affects reactivity. In the supporting electrolyte, the typical electrochemical response is observed without significant differences between the inert and O_2 environments for the peak position of the Ni^{2+}/Ni^{3+} transition, but with an increase in the OER current density.

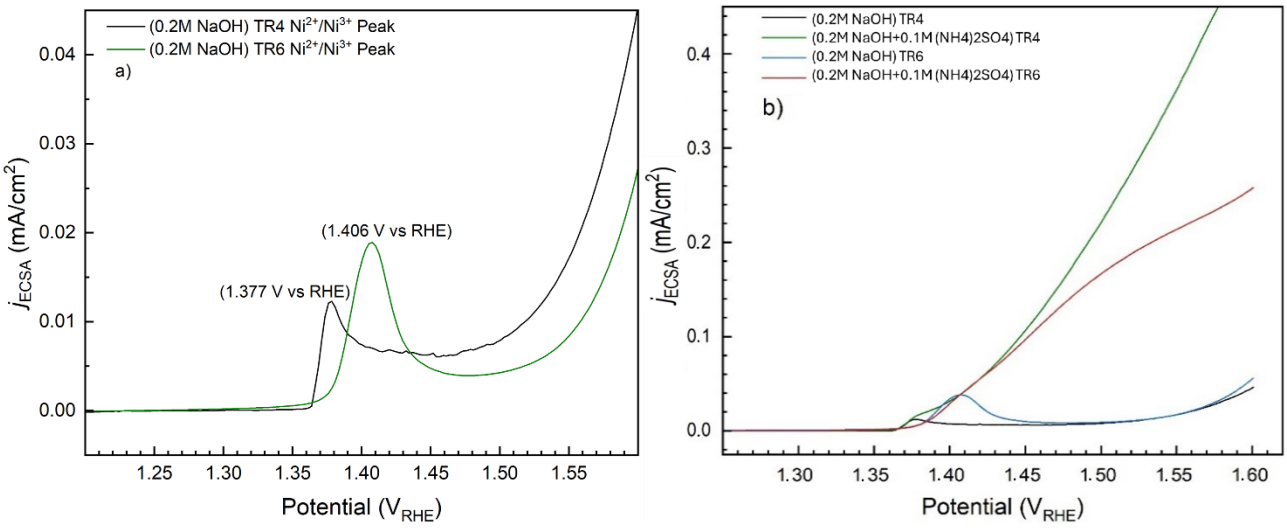

Figure 5.11: *(a) LSV at 2 mV/s in 0.2 M NaOH deoxygenated with Ar in the Ni^{2+}/Ni^{3+} couple potential region for TR4 and TR6. (b) LSV experiments for TR4 and TR6 in 0.2 M NaOH in the presence of air (not deoxygenated) and ammonia.*

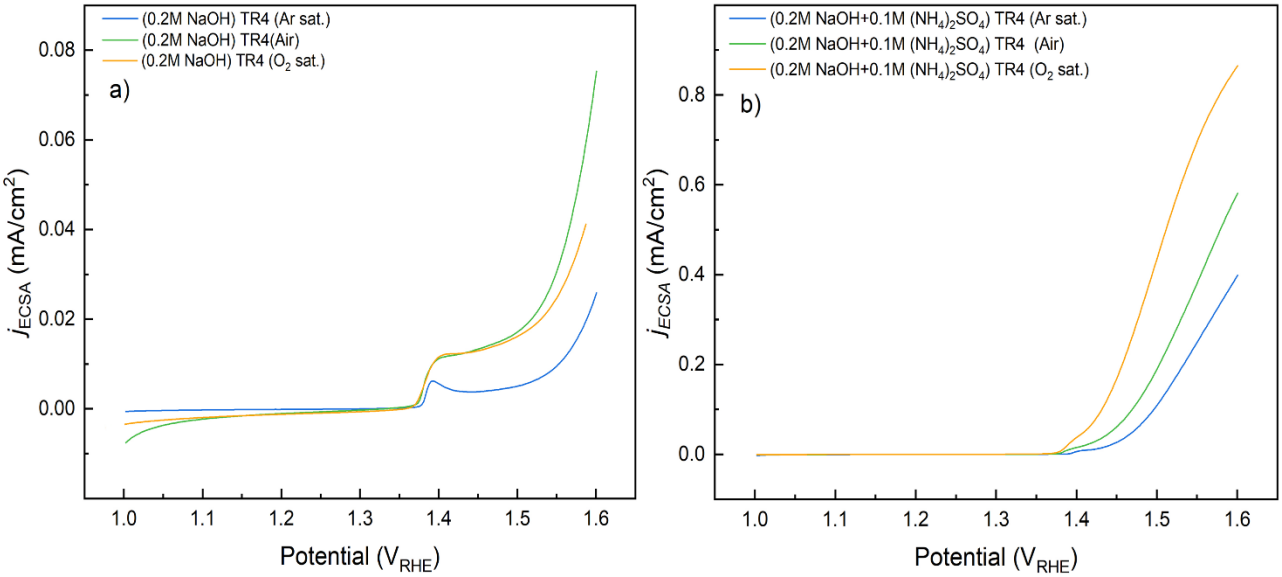

Figure 5.12: *LSV in NaOH 0,2 M in the potential window 1.0-1.6 V vs RHE for TR4 (a) in Argon saturated cell (blu line), environmental working conditions (yellow line), and oxygen saturated cell (green line). (b) LSV response for the TR4 in different environments when $(NH_4)_2SO_4$ is added.*

After adding ammonia to the cell (Figure 5.12 (b)) a clear influence of oxygen in this reaction is apparent, decreasing the onset potential and reaching higher currents, with respect to the air and inert conditions. The onset potentials for eAOR are found at 1.426 V vs RHE, 1.413 V vs RHE, and 1.409 V vs RHE, for the argon-saturated cell, the air cell, and the oxygen-saturated cell. In this sense, an O_2-mediated promotion effect could be suggested[19], where the excess of oxygen may result in the adsorption of more OH_{ads} on the catalyst surface, providing a major catalytic activity. Another alternative could be that oxygen itself plays a role in the oxidation of ammonia as an active oxidant, therefore allowing it to reach higher current densities.

At this point, for a better understanding of the processes taking place, it would be useful to establish the reactions involved and the products generated, which cannot be deducted only from LSV. Thus, differential electrochemistry mass spectrometry (DEMS) analysis has been performed for the TR4 sample.

5.9 Differential Electrochemical Mass Spectrometry (DEMS)

DEMS was used to obtain more information about the possible products generated during the electrochemical oxidation of ammonia on the catalyst TR4. By means of this technique, it is possible to accurately determine the onset potential of the electrochemical oxidation of ammonia and the other associated reactions, such as oxygen evolution reaction (OER), as well as nitrogen, NO and N_2O production. The experimental procedure, parameters and setup are described in the Experimental Section. Briefly, the selected m/z signals were set to follow OER (m/z = 32), N_2 (m/z = 28), NO (m/z = 30), and N_2O (m/z = 44). Since m/z = 44 can be attributed both to N_2O and CO_2, to be sure that this signal was indeed coming from N_2O and not from carbon dioxide, the m/z = 22 was also monitored, corresponding to ion fragmentation of the CO_2^{++}. The results obtained for this characterization are depicted in Figure 5.13. Only positive-going potential scans are shown for the ionic mass signals in this figure.

Figure 5.13 (a) shows the CVs performed at 0.5 mV/s in argon and oxygen-saturated supporting electrolyte and in presence of ammonia. When only the supporting electrolyte is present, the Ni^{2+}/Ni^{3+} transition appears at 1.39 V vs RHE in the argon saturated solution and in the oxygen saturated one, following the reaction:

$$Ni(OH)_2 + OH^- \rightarrow NiOOH + H_2O + e^- \quad (5.2)$$

The detection of O_2 and the determination of the onset for OER is important to confirm the reactivity of these materials toward this reaction, and to select a proper potential window to study the eAOR,

since this reaction could be influenced by oxygen evolution. Figure 5.13 (b) displays the ionic current for O_2, developing an onset potential of 1.50 V vs RHE in the argon-saturated electrolyte, and 1.46 V vs RHE in the oxygen-saturated electrolyte. After adding ammonia to the cell, a shift towards more positive potential is observable, as the OER starts at 1.60 V vs RHE in the argon-saturated cell, whereas the onset potential for this reaction in the oxygen-saturated cell is 1.62 V vs RHE. These results align with the trend observed in the CVs (Figure 5.13 (a)), if it is considered that oxygen evolution follows reaction 5.3:

$$NiOOH \rightarrow Ni + O_2 + H^+ + e^- \tag{5.3}$$

When ammonia is added and considering its adsorption on the catalyst, the OER is inhibited and a shift in the onset potential towards more positive potential values is seen. The reaction 5.4 describes the adsorption of ammonia on the catalyst surface:

$$NiOOH + NH_3 \rightarrow NiOOH\left(NH_{3_{ads}}\right) \tag{5.4}$$

The MSCVs for N_2 can be observed in Figure 5.13 (c). As expected, in the absence of ammonia, no nitrogen was detected. Once ammonia is present in the cell, an increase in the signal m/z = 28 is apparent, displaying onset potential values of 1.50 V and 1.43 V vs RHE for the argon and the oxygen-saturated solutions, respectively. The reaction responsible for the evolution of N_2 can be written as:

$$NiOOH + NH_3 \rightarrow NiOOH\left(NH_{3_{ads}}\right) \rightarrow NiOOH + \frac{1}{2}N_2 + 3H^+ + 3e^- \tag{5.5}$$

These onset values are similar to the OER onset potential when this reaction occurs in the absence of ammonia, suggesting that OER in the presence of ammonia was inhibited by adsorbed NH_3 species. Once these species are oxidized to nitrogen, free active sites are exposed to promote the OER. This is the reason why the onset potential for OER in presence of ammonia requires much more positive potential (1.60 V vs RHE). Comparing the LSVs shown in the 'Conventional Electrochemical Characterization' Section (Section 5.8), some differences are apparent. Firstly, different scan rates have been applied. For DEMS, a scan rate of 0.5 mV/s was used, while for common LSV it was set to 2 mV/s. Also, the ammonia concentration varied, being 0.2 M for DEMS, and 0.1 M for common LSV. Both conditions favor ammonia adsorption, justifying the shift toward more positive potential when looking at DEMS results. A higher analyte concentration is considered in DEMS configuration as vacuum pumps can decrease ammonia concentration in the solution over time[19].

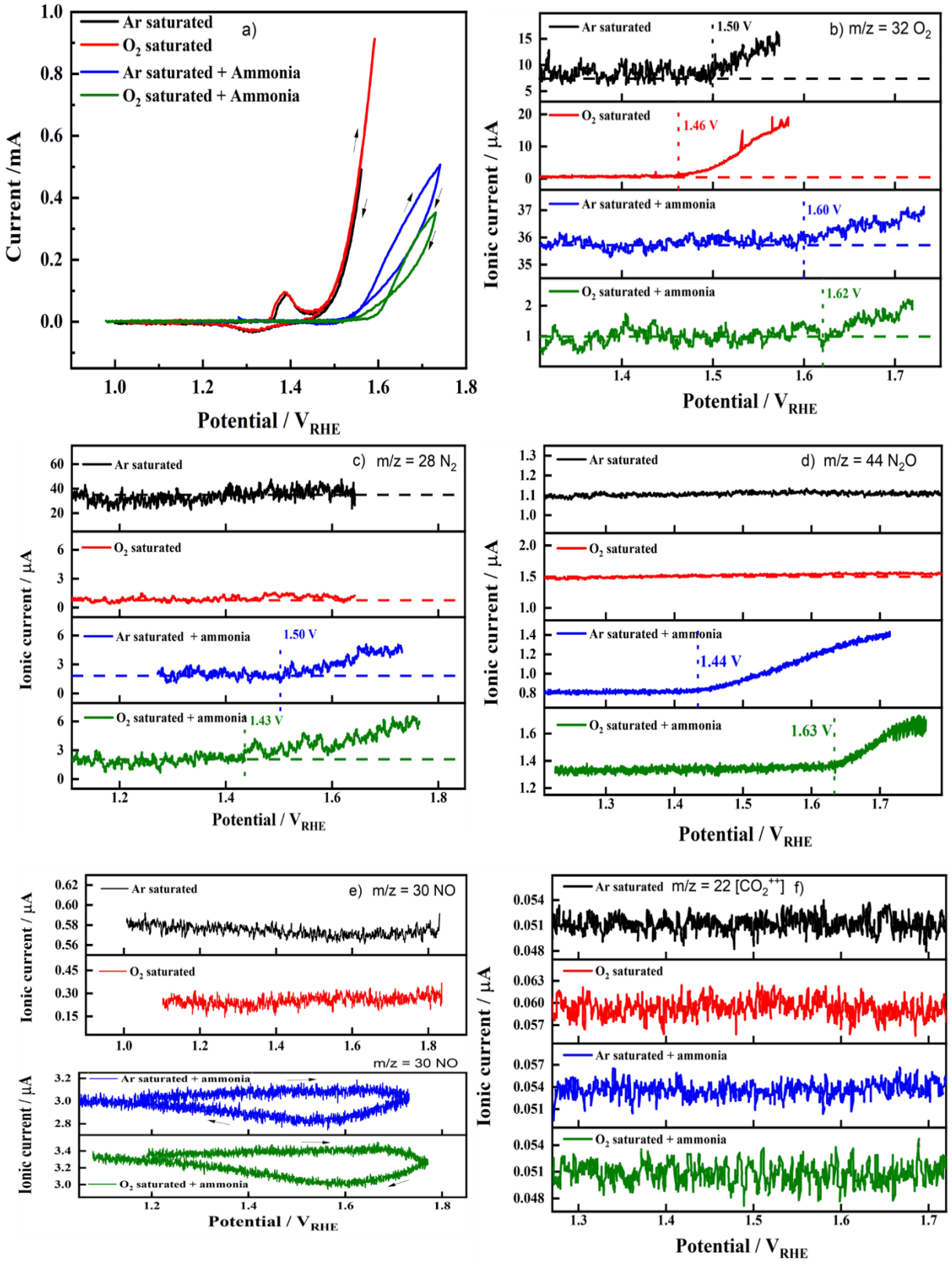

Figure 5.13: *(a) CVs showing the recorded faradaic current in different environment for the TR4 sample, (b) MSCVs for $_{O2}$ (m/z = 32), (c) for N_2 (m/z = 28), (d) for NO_2 (m/z = 44), (e) for NO (m/z = 30), and f) for CO_2 (m/z = 22).*

In Figure 5.13 (d), the ionic current to produce N_2O is shown. It can be seen how N_2O is formed in the argon-saturated cell in parallel with N_2 production, with an onset potential located at 1.44 V vs RHE. In the case of the oxygen-saturated ammonia solution, the N_2O generation goes in parallel with the OER at more positive potential, with an onset potential of 1.63 V vs RHE. Comparing this result with those observed in the CVs (see Figure 5.13 (a)), it can be stated that the registered faradaic currents at E < 1.60 V vs RHE in the absence of O_2 in the ammonia-containing solution are mainly related to the generation of N_2O. Equation 5.6 describes the reaction associated to the formation of N_2O:

$$NH_3 + 4OH^- \rightarrow \frac{1}{2}N_2O + \frac{7}{2}H_2O + 4e^- \quad (5.6)$$

An interesting result was observed when looking at the NO ionic current, depicted in Figure 5.13 (e). The shape of the MSCV for this mass signal is typical for the consumption of a species present in the bulk of the solution. Thus, when a cyclic voltammetry experiment is performed between 1.0 and 1.75 V vs RHE, the NO mass signal decreases at 1.67 V and 1.69 V vs RHE for the Ar-saturated and O_2-saturated electrolyte, respectively. This is an interesting result, as other literature works on DEMS eAOR study at NiOOH electrodes did not detect the formation of NO, although it was not completely ruled out since it can react in an alkaline solution to generate NO_2^-[19].

An explanation for the behavior of the m/z = 30 signal is that NO is formed when ammonia is added to the cell at low potential (i.e. 0.60 V vs RHE), following Equation 5.7:

$$NH_3 + 5OH^- \rightarrow NO + 4H_2O + 5e^- \quad (5.7)$$

This fact brings, consequently, the constant presence of this compound in the electrochemical cell. NO was not detected at NiOOH[19], the behavior in the present paper can be attributed to the presence of Cu atoms. A deep discussion in this regard will be addressed later in the analysis of the results depicted in Figure 5.14.

Finally, Figure 5.13 (f) shows the response for m/z = 22, which corresponds to the ion fragmentation of the CO_2^{++}. This signal did not show any variation, regardless of the different employed experimental conditions, leading to the conclusion that no carbon dioxide was formed as a product from the possible oxidation of the carbon cloth employed as support for the catalysts. Therefore, the previously detected m/z = 44 signal was due to N_2O presence.

In order to get more insights about the behavior of m/z = 30 corresponding to NO and its relationship with the ammonia, a current vs time curve was obtained at 0.60 V vs RHE introducing the ammonia solution at the specific time of 300 s and recording the response of this mass signal. The results

obtained for this experiment are depicted in Figure 5.14 (a). The addition of ammonia induces an increase in the ionic current associated to the m/z = 30, meaning the formation of NO. This experiment justifies the presence of NO in the solution and accounts for the decrease in its signal during the MSCVs described in Figure 5.13 (e), and thus promoting the formation of N_2O, according with the reaction 5.8:

$$2NO + 2OH^- \rightarrow N_2O + O_2 + H_2O + 2e^- \quad (5.8)$$

The formation of N_2O from NO is evident in the comparison of the MSCVs for the production of N_2O and the consumption of NO displayed in Figures 5.14 (b) and (c), in both argon and oxygen-saturated cells, respectively. At E > 1.60 V vs RHE, the consumption of NO is observable, as the N_2O signal increases in intensity along with the oxygen, probably due an NO-mediated oxygen production, following the Equation 5.8.

At high positive potentials, oxidation to nitrite and nitrate is also plausible (see reactions 5.9 and 5.10), however, these species cannot be monitored with DEMS, and other specific characterization techniques must be applied.

$$NO + \frac{1}{4}O_2 + OH^- \rightarrow NO_2^- + \frac{1}{2}H_2O \quad (5.9)$$

$$NO + O_2 + OH^- \rightarrow {NO_3}^- + H_2O \quad (5.10)$$

Right away, the influence of the oxygen in the cell can be seen, facilitating the reaction to form the NiOOH (Equation 5.2), and inhibiting the reaction given in Equation 5.6, as a shift of 200 mV toward more positive potentials is observable in the presence of O_2. A plausible adsorption-evolution mechanism for the OER is shown in Figure 5.15 (a). Alternatively, the lattice oxygen evolution mechanism (LOEM) can be evaluated (b), where the presence of oxygen in the lattice favours the reaction 5.11[23]:

$$NiO \rightarrow Ni^{2+} + O_2 + 4e^- \quad (5.11)$$

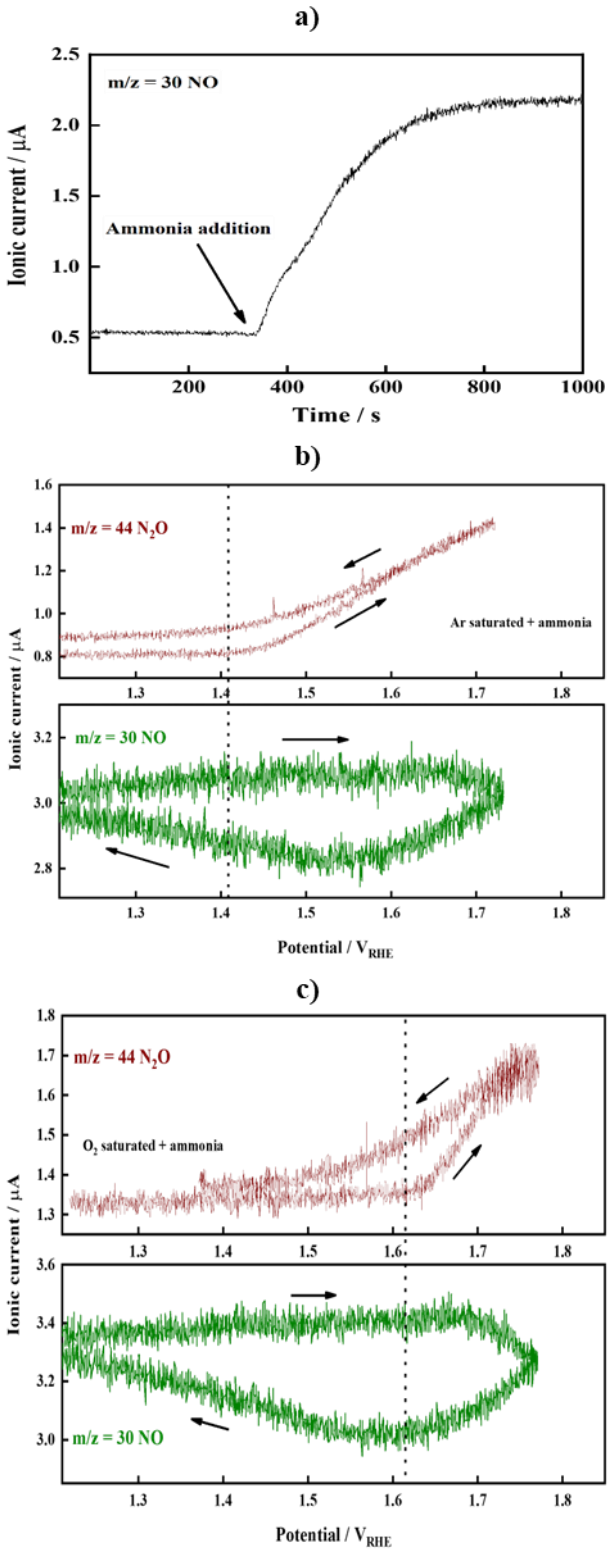

***Figure 5.14**: (a) Chronoamperometry monitoring the NO production at 0.60 V vs RHE after adding ammonia to the base electrolyte solution.(b) MSCVs at 0.2 mV/showing the ionic current registered for NO and N_2O in oxygen saturated and (c) in argon saturated electrolyte solutions. TR4 sample.*

Regarding the eAOR, Chan et al. propose the reaction mechanism found in Figure 5.15 (c), where it is explained that the occupation of the Ni sites by $*NH_x$ species hinder oxygen production, leading to the OER deactivation in argon saturated electrolytes[19]:

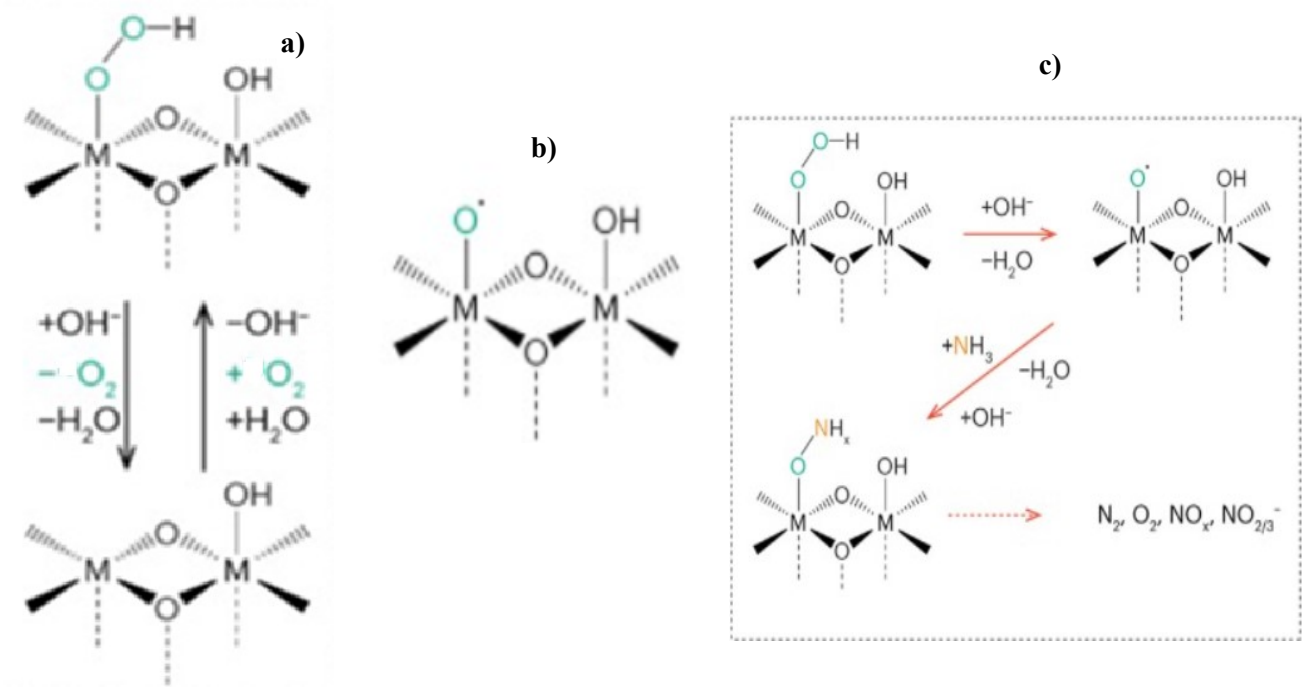

***Figure 5.15**: (a) Proposed mechanism for the OER on the electrode's surface. Another possibility is displayed in (b), showing the lattice oxygen evolution mechanism (LOEM). In (c) the proposed mechanism for the eAOR is shown. Reprinted from (19).*

According to our results, the first step, that is the formation of the M-O° radical, is favoured in the presence of molecular oxygen in solution (in the absence of ammonia). Higher faradaic currents were recorded for the OER, possibly due to the presence of Cu in the material, different than the case reported in the literature[19,23].

Regarding the final reactions, the ones concerning nitrogen-containing products, assuming the formation of the adsorbed intermediate, differences arise for N_2O formation in the presence of O_2 (around 200 mV positive shift in the presence of O_2) but not for N_2 production. The presence of O_2 in ammonia solution seems to have no influence on the processes related with adsorbed species (i.e. the production of N_2, Equation 5.5); however, on a bulk process (Equation 5.6) the radical (Figure 5.17 (b)) is stabilized in the presence of O_2 and it is possibly the active size involved in N_2O. Oxygen adsorbs after desorption of $NH_{3_{ads}}$ and blocks this active site. In argon, the species is not stabilized

and as soon as N_2 is formed, and free active sites are exposed, ammonia is directly oxidized to N_2O at that potential.

Finally, the rate determining step (*rds*) for the OER can be determined from the MSCV for m/z = 32 in the different reaction conditions. Faradaic currents and mass currents are proportional for a specific reaction. Therefore, Tafel analysis can be performed directly with DEMS data. Equations (2.7-2.11) describe the mechanism for the OER in alkaline media and the values for the different Tafel slopes when each step acts as *rds*. Figure 5.16 (a) displays the signals for m/z = 32 when OER takes place (Figure 13 (b)), whereas Figure 5.16 (b) shows the Tafel analysis for this reaction, reporting a Tafel slope of 120 mV dec^{-1} when working in an argon saturated environment, both in supporting electrolyte and in presence of ammonia, respectively.

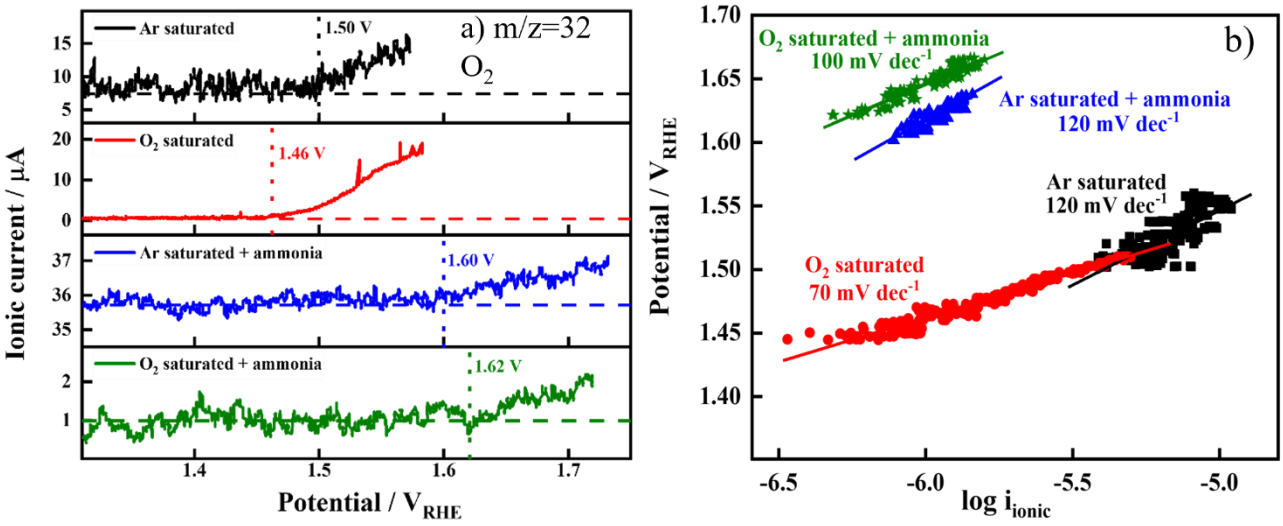

Figure 5.16: *MSCVs for m/z=32 ionic currents in different environments (a), and (b) Tafel plots obtained for the OER from (a) for the TR4 sample.*

This result permits to attribute the *rds* to the first step of the mechanism (Equation 5.12). When oxygen is present in the cell, the calculated Tafel slopes are 70 mV dec^{-1} and 100 mV dec^{-1} in supporting electrolyte and in presence of ammonia, respectively. A mixed kinetic control is found for OER in these conditions, involving steps 1 and 2 (Equation 5.12 and 5.13). Then, it can be concluded that the presence of O_2 in the solution modifies the OER mechanism.

Summarizing, important conclusions on the mechanism for eAOR at TR4 can be made from these DEMS results, indicating that eAOR is a potential dependent reaction influenced by the presence of oxygen. This reaction occurs in competition with the OER in the same potential region. In fact, the presence of ammonia hinders the OER and shifts its onset potential to more positive values. DEMS confirms the production of N_2 and N_2O from eAOR and the presence of NO as intermediate species

involved in formation of N_2O, promoted by Cu atoms in the catalysts. The eAOR is affected by the presence of O_2 promoting eAOR-to-N_2 at low potentials and eAOR-to-N_2O at high potentials. Moreover, the OER mechanism is altered by the presence of O_2 for both the base electrolyte and the ammonia containing solution.

Bibliography

1. Zhao, W., Zhang, C., Geng, F., Zhuo, S. & Zhang, B. Nanoporous hollow transition metal chalcogenide nanosheets synthesized via the anion-exchange reaction of metal hydroxides with chalcogenide ions. *ACS Nano* **8,** 10909–10919 (2014).
2. Wang, Y., Zhu, Q. & Zhang, H. Fabrication of β-$Ni(OH)_2$ and NiO hollow spheres by a facile template-free process. *Chem. Commun.* **41,** 5231–5233 (2005).
3. Tian, L., Yang, T., Pu, W. *et al.* Synthesis of cubic $Ni(OH)_2$ nanocages through coordinating etching and precipitating route for high-performance supercapacitors. *Nanoscale Res. Lett.* 14**,** 264 (2019).
4. Xu, F., Hu, K., Wang, S. *et al.* ZIF-8 derived $Ni(OH)_2$ hollow nanocages for non-enzymatic glucose electrochemical sensing. *J. Mater. Sci.* **57,** 18589–18600 (2022).
5. Lu, P., Liu, Q., Xiong, Y., Wang, Q., Lei, Y., Lu, S., Lu, L. & Yao, L. Nanosheets-assembled hierarchical microstructured $Ni(OH)_2$ hollow spheres for highly sensitive enzyme-free glucose sensors. *Electrochim. Acta* **168,** 148–156 (2015).
6. Simon, P., Baldovino-Medrano, V.G. & Wojcieszak, R. X-ray photoelectron spectroscopy (XPS): Principles and application for the analysis of photoactive materials. In *Springer Handbook of Inorganic Photochemistry*, Bahnemann, D. & Patrocinio, A.O.T., Eds., Springer Handbooks, Springer, Cham (2022).
7. Krishna, D.N.G. & Philip, J. Review on surface-characterization applications of X-ray photoelectron spectroscopy (XPS): Recent developments and challenges. *Appl. Surf. Sci. Adv.* **12** (2022).
8. Biesinger, M.C., Payne, B.P., Lau, L.W.M., Gerson, A. & Smart, R.S.C. X-ray photoelectron spectroscopic chemical state quantification of mixed nickel metal oxide and hydroxide systems. *Surf. Interface Anal.* **41,** 324–332 (2010).
9. Biesinger, M.C., Lau, L.W.M., Gerson, A.R. & Smart, R.S.C. Resolving surface chemical states in XPS analysis of first-row transition metals, oxides, and hydroxides: Sc, Ti, V, Cu, and Zn. *Appl. Surf. Sci.* **257,** 887–898 (2010).
10. Hall, D.S., Lockwood, D.J., Bock, C. & MacDougall, B.R. Nickel hydroxides and related materials: A review of their structures, synthesis, and properties. *Proc. R. Soc. A* **471,** 20140792 (2015).
11. Tang, T. *et al.* Electronic and morphological dual modulation of cobalt carbonate hydroxides by Mn doping toward highly efficient and stable bifunctional electrocatalysts for overall water splitting. *J. Am. Chem. Soc.* **139,** 8320–8328 (2017).

12. Morales, D.M. & Risch, M. Seven steps to reliable cyclic voltammetry measurements for the determination of double layer capacitance. *J. Phys. Energy* **3,** 034013 (2021).
13. Machado, S.A.S. & Avaca, L.A. The hydrogen evolution reaction on nickel surfaces stabilized by H-absorption. *Electrochim. Acta* **39,** 1385–1391 (1994).
14. Cossar, E. *et al.* Comparison of electrochemical active surface area methods for various nickel nanostructures. *J. Electroanal. Chem.* **870,** 114246 (2020).
15. Martínez-Hincapié, R., Wegner, J., Anwar, M. U., Raza-Khan, A., Franzka, S., Kleszczynski, S., Čolić, V. The determination of the electrochemically active surface area and its effects on the electrocatalytic properties of structured nickel electrodes produced by additive manufacturing. *Electrochim. Acta* **476,** 143663 (2024).
16. Srinivasan, V. & Weidner, J. W. Studies on the capacitance of nickel oxide films: Effect of heating temperature and electrolyte concentration. *J. Electrochem. Soc.* **147,** 880 (2000).
17. Xu, W., Lan, R., Du, D., Humphreys, J., Walker, M., Wu, Z., Wang, H. & Tao, S. Directly growing hierarchical nickel-copper hydroxide nanowires on carbon fibre cloth for efficient electrooxidation of ammonia. *Appl. Catal. B Environ.* **218,** 470–479 (2017).
18. de Vooys, A.C.A., Koper, M.T.M., van Santen, R.A. & van Veen, J.A.R. The role of adsorbates in the electrochemical oxidation of ammonia on noble and transition metal electrodes. *J. Electroanal. Chem.* **506,** 127–137 (2001).
19. Chen, J., Chen, S., Gao, J., Huang, X., Stavrou, E., Vogt, C. & Zheng, W. Correlative *in situ* analysis of the role of oxygen on ammonia electrooxidation selectivity on NiOOH surfaces. *J. Catal.* **438**, 115720 (2024).
20. Rosca, V. & Koper, M. T. M. Electrocatalytic oxidation of ammonia on Pt(111) and Pt(100) surfaces. *Phys. Chem. Chem. Phys.* **8,** 2513–2524 (2006).
21. Li, Z.-F., Wang, Y. & Botte, G. G. Revisiting the electrochemical oxidation of ammonia on carbon-supported metal nanoparticle catalysts. *Electrochim. Acta* **228,** 351–360 (2017).
22. Garcia, A.C. & Koper, M.T.M. Effect of saturating the electrolyte with oxygen on the activity for the oxygen evolution reaction. *ACS Catal.* **8**, 9359–9363 (2018).
23. Exner, K.S. On the lattice oxygen evolution mechanism: avoiding pitfalls. *ChemCatChem* **13**, 4066 (2021).

CHAPTER 6

6.1 Conclusions

Nickel-based electrocatalysts were synthesized to study their activity toward the electrochemical Ammonia Oxidation Reaction (eAOR).

Multiple nickel hydroxide materials were prepared (samples TR1, TR2, TR3, TR4, TR5 and TR6) by the solvothermal method, where some modifications were introduced to obtain different morphologies. The first three samples were synthesized starting from different precursors and/or solvents, whereas samples four and six were synthesized starting from a copper template to obtain a hollow cage structure with different Ni:Cu ratio. Sample 5 was synthesized with the help of a ZIF-8 (Zeolitic Imidazolate Framework) precursor to obtain cubic morphology.

The morphologies were investigated by electron microscopies, which showed the several issues encountered during the synthesis of sample 1, 3, and 5. They presented no defined morphology, only displaying big agglomerates. On the other hand, sample 2 was formed by spheres of 1-3 μm diameter constituted of several two-dimensional nanosheets. Samples 4 and 6 had a hollow cages structure, but differences were observed between them. In the case of sample 4, the cage was made of Ni hydroxide hosting Cu atoms inside the structure. On the contrary, in sample 6, the cage was of a copper structure with a layer of Ni hydroxide on the surface. In fact, both samples contained a different Ni:Cu ratio, being 10:1 and 1:9 for samples 4 and 6, respectively.

XRD revealed the presence of β-$Ni(OH)_2$ phase in the first three samples, while samples 4 and 5 showed an amorphous structure and a closer resemblance to the α-$Ni(OH)_2$ phase. Sample 6, however, contained a limited amount of Ni, showing an XRD spectrum with little resemblance to the Ni reference.

XPS analysis was used to study the surface composition and stoichiometry of the Ni-containing samples, confirming the hydroxide structure for all of them. Both samples containing copper had both Cu(I) and Cu(II) on the surface. However, CuO was the main component for sample 4, while Cu_2O was the major one in sample 6. The stoichiometry analysis confirmed that Ni hydroxide was deposited on the surface of the copper cages for sample 6, as shown in TEM images and as expected from the synthetic procedure adopted.

All the materials were tested as eAOR electrocatalysts. Samples containing only Ni (TR1, TR2, TR3; TR5) resulted in not be electrocatalytically active, whereas the copper-containing samples (TR4, and

TR6) proved to be active catalysts for the ammonia oxidation reaction. Considering that copper oxide was not very active for the eAOR, a synergetic effect between Ni and Cu is elucidated. It was found that the oxidation of Ni(II) to Ni(III), which is the active species for the eAOR, occurred at lower potentials in sample 4 (1.39 V vs RHE) than in sample 6 (1.42 V vs RHE).

Since sample 4 was the most promising catalyst, further electrochemical characterization was employed to determine the best catalytic conditions. The presence of oxygen lowered the potential at which Ni(III) is formed and, therefore, decreased the eAOR overpotential of about 30 mV. Alternatively, oxygen itself could play a role as an adsorbed species providing OH^- sites.

DEMS was used to bypass conventional electrochemistry limitations, and accurately detect the products of the reaction, monitoring m/z signals corresponding to N_2 (m/z=28) O_2 (m/z=32), NO (m/z=30), and N_2O (m/z=44). Since m/z = 44 can be attributed both to N_2O and CO_2, the m/z = 22 was also monitored, corresponding to ion fragmentation of the CO_2^{++} species. This was ultimately done to be sure that this signal was indeed coming from dinitrous oxide and not from carbon dioxide.

As expected, no nitrogen-based compounds were detected in the absence of ammonia, with only the oxygen evolution present as ionic current. Adding ammonia to the cell, nitrogen production was successfully determined at an onset potential of 1.50 V vs RHE and 1.43 V vs RHE for the argon and oxygen saturate cell, respectively. On the other hand, oxygen evolution was confirmed at 1.60 V vs RHE and 1.62 V vs RHE, respectively. At these high potentials, N_2O formation was also confirmed. The m/z = 22 signal did not show potential dependence, confirming no contribution from the oxidation of the carbon cloth.

An interesting result was found monitoring the NO evolution, which underwent consumption probably due to further oxidation, possibly to form N_2O. The formation of NO was not previously reported when working with Ni electrodes, which lead to believe that the presence of Cu was a key aspect in the selectivity of the eAOR.

An accurate Tafel analysis for the OER was possible from m/z = 32 DEMS signal. Calculated Tafel slope values agree with literature work, and a proposed mechanism was discussed for the sample 4. Unfortunately, due to the selectivity issues of eAOR and the potentially high number of exchanged electrons to form a multitude of byproducts, it is rather difficult to perform a Tafel analysis and propose a precise determination of a rate-determining step for ammonia oxidation.

Summarizing, DEMS allowed the precise determination of the products of the reactions and their onset potential. Nitrogen production was confirmed, while a potential dependency of the eAOR and

an influence of the presence of the oxygen in the solution were observed. The latter apparently promoted ammonia oxidation to N_2 at low potentials and to N_2O at high potentials.

Acknowledgements

I would like to thank the Erasmus+ Traineeship Program and the University of Padova for financial support and the opportunity to spend this research period abroad. Also, I would like to thank the University of La Laguna for hosting me and Professor Elena Pastor for accepting me at her Grupo de Ciencia de Superficies y Electrocatálisis laboratories at the University of La Laguna and for guiding me during this internship period. I would also like to extend my gratitude to Juan Carlos and Abraham for their patience, support, and their mentorship throughout these 6 months. I am very thankful to all of them and to the other members of the team, Carmen, Yapci, Stefan, Gonzalo, Sthephanie, Jennifer, Noemi, Ana, and Ruth for all the shared moments, for all the lessons they taught and for helping me along the way, overcoming the frustration when things got hard and for being patient for all the mistakes. A special thanks goes to Sacha for sharing this journey and being such a fun and crazy companion.

I would like to warmly thank Professor Laura Calvillo for her mentorship, availability, advice, and patience throughout this journey, as well as Professor Christian Durante for his support and the thoughtful insights he provided during this research period.

A special thanks goes to Marisa and Luis for welcoming me so warmly into their home and making me feel like part of a family from the very beginning. Thank you for helping me discover your island and culture, for all the laughter and shared dinners, and for supporting me even on the darkest days, bringing a smile to my face even when I thought it was impossible. I would also like to express my gratitude to Nico for being like a big brother, a guide and a reference during this time, for all the adventures and the amazing places you showed me around the island, for your incredible stories, and for always being cheerful and radiant. And for introducing me to Ugo. You all have taught me the value of sharing, of hospitality, and the importance of not taking life too seriously and smiling through it, because everything will eventually turn out fine.

Ringrazio inoltre tutti i compagni conosciuti in questo percorso quinquennale per le mille battaglie combattute assieme tra le mura del Disc e per le mille risate sui muretti all'ora di pranzo. Che Faust il custode sia con voi.

Ci tengo a ringraziare tutti i miei amici più stretti per essermi stati a fianco da ben prima dell'inizio di questa avventura, e per essere ancora parte della mia vita. Non sono stati anni facili ed il supporto di ognuno di voi mi ha dato il coraggio per non arrendersi mai.

Un grazie anche a Monica, Costantino e David per essere parte della mia famiglia ed essermi stati vicini nei momenti più difficili, spronandomi a non mollare e a dare il massimo, senza dimenticare di prendermi cura di me stesso. Mi avete sempre offerto amore e sostegno, un rifugio sicuro e tante risate.

Voglio dedicare un grazie speciale a mio padre Alessandro per avermi permesso di intraprendere questo viaggio e per essere un punto di riferimento. Il tuo cuore grandissimo, il tuo amore, la tua gentilezza, e la tua infinita disponibilità nell'aiutare chiunque sono un modello a cui aspirare e un esempio per affrontare tutte le difficoltà che la vita ci ha posto davanti. A mia sorella Chiara e a mio fratello Francesco per aver creduto in me, per essere stati sempre presenti e per avermi aiutato a crescere. Siete stati grandi maestri e saggi consiglieri, sempre presenti al momento opportuno. Infine, un grazie anche a mia madre che nonostante tutto rimane sempre presente nei nostri cuori.

Alle zie, agli zii, ai miei cugini, ad Antonietta, Laura, Carlotta, Angelo, e Giulia dico grazie per i preziosi ricordi, per essere qui con me per festeggiare questa meta e a brindare ad un nuovo inizio.

E per concludere vorrei ringraziare Elisa. Crescere assieme in tutti questi anni, imparando a conoscerci, accettarci, supportarci e amarci è stata un'avventura fantastica. Grazie per avermi insegnato ad amare e avermi sempre permesso di essere me stesso. Hai trasformato la mia vita e ogni giorno mi dai il coraggio per essere la versione migliore di me stesso, quella che tu hai sempre visto, anche quando io nemmeno sapevo della sua esistenza. Non avrei potuto desiderare una compagna di avventure migliore e non vedo l'ora di scoprire cosa ci riserva il futuro e come sapremo cambiare e crescere, insieme.